A GPS-based method for pressure corrections to neutron monitor data

IZAK G. MORKEL

A GPS-based method for pressure corrections to neutron monitor data

Izak G. Morkel, B.Sc.

Dissertation accepted for the degree Master of Science in Physics
at the North-West University

Supervisor: Prof. H. Moraal
Co-supervisor: Dr A.Z.A. Combrink

July 2008

Potchefstroom Campus

Abstract

Galactic cosmic rays are high-energy particles in the heliosphere. When entering the atmosphere of earth, they interact with the nuclei of air molecules, which then cascade down to the earth's surface. The nuclear active secondary particles of the cascade consist of protons and neutrons, and the amounts of these different species are dependent on the thickness of the atmosphere. Neutron monitors detect these nuclear active secondaries, and to normalise these counting rates from day to day requires accurate pressure measurements e.g. *Krüger* (2006).

With a normal barometer, accurate pressure measurements can be obtained, but it has been found that when a strong wind blows, the pressure drops. According to *Malan and Moraal* (2002) this drop in pressure can be explained by the Bernoulli effect. The idea therefore is to make use of the latest technology, in this case the Global Positioning System (GPS), to correct for this environmental effect. GPS technology makes it possible to determine the column density of air above a certain area with high precision, but it is greatly affected by precipitable water vapour in the atmosphere e.g. *Combrink* (2003). The idea then is to determine a method for using the strong points of both sets of data, to find a possible data set in which both weather conditions (wind and humidity) are corrected for. If this is possible it will greatly increase the accuracy of neutron monitor data around the world.

Keywords: neutron monitor, dispersion,
GNSS, pressure corrections
GPS, cosmic rays

Opsomming

'n GPS gebaseerde metode vir druk korreksies aan neutron monitor data

Galaktiese kosmiese strale is hoë energiedeeltjies in die heliosfeer. Wanneer dit die atmosfeer van die aarde binne kom, bots dit teen die kerne van lugmolekules, en veroorsaak 'n kaskade van sekondêre deeltjies. Die kernaktiewe sekondêre deeltjies van die kaskade bestaan uit protone en neutrone: die hoeveelheid van die deeltjies is afhanklik van die dikte van die atmosfeer. Neutron monitors neem hierdie kernaktiewe sekondêre deeltjies waar. Om die teltempo van dag tot dag te normaliseer vereis akkurate drukmetings bv. *Krüger* (2006).

Met 'n barometer kan akkurate drukmetings geneem word, maar daar is bevind dat as daar 'n sterk wind waai, dan val die druk. Volgens *Malan and Moraal* (2002) kan die val in die druk verduidelik word deur die Bernoulli effek. Daarom is die doel van hierdie verhandeling om van die nuutste tegnologie, in die geval die Globale Posisionering Sisteem (GPS), gebruik te maak om te korrigeer vir hierdie omgewingseffek. GPS tegnologie maak dit moontlik om die kolomdigtheid van lug bo 'n sekere area met hoë akkuraatheid te bepaal. Die GPS tegnologie word egter grootliks geaffekteer deur die hoeveelheid waterdamp in die atmosfeer. Daarna word 'n metode vasgestel wat die sterk punte van beide die datastelle besit. Hierdie nuwe datastel moet vir beide die weerkondisies (wind en water damp) gekorrigeer wees. As dit moontlik is, sal dit die akkuraatheid van neutronmonitordata dwarsoor die wêreld grootliks verbeter.

Sleutelwoorde: `neutron monitor, dispersie,`
`GNSS, atmosferiese druk`
`GPS, kosmiese strale`

Nomenclature

List of key terms and abbreviations

AU	Astronomical Unit
CME	Coronal Mass Ejection
DoD	United States Department of Defense
GCR	Galactic Cosmic Ray
GLONASS	Global Orbiting Navigation Satellite System
GNSS	Global Navigation Satellite System
GPS	Global Positioning System
HartRAO	Hartebeesthoek Radio Astronomy Observatory
HCS	Heliospheric Current Sheet
HMF	Heliospheric Magnetic Field
KWV	Kuemmel Water Vapour
LISM	Local Interstellar Medium
NAVSTAR	Navigation System with Timing and Ranging
NCEP	National Centers for Environmental Prediction
NWU	North-West University
PTE	Parker Transport Equation
PWV	Precipitable Water Vapour
SAWS	South African Weather Services
SLR	Satellite Laser Ranging
SMF	Solar Magnetic Field
USP	Unit for Space Physics
VLBI	Very Long Baseline Interferometry
ZTD	Zenith Tropospheric Delay

Contents

Chapter 1

Introduction

Galactic cosmic rays (GCRs) are energetic atomic nuclei produced in our galaxy. When propagating through the heliosphere they are affected by the solar magnetic field embedded in the outward flow of the solar wind. This interaction between particles and solar effects is called the modulation of cosmic rays. Furthermore, when the GCRs encounter the magnetic field of the earth, they get deflected by an amount that is determined by their rigidity (momentum per charge). If this rigidity is below the so-called cut-off rigidity, they can not penetrate through the geomagnetic field to the surface. When entering the atmosphere of Earth the GCRs collide inelastically with the nuclei of air molecules, these collisions forming a cascade of secondary nuclear active particles, the number being determined by the thickness of the atmosphere, and hence the atmospheric pressure.

From 1948 to 1951 J.A Simpson developed what is commonly known today as the neutron monitor (*Simpson*, 2000). These neutron monitors are long-term cosmic-ray detectors able to detect the secondary nuclear active particles from the cosmic-ray particle cascade. In the beginning of the 1960s a network of about a 100 neutron monitors was established in a grid on Earth, but according to *Shea and Smart* (2000) these numbers have reduced to approximately 40 presently. The decrease in operating neutron monitors is mainly due to space missions being able to measure the energy spectra of cosmic rays directly, which is not possible with neutron monitors.

A neutron monitor's counting rate is sensitive to atmospheric pressure, and therefore corrections of the pressure variations are important. These pressure measurements are affected by wind through the so-called Bernoulli effect. A study was done by *Malan and Moraal* (2002)

on this effect, showing that the Bernoulli effect describes only a fraction of the wind effect on pressure measurements. In the same paper it is suggested that technology like the Global Positioning System (GPS) may also be used to correct, or eliminate, for this effect.

In collaboration with the Hartebeesthoek Radio Astronomy Observatory (HartRAO) Space Geodesy Programme it was brought to our attention that GPS technology may now have become accurate enough to be used to correct for this wind effect on pressure readings near neutron monitors. A GPS signal is delayed by the ionosphere and neutral atmosphere of the earth. The ionospheric delay can readily be calculated, but the tropospheric part of the delay is highly variable due to the highly variable precipitable water vapour (PWV) in the atmosphere. *Combrink* (2003) and *Combrink* (2006) studied this effect of the PWV on the signal.

The main aim of this dissertation is twofold: firstly to use the data of a barometer and the GPS to find a combined data set of pressure which is corrected for wind speed and PWV (absolute humidity). This combined set will greatly increase the accuracy of the pressure correction on neutron monitor data, and may even be used in other applications in industry. Secondly, this study is focused on the SANAE IV neutron monitor. Therefore, the environmental effects at the SANAE IV base in Antarctica will be studied in greater detail. A quantitive opinion will be given on the possibility of certain research projects benefiting from the environmental conditions there.

In Chapter 2 some basic concepts of heliospheric physics are introduced which are important in understanding the need for accuracy on the neutron monitor counting rate. In the first place, cosmic rays and their potential for revealing the various properties of the heliosphere, e.g. the solar wind and magnetic field, are discussed. This is followed by a brief history of the development of cosmic-ray detectors, with emphasis on neutron monitors. Thereafter, the effect the atmospheric pressure has on neutron monitor counting rates and how this is corrected for, is investigated. Finally, the different types of barometers used with the neutron monitors are described.

The theme of this study is how to avoid wind effects on atmospheric pressure readings which have to be used to correct neutron monitor data. In order to do so, Chapter 3 is devoted to discussing the wind effect on atmospheric pressure, and how it may be compensated for. This chapter has a threefold purpose. Firstly, a review is given of earlier work that was done in this

regard by *Maletsoa* (2000) and *Malan and Moraal* (2002). Thereafter, a full derivation is given of the Bernoulli effect according to *Choudhuri* (1998). Finally, this effect is used, and following the data analysis method of *Malan and Moraal* (2002), it is shown that it does not fully account for the wind effect observed at the SANAE IV base.

In Chapter 3 it is stated that the Bernoulli effect was not effective in quantifying the wind speed problem, and therefore the results are not satisfying. In *Malan and Moraal* (2002) it is suggested that GPS technology should be considered to find a suitable solution to determine the atmospheric pressure. Chapter 4 is devoted to justify why GPS may be able to eliminate the wind speed problem, and to explain how such a GPS works. Firstly, justification for the ability of the GPS to eliminate the wind effect will be discussed. Then a short history is given on the GPS and how it was developed. After that a discussion on the different types of Global Navigation Satellite System (GNSS) follows, as well as the basic components of these systems. Finally, the method to determine the position of a receiver, and the applications of the system are discussed.

In Chapter 5 a detailed discussion is given on the atmospheric characteristics that influence GPS signals. The first part will focus on the derivation and meaning of the Clausius-Clapeyron relation and water vapour equation. Finally, discussions are presented on the delay of the GPS signal due to the troposphere and ionosphere.

The main idea of the data analysis method is to find a method able to eliminate the precipitable water vapour (PWV) and wind effect on pressure by integrating the two data sets and finding a corrected data set. In *Malan and Moraal* (2002) the Bernoulli effect was found only to describe 38% of the effect of wind on the pressure data. GPS-pressure results are not affected by wind, but by PWV. PWV measurements are very low at SANAE IV base, and therefore it should be suitable spot for the data analysis. In Chapter 6 the reasons for using the specific location, and instrumentation are discussed. Then the simple regression plots between the different pressure methods are discussed, and lastly the different water vapour pressure equations are compared to find the best way to include water vapour. Chapter 7 is devoted to conclusions.

Chapter 2

Cosmic rays and their detectors

2.1 Introduction

In this chapter some basic concepts of heliospheric physics are introduced, which are important in understanding the need for accuracy on the neutron monitor counting rate. Firstly, cosmic rays and their potential for revealing the various properties of the heliosphere, e.g. the solar wind and magnetic field, are discussed. This is followed by a brief history of the development of cosmic-ray detectors, with emphasis on neutron monitors. Thereafter, the effect the atmospheric pressure has on neutron monitor counting rates and how this is corrected for, are investigated. Finally, the different types of barometers used with the neutron monitors are described.

2.2 Cosmic rays

Galactic cosmic rays are charged particles, with energies ranging from 10^8-10^{15} eV, which are formed outside our solar system. Higher energy cosmic rays, up to $\sim 10^{20}$ eV, are probably of extragalactic nature. They propagate into the heliosphere and get modulated by the effects of the sun; i.e. the heliospheric magnetic field (HMF) embedded in the solar wind, coronal mass ejections (CMEs) and solar flares. When the GCRs enter the heliosphere, they propagate along the HMF, which is transported outwards by the solar wind. Because the GCRs are tied to the magnetic field lines, it is possible to extract information about the structure of the heliosphere from cosmic-ray observations.

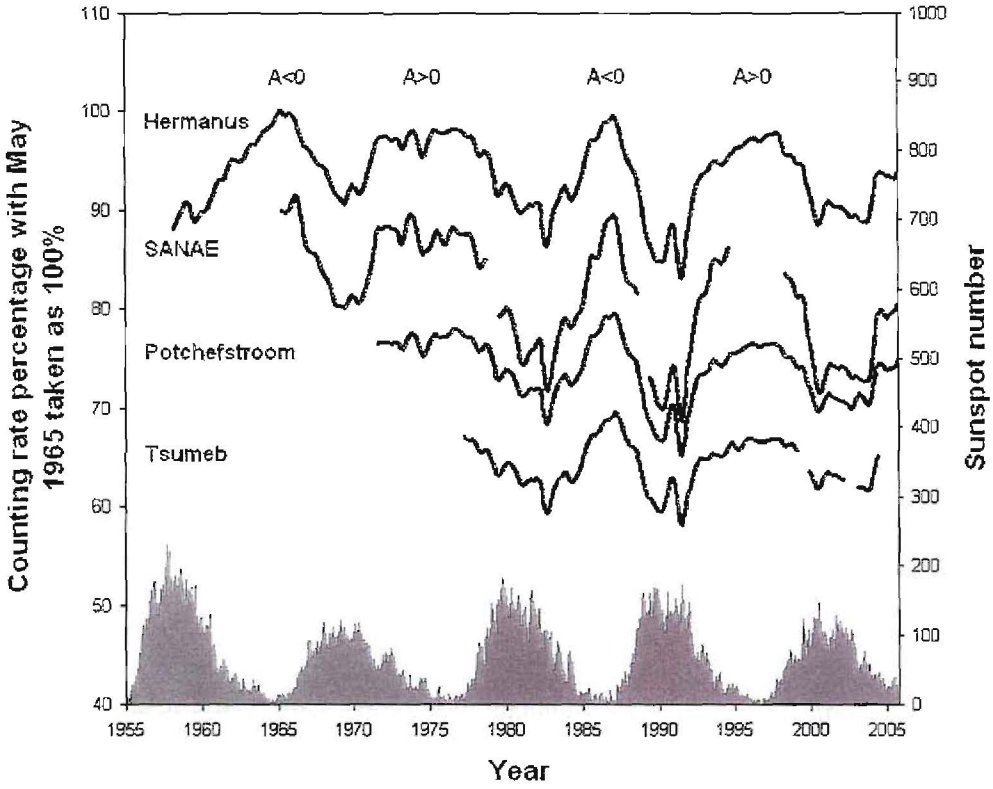

Figure 2.1: The counting rate for the four NWU neutron monitors together with the sunspot number. The sunspot number is anti-correlated with the counting rate, and it shares an 11-year periodicity. The two peaks (1965, 1987) and two plateaus (1976, 1997) are caused by the bipolar magnetic field of the sun.

Figure 2.1 shows the counting rate of the four North-West University (NWU) neutron monitors, together with the sunspot number for that period of time. The counting rate for each monitor was normalized to have a counting rate of 100% in May 1965. For clarity, factors of 10, 20, and 30% are subtracted from the counting rates of the SANAE IV, Potchefstroom and Tsumeb monitors respectively. There is a clear anti-correlation between the sunspot number and neutron monitor counting rates, which is called modulation due to variations in solar activity. The Hermanus monitor has four maximum and four minimum values for the counting rate. The solar activity is at a maximum (minimum) every 11 years, and therefore is referred to as the 11-year solar cycle. The $A > 0$ and $A < 0$ signs on top of the individual cycles designate a property of the solar magnetic cycle. These counting rates form peaks in 1965 and 1987, and plateaux in 1976 and 1997, due to particle drifts, as described in Section 2.5.2. These peaks (plateaux) occur every 22 years, and they are caused by the bipolar solar magnetic field reversing polasity every 11 years.

According to *Simpson* (1992) the cosmic rays reaching earth, consist of 98% nuclei (entirely

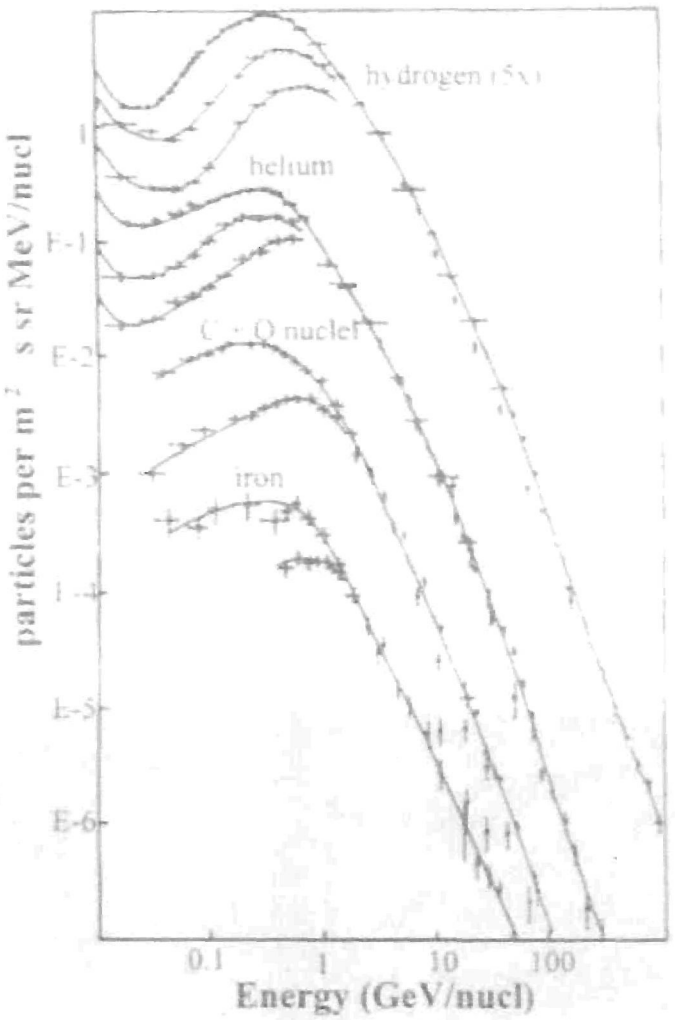

Figure 2.2: Energy spectra of galactic cosmic rays. Five different species of cosmic rays are shown. For energies below a few GeV three curves can be distinguished. They are for solar minimum (upper curve), average (middle curve), and solar maximum (lower curve). Adapted from *Meyer et al.* (1974).

stripped of their electrons) and 2% electrons and positrons. In the energy range 10^8-10^{10} eV/nucleon, the composition of the nuclei is 87% hydrogen, 12% helium and 1% heavier nuclei. For each of these species of cosmic-ray particles, an energy spectrum can be constructed from spacecraft observations, as shown in Figure 2.2.

Solar modulation is the time-dependent change of the intensity of cosmic rays in the heliosphere, due to the changes in solar activity. Figure 2.1 shows the modulation which is the changes in intensity for the counting rates. The abundance of Helium and Hydrogen at low energies has three different values, as seen in Figure 2.2. The high values are for solar minimum, the middle values are for the average conditions, and the lowest values for solar maximum.

2.3 Solar wind

Solar energy is produced by nuclear fusion. This energy propagates through radiation and convection towards the surface. When reaching the solar surface, the plasma gets accelerated radially outwards and is referred to as the solar wind. *Parker* (1958) shows that the solar wind is accelerated to supersonic speeds. With increasing radial distance its internal pressure decreases. At some radius the pressure drops so low that the flow becomes subsonic by going through a shock transition. This shock is called the termination shock and was first proposed by *Parker* (1961). According to *Stone et al.* (2005) Voyager 1 crossed this termination shock at 94 AU on 16 December 2004, while *Nasa* says that Voyager 2 did so on August 30, 2007. When the pressure equals that of the local interstellar medium (LISM), a boundary called the heliopause is formed. The distance to the heliopause, according to *Ferreira and Scherer* (2004), is 140 AU from the sun in the nose direction.

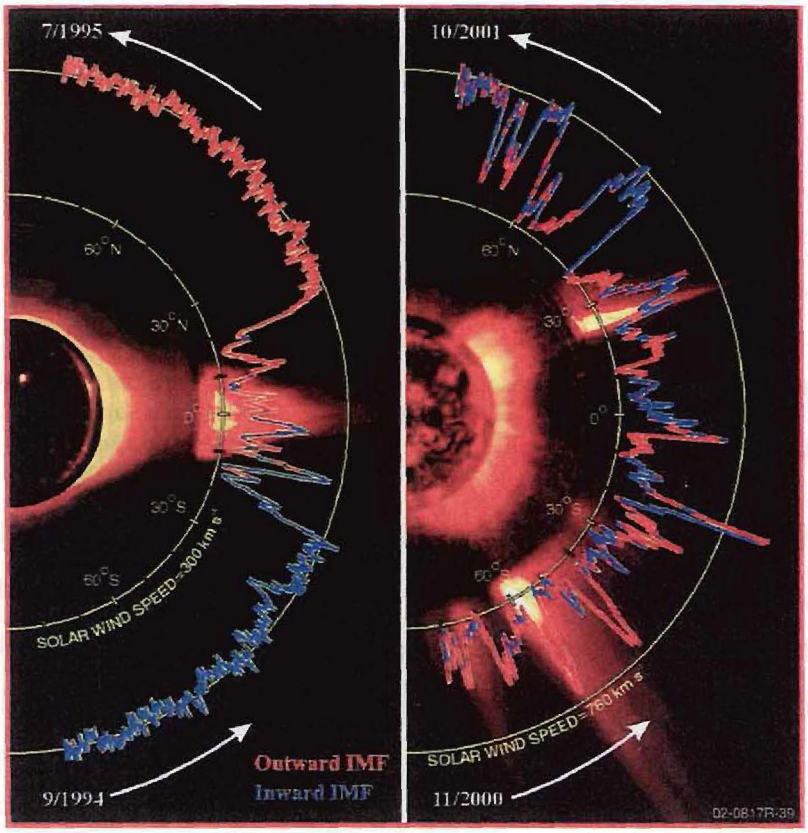

Figure 2.3: The latitude dependence of the solar wind speed as observed by Ulysses. The left panel was observed during a quiet solar period, with the right hand panel observed during an active solar period. Adapted from http://solarprobe.gsfc.nasa.gov/solarprobe_science.htm.

Figure 2.3 shows the solar wind speed data for the Ulysses mission. The solar wind speed

was found to be latitude dependent. During a quiet solar period *Goldstein et al.* (1995) found that Ulysses observed a solar wind speed of ~450 km/s in the region near the solar equator. From 5° S to 35° S the average wind speed increased to ~700 km/s. In the next 20° it increased to ~750 km/s, and from there on it remained constant. During an active solar period the wind speed fluctuates between ~400 km/s and ~800 km/s, but on average is more uniform as function of heliolatitude.

2.4 The Heliospheric magnetic field

The solar magnetic field (SMF) is generated by the dynamo effect inside the sun. When the SMF exits through the photosphere it gets bundled up. Sunspots are formed through the shear force created by the SMF. The sunspots are therefore an indication of the SMF strength, which is generally proportional to the activity of the sun.

The solar wind is a highly energetic plasma, forcing the SMF radially outwards. When the magnetic field is beyond the corona it is called the HMF. Three models for the HMF are currently used in heliospheric physics. The first of these is the Parker spiral field proposed by *Parker* (1958), and has the form of an Archimedes spiral. The second model, proposed by *Fisk* (1996), called the Fisk field, looks like a string on a rotating ball. The last model, proposed by *Krüger* (2005), is called the hybrid model. It is formed by making use of both the previous models.

According to *Jokipii and Thomas* (1981) the magnetic and rotation axes of the sun do not coincide, and therefore a wavy heliospheric current sheet (HCS) is formed. This structure is transported radially outward by the solar wind, and is important for modulation in the heliosphere. Figure 2.5 shows the HCS to be the wavy line on the equatorial plane.

2.5 Propagation of Particles in the Heliosphere

2.5.1 The Parker transport equation

The propagation of cosmic rays in the HMF discussed above is described by the Parker transport equation (PTE) which was derived by *Parker* (1965). The PTE is given by:

$$\frac{\partial f}{\partial t} = -\mathbf{V} \cdot \nabla f + \nabla \cdot (\mathbf{K}^{\mathrm{S}} \cdot \nabla f) - \mathbf{v}_d \cdot \nabla f + \frac{1}{3}(\nabla \cdot \mathbf{V}) \frac{\partial f}{\partial \ln P} + Q_{source} \tag{2.1}$$

where $f(\mathbf{r}, P, t)$ is the cosmic-ray distribution function dependent on position $\mathbf{r}$, rigidity P, and time t. $\mathbf{K}$ is the diffusion tensor, $\mathbf{V}$ the solar wind velocity, and Q_{source} possible sources of cosmic rays inside the heliosphere.

The PTE describes the time rate of change, $\partial f / \partial t$ as due to:
(1) Outward convection of particles due to the HMF embedded in the solar wind.
(2) Spatial diffusion relative to the HMF.
(3) Drift of particles due to the gradient and curvature of the HMF.
(4) Energy changes, whether it be due to adiabatic heating or cooling, or acceleration at shocks.
(5) Possible sources of cosmic rays inside the heliosphere, e.g. the Jovian cosmic ray source.

2.5.2 Diffusion

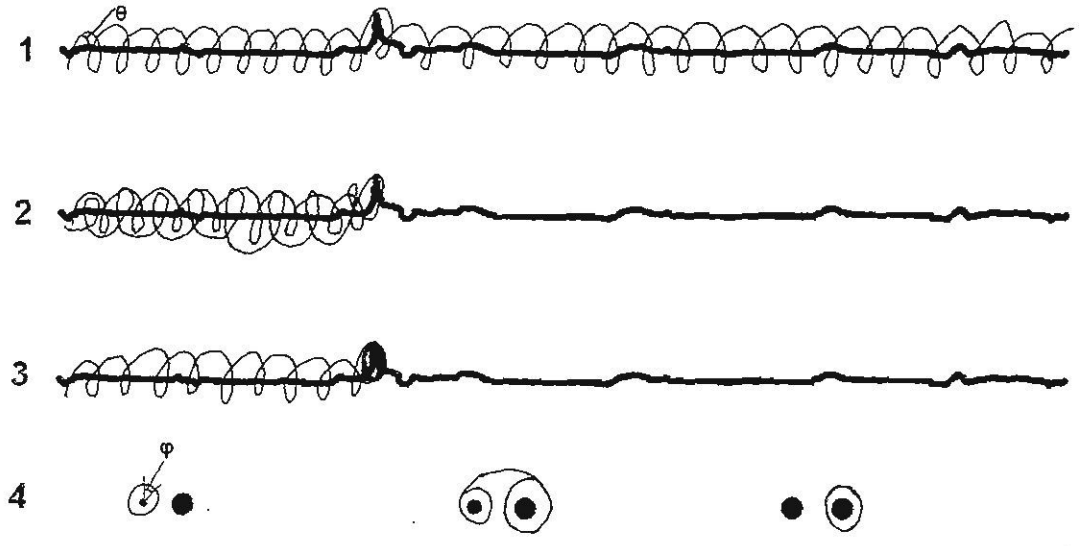

Figure 2.4: Schematic representation of diffusion of charged particles in an irregular magnetic field.

Diffusion is the consequence of frequent random collisions between particles in a ensemble. In such a case it is not practical to describe the motion of individual particles, and therefore only the collective behaviour (ensemble) of particles is described. When working with an ensemble of particles a distribution function is used to describe the collective properties of the particles. It is essential to note that diffusion does not only depend on the spatial distribution of particles, but also on the distribution of particles in momentum space.

For an appropriate example, the scenario of cosmic rays propagating along the HMF will be discussed. In this kind of scenario the scattering points in the HMF have the same effect on a particle traveling along it, as a particle colliding with another particle.

Figure 2.4 shows four possible paths of a particle gyrating down a magnetic field line. The black lines indicate a typical magnetic field line; they are uneven because of the irregularities of the solar wind transporting the HMF outwards. In this case our magnetic field only has one significant irregularity for simplicity. A particle gyrates along this magnetic field line, and when it interacts with the irregularity its pitch angle (θ) changes. That is the angle between the magnetic field line and the propagation of the particle along it. A particle path is mainly determined by how the phase angle (φ) is orientated towards an irregularity on the magnetic field line. The first three paths describe parallel diffusion of particles along the HMF. The first particle path is that of a particle finding an unrestricted way through the irregularity along the magnetic field line. The second particle path is that of a particle interacting with the irregularity and its pitch angle is forced through 90°; the particle turns around heading in the opposite direction. On its way backwards it may interact with another of these irregularities and get turned back. The average length a particle travels before turning around is called the mean fee path (λ). The third particle path is that of a particle in such a position that its pitch angle is equal to 90°. The particle stays on one spot having no movement along the HMF, this is shown by the third particle path. Perpendicular diffusion, which may occur from paths one to three, is most easily discussed with the help of sketch four. The last particle path is when a particle gets such a phase angle that it may leave the current magnetic field line and jump to another line. This is due to the fact that the magnetic field line strength is irregular. This is an example of how perpendicular diffusion can occur. Another way for perpendicular diffusion to occur is through the random walk of the magnetic field itself.

Kallenrode (2001) shows how the effect of diffusion can be expressed mathematically. Assume

that the particle distribution is Gaussian in space, and view a scenario with a density gradient. The density gradient ensures a situation with anisotropy, meaning that the diffusion streaming is directed. The streaming of particles is described by

$$\mathbf{S}_{\parallel} = -\kappa_{\parallel}(\nabla f)_{\parallel}, \tag{2.2}$$

and

$$\mathbf{S}_{\perp} = -\kappa_{\perp}(\nabla f)_{\perp}, \tag{2.3}$$

with $\kappa_{\parallel}$ and $\kappa_{\perp}$ the respective diffusion coefficients parallel and perpendicular to the magnetic field, and f the particle distribution function. From (2.2) and (2.3) the diffusion tensor can be defined as

$$\kappa = \begin{pmatrix} \kappa_{\parallel} & 0 & 0 \\ 0 & \kappa_{\perp} & \kappa_A \\ 0 & \kappa_A & \kappa_{\perp} \end{pmatrix}.$$

where κ_A is the coefficient describing drift effects(described in Section 2.5.5). The gradient is the force behind the current density, where the current density is directly proportional to the gradient. The mobility of the particles is described by the diffusion tensor. When the magnetic field lines have very few or no irregularities, the parallel diffusion is very effective, and $\kappa_{\parallel}$ becomes so large that there is no use in determining its value. When the magnetic field lines have too many irregularities, $\kappa_{\parallel}$ becomes smaller, while $\kappa_{\perp}$ becomes larger, until they become equal. This then results in anisotropic diffusion.

2.5.3 Convection

Convection is an important part in the transport of a particle, because the HMF is frozen into the solar wind and it gets transported outwards. The cosmic rays get transported along the HMF, and therefore are convected. Therefore, the streaming of a particle, as discussed in the previous subsection is twofold. According to *Kallenrode* (2001), (2.2) needs to be corrected with another term $\mathbf{S}_{conv} = f\mathbf{V}$, giving

$$\mathbf{S} = f\mathbf{V} - \kappa\nabla f, \tag{2.4}$$

where $\mathbf{V}$ is the convection flow velocity. Inserting (2.4) into the equation of continuity, it follows

$$\frac{\partial f}{\partial t} = -\nabla \cdot (f\mathbf{V}) + \nabla \cdot (\kappa \nabla F) = -\mathbf{V} \cdot \nabla f + \nabla(\kappa \nabla F) - \nabla \cdot \mathbf{V} f. \tag{2.5}$$

The first two terms are similar to (2.1).

2.5.4 Energy losses

Cosmic rays get trapped at the scattering points of the HMF. These field lines move radially outwards and cause the cosmic rays trapped at different field lines to recede in latitude and longitude. In essence this is a classic scenario of adiabatic energy loss. *Gleeson* (1978) shows that this adiabatic rate of momentum loss in the frame of the solar wind is $\langle \dot{p} \rangle = (p/3)\nabla \cdot \mathbf{V}$. In the frame of the earth, which is a fixed frame, the adiabatic momentum loss is $\langle \dot{p} \rangle = (p/3)\mathbf{V} \cdot \nabla f/f$. Here p is the momentum, $\mathbf{V}$ the solar wind velocity and f the cosmic-ray distribution function. It can be shown that these momentum changes lead to the well-known adiabatic relation $PV^{\gamma} = c$, where P is the pressure, and V the volume (Moraal, private communication).

2.5.5 Particle drifts

Although Parker includes particle drifts in the PTE, they were neglected until a study by *Jokipii et al.* (1977). They point out that drifts are sensitive to the polarity of the HMF, and therefore their inclusion could alter modulation. The drift velocity is given by *Steenkamp* (1995) as:

$$\langle v_d \rangle = \frac{|\,q\,|}{q} A \nabla \times \frac{\beta R}{3B} \mathbf{e_B} \tag{2.6}$$

where $\mathbf{e_B} = \mathbf{B}/B$, R is the Rigidity, and $\frac{|q|}{q} = +1$ for nuclei and -1 for electrons. In one 11-year period the vector $\mathbf{e_B}$ points outwards in the northern hemisphere and inward in the southern hemisphere. This has generally become known as the $A > 0$ drift cycle, and is shown in Figure 2.5 and the symbols on the top of Figure 2.1. In the subsequent 11-year cycle the field direction, and therefore the drift direction, is reversed.

Figure 2.5 shows the drift for positively charged particles; for negatively charged particles the drift is just in the the opposite direction. For the $A > 0$ polarity cycle, positively charged particles drift from the polar regions towards the ecliptic plane. For this cycle the particles

are mostly unaffected by the changes in the ecliptic plane, which are mainly due to changes in the waviness of the HCS. For the $A < 0$ cycle the positive particles drift along the HCS and outwards towards the polar regions. For this cycle particles are greatly affected by the tilt angle of the HCS. Figure 2.1 shows that in the $A > 0$ cycles the cosmic-ray maxima formed plateaux in the neutron monitor counting rate and the $A < 0$ cycle, peaks in the neutron monitor counting rate.

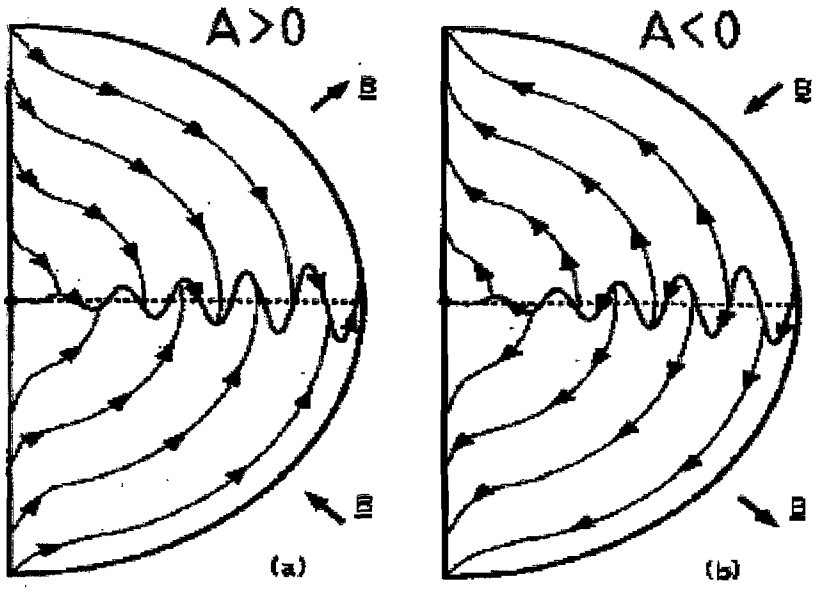

Figure 2.5: The drift of positively charged particles in the heliosphere is due to the curvature and gradient of the HMF. The drifts for $A > 0$, and $A < 0$ polarity are shown. It is in the opposite direction for negatively charged particles. Adapted from *Jokipii and Thomas* (1981).

2.6 Short-term variations

Variations in the cosmic-ray intensity of a few minutes to several days are termed short-term variations. In this section a discussion is given of Forbush decreases, ground level enhancements (GLEs), diurnal variations and 27-day variations. Figure 2.6 shows three of these commonly occurring short-term variations. Firstly, the Forbush decrease is the sharp decline and gradual recovery of the counting rate. Secondly, the GLE is the spike in the counting rate. Finally the diurnal variations are shown by the increase and decrease of the counting rate over daily periods.

2.6.1 Forbush decreases

A Forbush decrease refers to a short-term decrease in the counting rate of a neutron monitor. According to *Cane* (2000) two basic types occur, they are non-recurrent decreases and recurrent decreases. The non-recurrent decreases are caused by temporary interplanetary events such as CMEs. *Lockwood* (1971) found that recurrent decreases are more symmetrical, and have a more gradual onset than non-recurrent decreases.

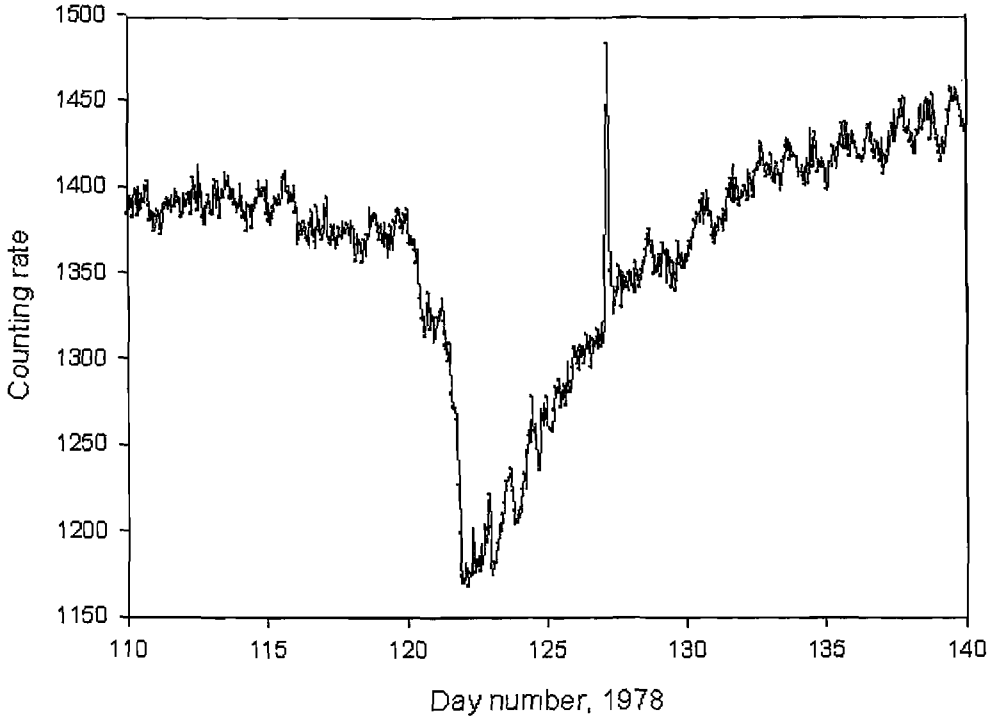

Figure 2.6: The decrease in the counting rate of a neutron monitor is called a Forbush decrease. The spike in the counting rate is termed a GLE. The daily variation in the counting rate are known as diurnal variations. This event was recorded by the SANAE neutron monitor in May 1978.

A CME is a massive plasma explosion on the sun. This explosion contains a magnetic field which pushes away any charged particles in front of it. It is this property of a CME that causes the cosmic-ray intensity to drop. Figure 2.6 shows that the descending phase of the decrease has two stages. The first decrease is usually a decrease in the vicinity of 2% and it is caused by the interplanetary shock moving past the observer. The second decrease has a magnitude of ~5% and this happens when the observer goes into the injecta driving the shock (*Kallenrode*, 2001).

2.6.2 Ground level enhancements

The first GLE was recorded on 28 February 1942. Such an event is caused when a particle ejection from the sun is so large that it overshadows the normal GCR intensity. At the SANAE IV base in Antarctica such an event, GLE number 69, occurred on 20 January 2005 and is shown in Figure 2.7. In this figure there is a three-peak structure which gives insight on the propagation of cosmic rays in the inner heliosphere; for a detailed discussion see *McCracken et al.* (2008).

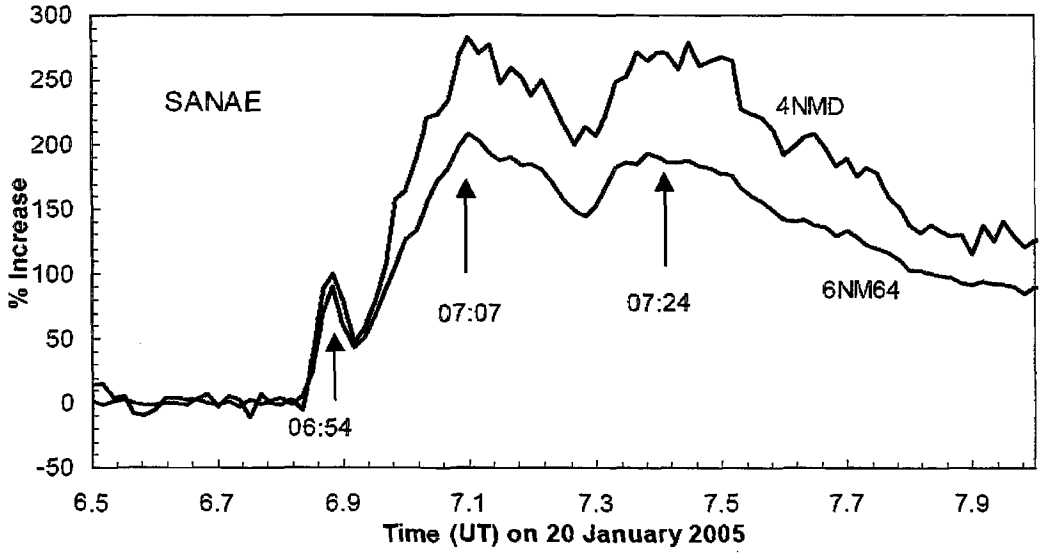

Figure 2.7: GLE number 69 as detected by the neutron monitor (6NM64) and the neutron-moderated detector (4NMD) at the SANAE IV base. Adapted fom *McCracken et al.* (2008).

2.6.3 Diurnal variations

As the earth rotates around its axis, a neutron monitor on the surface is able to make a pitch angle measurement of the distribution of cosmic rays in the heliosphere. The flow of cosmic rays is anisotropic in the heliosphere, and this causes a diurnal variation in the neutron monitor counting rate. The magnitude and direction of the flow, as well as the variation with the 11-year and 22-year solar cycle, provides important observational data. According to *Bieber and Pomerantz* (1991) these observational data can be used to test theories on cosmic ray transport in the heliosphere. Furthermore, information on the radial and latitudinal gradients of cosmic rays can be derived through use of these data, in accordance with the cosmic ray transport

equations.

2.6.4 27-day variations

The solar activity on the surface of the sun has a longitudinal dependence. The sun takes, on average, 27 days to rotate once around its axis. Therefore if the solar activity is viewed from the earth, a 27-day variation in cosmic-ray intensity is seen. It is found that each rotation has a maximum and minimum cosmic-ray intensity. The (synodic) Bartels period of 27 days, which was detected in the variation of geomagnetic indices by *Chapman and Bartels* (1940), is consistent with many other solar properties. Periods close to this one are detected in the interplanetary magnetic field (*Svalgaard and Wilcox*, 1975), magnetograms (*Bumba and Howard*, 1969), and sunspot distribution (*Balthasar and Schuessler*, 1983).

2.7 First cosmic ray detectors

An Austrian physicist, Victor Hess, discovered cosmic rays while conducting a balloon flight in 1912. On this specific flight he had an ionization chamber, to make measurements of the energetic particles. From these observations he proposed a theory in which high-energy particles collide with the nuclei of air molecules. In these collisions secondary charged particles are formed which are detected by ionization cambers. These collisions are depicted in Figure 2.8 and consist of three components. They are the electromagnetic, meson, and nucleonic components, of these three components: some detectors only detect the nucleonic part. In Figure 2.9 the number of secondary particles is shown. The number increases exponentially with altitude until it reaches an altitude of ~18 km. This is because the secondary particles get absorbed by the air molecules. From 18 km upwards the number of secondary particles decreases because the cosmic rays have not yet formed the secondary particles at an optimal rate.

The first cooperative attempt to measure cosmic rays on ground level was done by using ionization chambers. Ionization chambers were very large and expensive, and it was difficult to calculate the counting rate from the observations. Furthermore, the statistical accuracy of the chambers on the counting rate was low. Neutron monitors, which will be discussed in detail in Section 2.10, have higher counting rates. This attribute increases the statistical accuracy on

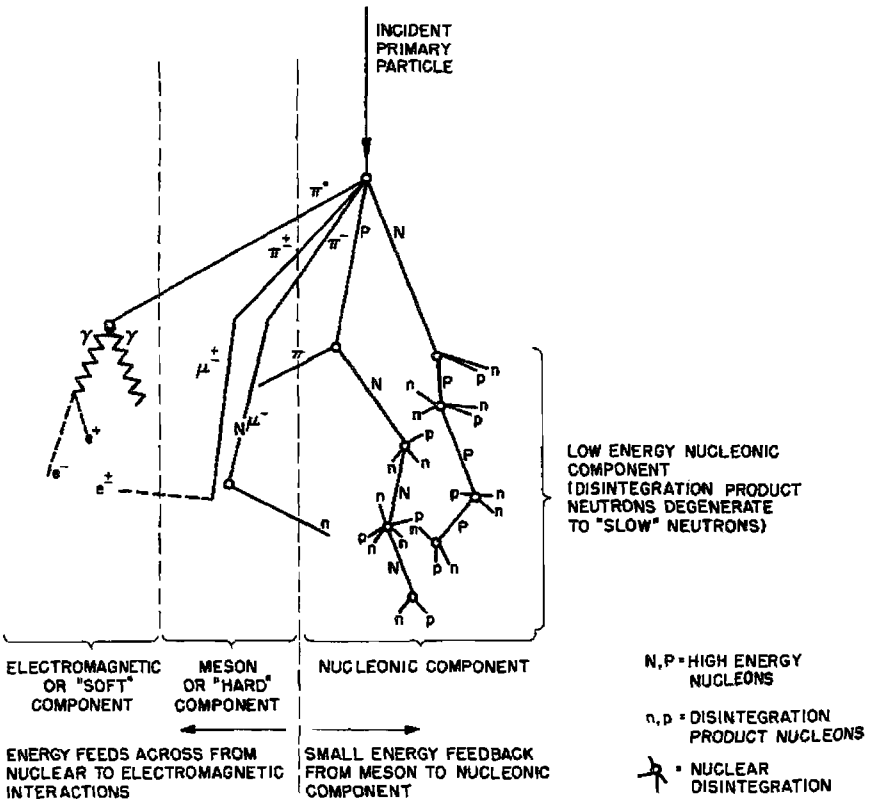

Figure 2.8: When a cosmic ray enters the atmosphere of the earth it collides with the nuclei of air molecules, forming a shower of secondary particles. For neutron monitor studies only the nucleonic component is of importance. Adapted from http://www.ngdc.noaa.gov/stp/SOLAR/COSMIC_RAYS/*cosmic.html*.

the counting rate significantly, making the neutron monitor the superior detector.

2.8 Spacecraft

One of the more recent ways to detect lower energy cosmic rays are on spacecraft and satelites. They are able to detect cosmic rays at different positions in the heliosphere. There are numerous missions of importance to cosmic-ray modulation studies; e.g. the Ulysses, Voyager 1, Voyager 2, IMP 8, Pioneer 10, and Pioneer 11 missions. This section gives some discussion on the Ulysses and Voyager missions.

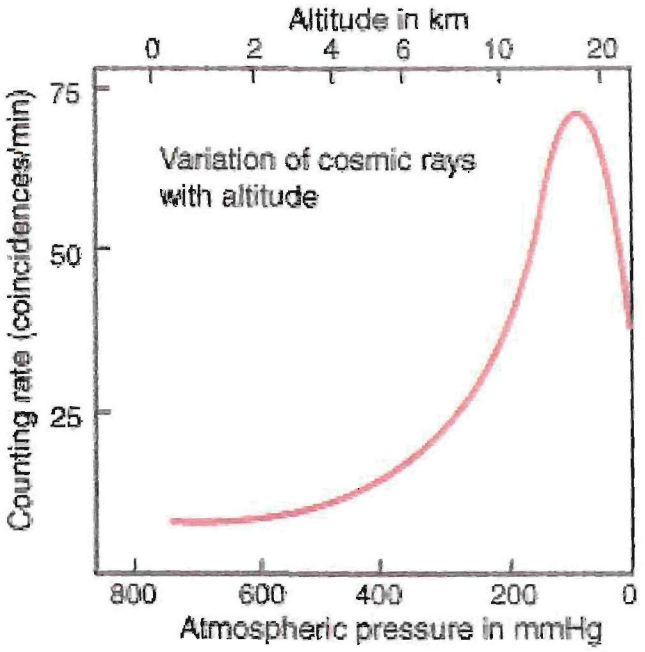

Figure 2.9: The intensity of the secondary particles due to the cascade caused by the inelastic collisions of cosmic rays with air molecules. This variation was first discovered by Pfotzer in 1936. Adapted from http://hyperphysics.phy-astr.gsu.edu/hbase/astro/cosmic.html.

2.8.1 Ulysses

The Ulysses spacecraft was launched on 6 October 1990 and was the first spacecraft ever launched to do detections over the poles of our sun. It gathered data explaining the dynamics of the inner heliosphere.

It was launched in the ecliptic plane where it stayed until it reached Jupiter. Its direction was changed by the gravitational force of Jupiter, and it headed back towards the sun, going over its poles. Ulysses reached the highest southernmost point of its orbit around the sun near the solar minimum conditions in 1994. From here it moved to the northern pole which it reached one year later.

Ulysses was a very successful spacecraft mission, and has given information about the inner heliosphere, especially the latitudinal dependence of the solar wind. The solar wind speed results it obtained are shown in Figure 2.3. An in-depth discussion is given by *Marsden and Marsden* (1995); *Marsden* (2001); *Balogh et al.* (2001); *Smith et al.* (2003) and *Smith and Marsden* (2003).

2.8.2 Voyager missions

The two Voyager spacecraft were launched in 1977. They are probes with a variety of scientific instruments to detect certain properties of the heliosphere. Both the spacecraft examined Jupiter and Saturn, as well as their moons. Voyager 2 also went on to make observations of both Neptune and Uranus. They were launched in the general direction of the nose of the heliosphere, as seen in Figure 2.10. They detected shocks in the heliosphere with the most important of these the termination shock. According to *Decker et al.* (2005) and *Stone et al.* (2005) Voyager 1 crossed the termination shock on 16 December 2004, and according to *Nasa* Voyager 2 crossed the shock on August 30th 2005. These two spacecraft still need to cross the heliopause.

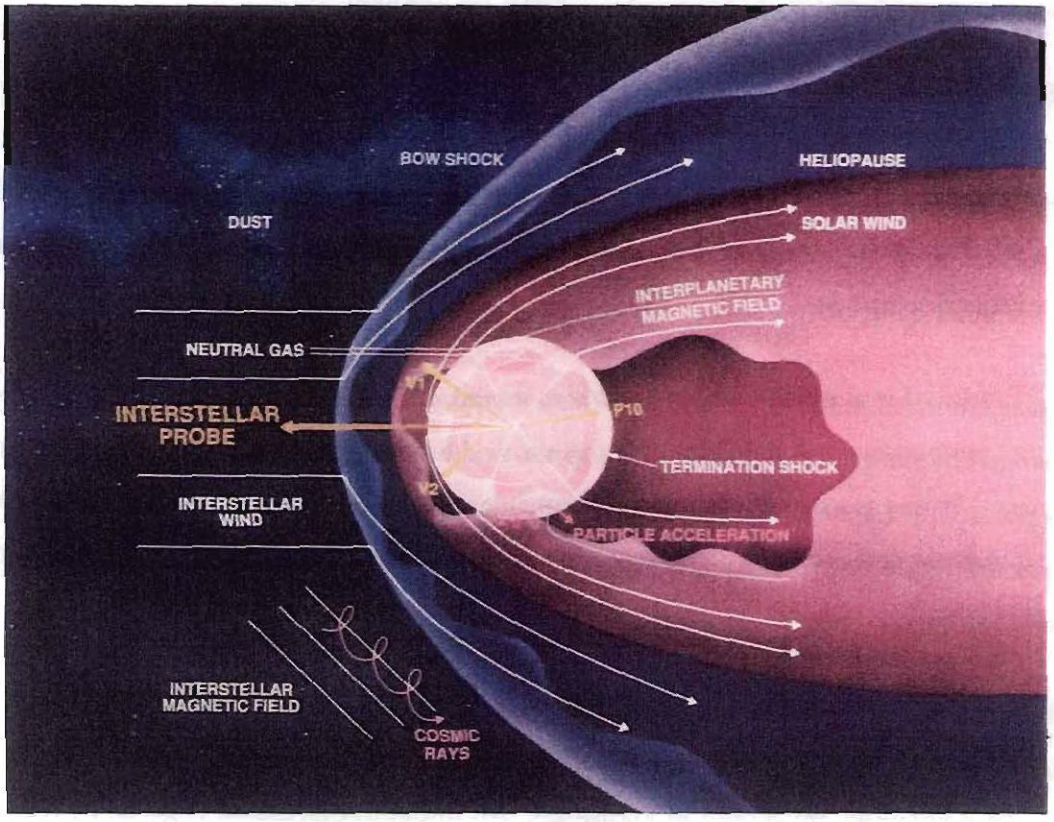

Figure 2.10: This is an illustration of the form of the heliosphere. The bow shock, termination shock, heliopause, and the paths of the Voyager 1, and 2 spacecraft are indicated. Adapted from http://interstellar.jpl.nasa.gov/.

2.9 Neutron monitors

In the late 1940s the physicist J.A. Simpson started to develop a detector to measure the cosmic-ray flux. In the early 1950s he succeeded in constructing such a instrument and called it the neutron monitor. The first monitor was put in practical use in 1954, at Climax, Colorado. From this period onwards many neutron monitors were stationed all over the world, and these constitute a neutron monitor network.

Spacecraft missions are very important in order to find the latitudinal and longitudinal dependence of various variables in the heliosphere. They are also able to measure the spectrum of various cosmic-ray species in the heliosphere. The problem with spacecraft is that when they are launched to collect data from the heliosphere, they have a limited lifespan. Secondly, they are very expensive to launch. This is not true for neutron monitors because, compared to spacecraft, they are relatively inexpensive, and very easy and cheap to maintain. However neutron monitors are affected considerably by environmental effects, as described in Section 2.11.

The geomagnetic field bends the ray paths of high energy particles near the earth. This effect may be so large that some particles get bent away from the earth when their energy is too low. Thus a particle needs a minimum energy, called the cut-off rigidity, to be able to reach the surface of the earth. Rigidity is defined as $R = pc/q$, where p is the momentum, c the speed of light in a vacuum and q the charge of the particle. The cut-off rigidity increases with decreasing latitude from the poles, with maximum value at the equator. Table 2.11.3 shows some values for the cut-off rigidity. The acronyms IGRF and DGRF stand for International or Definitive Geomagnetic Reference Field respectively.

Table 2.11.3: Calculated vertical cutoff rigidities (GeV) for the NWU's neutron monitors. Adapted from Krüger (2006).

NWU Stations	1980 IGRF model	1980 DGRF model	1995 IGRF model
Hermanus	4.55	4.58	4.45
Potchefstroom	6.94	7.00	6.85
Sanae	0.86	0.86	0.75
Tsumeb	9.15	9.21	9.06

When cosmic rays enter the atmosphere of the earth they get deflected away from its surface when below the cut-off rigidity. In essence neutron monitors then measure all the particles above a certain rigidity or energy level. Therefore, it is difficult to calculate energy spectra by making use of neutron monitors. Cosmic-ray spectra for different species are readily measured by spacecraft. However there are two ways to find energy spectra by way of neutron monitor data. The first is to do a latitudinal survey by ship or airplane; details of such surveys are given in *Krüger* (2006). Secondly, to intercalibrate the neutron monitor network, which was the main aim of *Krüger* (2006). A calibration neutron monitor was designed and is currently employed to produce the desired result. If the calibration works, 50 years of neutron monitor spectra data will be possible.

2.10 Atmospheric effects on neutron monitor counting rates

2.10.1 Definition of the barometric coefficient β

Figure 2.8 shows that the intensity of the secondary particles, in our case the nucleonic part, is affected in some way or another by the amount of air molecules it passes through. The amount of air molecules is directly proportional to the atmospheric pressure, and therefore it is possible to derive the effect of the atmospheric pressure on the counting rate. The fractional change of the counting rate N is proportional to the change in the pressure P

$$\frac{\triangle N}{N} = -\beta \triangle P. \tag{2.7}$$

Let this change be infinitesimal, and integrate both sides to find

$$\int dN/N = -\beta \int dP. \tag{2.8}$$

From (2.8) it follows

$$N = c_1 e^{-\beta P}. \tag{2.9}$$

By further assuming that when $N = N_0$, when $P = P_0$ it follows

$$N = N_0 e^{-\beta(P-P_0)}, \tag{2.10}$$

where P_0 is usually taken as the average pressure at the neutron monitor. The quantity β is called the barometric coefficient, and this is an indication on how the counting rate changes with pressure for that specific station.

2.10.2 Calculating the barometric coefficient β

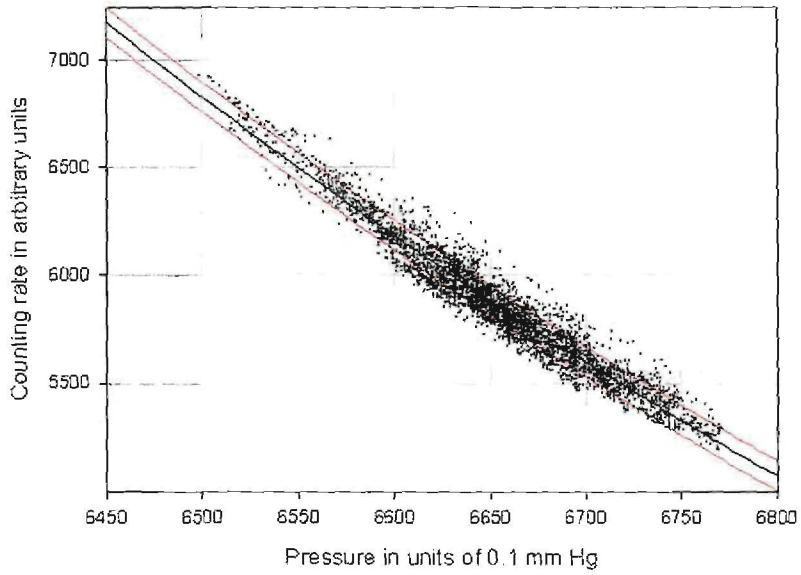

Figure 2.11: The relation between the counting rate of the SANAE IV neutron monitor and the atmospheric pressure at the neutron monitor. The red lines indicate that 67% of the data points lie between them, and the value of β is equal to 1.000 ± 0.004 %/mmHg.

The variations in cosmic-ray intensity due to modulation and other interplanetary occurrences are small, $\leq$10%. Due to this, one wants to eliminate all other effects as to enhance the interplanetary effects. It is for this reason that the atmospheric pressure effects need to be eliminated; this is done via the barometric coefficient. Figure 2.11 shows a plot of the cosmic ray intensity of the SANAE IV neutron monitor as function of atmospheric pressure. The regression line has a slope of approximately -1% per mm Hg. This implies that when the pressure increases by 1 mm Hg the counting rate of the neutron monitor decreases by about 1%. For a

neutron monitor with a counting rate in the order of $10^5 - 10^6$ counts per hour the statistical uncertainty is between 0.1%-0.3%, and if the value of β is 1%/mmHg then from (2.10) it follows that the atmospheric pressure should be accurate to at least 0.3 mmHg, to get uncertainties due to pressure variations smaller than those due to true cosmic rays variation.

2.10.3 The effects of variables on the barometric coefficient

Bachelet et al. (1968) show that the barometric coefficient β is not a constant but varies due to effects such as cutoff rigidity, atmospheric pressure and altitude. This section will give an overview of each of these properties.

The effect of cutoff rigidity

Various studies have been made on the effect of the cutoff rigidity on the barometric coefficient, amongst these authors are *Carmichael and Bercovitch* (1969), *Raubenheimer* (1972), *Bachelet et al.* (1972), and *Raubenheimer and Stoker* (1974). In all these studies it was found that β decreases with increasing cut-off rigidity. The value of β for the cut-off rigidity at the equator is more than 10% lower than at the poles. This is due to the fact that more low-energy particles are able to enter over the poles due to the low cut-off rigidity. These particles are more easily absorbed than high-energy particles, and causes β to have a higher value.

The effect of altitude

The effect of altitude on β is threefold. From Figure 2.9 the first two effects are explained. The figure shows that for altitudes between 0 and 15000 m the intensity increases with increasing altitude. This causes β to increase with increasing altitude. The second effect is for altitudes above 15000 m. The secondary particles are not fully produced yet. Therefore β decreases with increasing altitude. The third effect according to *Bachelet et al.* (1965) is caused by stopping muons in the atmosphere. The stopping muons contribute exponentially to β with decreasing altitude. Therefore, the stopping muons have no effect at the top of the atmosphere. At lower altitudes they do have an effect, and according to *Raubenheimer* (1972) this effect causes a decrease in β with decreasing altitude.

The effect of the solar cycle

In numerous studies, e.g. *Shatashvili and Rogava* (1995) and *Dorman et al.* (1997) it was shown that there is a rough anti-correlation between β and solar activity. Therefore β is low (high) during solar maximum (minimum). The 11-year intensity variation is due to primary spectrum changes. For solar maxima the spectrum is harder. This does not mean the spectrum has shifted to a higher energy, it rather indicates that the low-energy particles are deflected away by modulation more effectively from the earth. Thus the spectrum just consists of more high-energy particles during the maxima period. These particles are more difficult to absorb, and therefore β is ~3% lower at solar maxima than at solar minima.

The effect of atmospheric temperature

Neutrons are generated in the lead covering around the neutron counters of the monitor through nuclear interactions. These interactions occur when fast particles pass through the lead absorber. In a study by *Dorman* (1972) it was found that heated lead nuclei become unstable to generate neutrons in the lead covering.

In a study by *Harman and Hatton* (1968) it was shown that an increase in upper atmospheric temperature results in a decrease in the neutron monitor counting rate. The correction on the counting rate according to *Dorman* (1972) can be made by

$$N_0 = N(1 - C_T \delta T), \tag{2.11}$$

where N_0 is the counting rate corrected for atmospheric temperature, and N the pressure corrected counting rate. Furthermore $\delta T = T - \bar{T}$, where $T = \sigma D_i \Delta p_i t_i$, t_i is the temperature of the i^{th} pressure level in the atmosphere, Δp_i is the pressure thickness. The quantities D_i are temperature heights applied to each level, $\bar{T}$ is a reference temperature, and C_T is the temperature coefficient.

Iucci (1999) shows that the value of C_T = -0.037%/°C. This then tells us that if the temperature changes by ~ 10°C then the counting rate changes by ~0.4%. This is four times larger than the statistical error on the counting rate, but on the long term this will not cause a serious drift in counting rate.

2.11 Pressure equipment at USP neutron monitor stations

The importance of the pressure readings when correcting the counting rate of a neutron monitor has already been argued. Therefore a discussion follows on the different types of barometers that were used or are in use at the four neutron monitor stations that are under the control of the USP at NWU.

2.11.1 Mercury barometer

A standard mercury barometer consists of a glass tube which is filled with mercury and an open mercury-filled reservoir. The mercury column balances the pressure of the air on the reservoir. The higher the air pressure the higher the mercury is pushed up into the glass tube. For low air pressure the mercury in the glass tube flows into the reservoir, leaving less mercury in the tube.

This instrument was first devised in 1643 by Evangelista Torricelli, and has since resulted in many variations such as the basin, siphon, wheel, cistern, Fortin, multiple folded, stereometric, and balance barometers. The mercury barometer measures air in units of mmHg. The equivalence of one atmosphere is 760 mmHg, which is a unit still commonly used today.

The problem of this type of barometer is that it is very sensitive to temperature changes in the atmosphere. This is attributed to the fact that mercury's density decreases with increasing temperature and increases with decreasing temperature. Until about 15 years ago, they were the standard barometers at most neutron monitors.

2.11.2 Aneroid barometer

This type of barometer consists of a cell or a set of interconnected cells. Each cell is sensitive to the air pressure, which expands or compresses the cell. Inside these cells are stiff springs which are sensitive to these changes, and therefore amplify the effect of the air pressure.

These cells are very sensitive to ambient temperature. To compensate for this, the aneroids are usually submerged into an oil bath at constant temperature.

2.11.3 Paroscientific barometer

The sensor of the Paroscientific digital barometer, is a piezo electric crystal which releases electricity when a force is applied to it, in this case air pressure. The manufacturers of this type of barometer specify that the drift of this equipment is smaller that 0.013 mmHg per year, which is 10 times smaller than the accuracy that is needed. This type of barometer is very easy to use, and only minimally sensitive to temperature. It is currently used at most neutron monitors.

In this study, an evaluation is made of the GPS to determine whether it is accurate enough so that it can replace physical barometers to do pressure corrections on neutron monitors.

Chapter 3

The wind effect at the SANAE IV base

3.1 Introduction

The theme of this study is how to avoid wind effects on atmospheric pressure readings which have to be used to correct neutron monitor data. In order to do so, this chapter is devoted to discussing the wind effect on atmospheric pressure, and how one may be able to compensate for it. The content of this chapter is threefold. Firstly, a review is given about earlier work that was done in this regard by *Maletsoa* (2000) and *Malan and Moraal* (2002). Thereafter, a full derivation is given of the Bernoulli effect according to *Choudhuri* (1998). Finally, this effect will be used, and following the data analysis method of *Malan and Moraal* (2002), it will be shown that it does not fully account for the wind effect observed at the SANAE IV base.

3.2 The effect of wind on atmospheric pressure

In a study by *Maletsoa* (2000) it was found that wind indeed affects the counting rate of the SANAE IV neutron monitor station. He shows that when comparing the ratio between two monitors, it is possible to get an idea of the magnitude of environmental effects.

As an example Figure 3.1 shows the pressure-corrected counting rate, as well as the ratio between the SANAE IV and Hermanus neutron monitors for the period of March to April 1998. The ratio should be constant to some degree, because both counting rates have the same tendencies due to modulation. According to *Maletsoa* (2000) the standard deviation on the hourly counting rates of the SANAE IV and Hermanus monitors are 0.12% and 0.15% respectively.

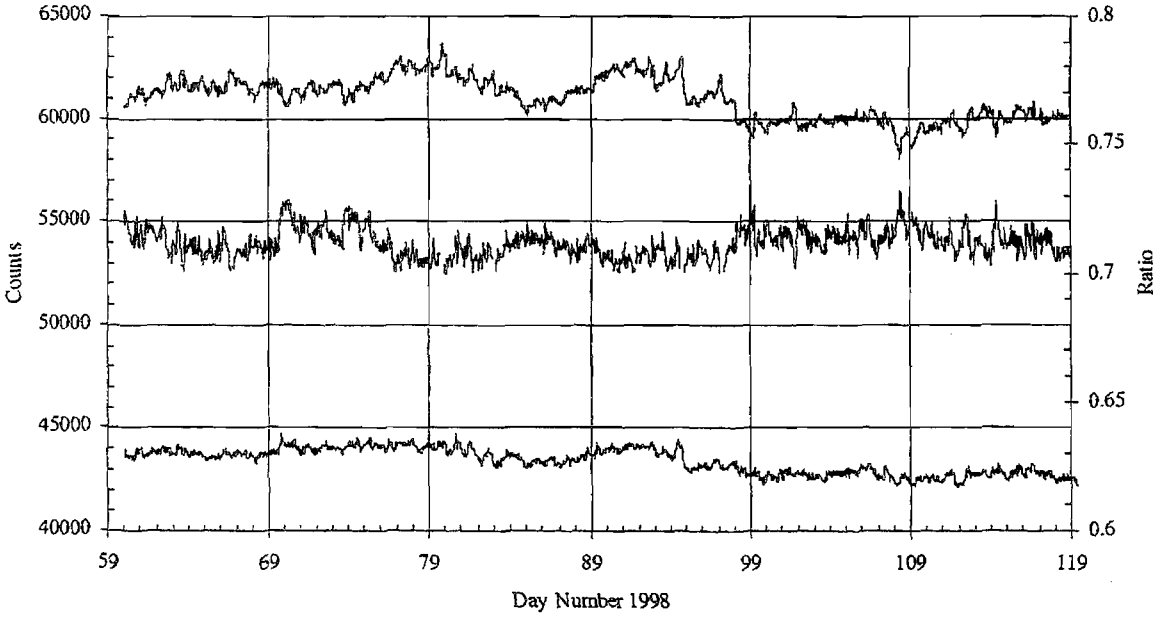

Figure 3.1: SANAE IV neutron monitor (top) and Hermanus neutron monitor (bottom) hourly counting rates (divided by 10) with their ratio given by Hermanus/SANAE (middle) from day 60 to 119 in 1998. Adapted from *Maletsoa* (2000).

From these values it is calculated that the statistical fluctuations on the ratio should be consistently within 0.19%.

Figure 3.2 shows both the ratio (on an expanded scale) and wind speed. The statistical fluctuation boundaries for the ratio are shown. The fluctuations on the ratio are several times larger than the purely statistical value. There are many possible reasons for these large fluctuations. They may be of atmospheric, geomagnetic or heliospheric nature, and wind effects present only one possibility. As far as heliospheric effects are concerned, the modulation at Hermanus is less than at SANAE due to the difference in geomagnetic cutoff. To reduce this effect the fluctuations of the Hermanus counting rates were multiplied by a factor 1.3 in order to make them the same size as those of SANAE. It is not immediately clear that the fluctuations in the ratio are related to the wind speed.

By no means, however, is this effect new to the study of neutron monitor counting rates. *Maletsoa* (2000) indicates that according to private communication between himself and *Humble* the wind effect has already been intensively studied from the 1950s. In a study on the Mawson neutron monitor, it was found that a correlation existed between pressure corrected counting

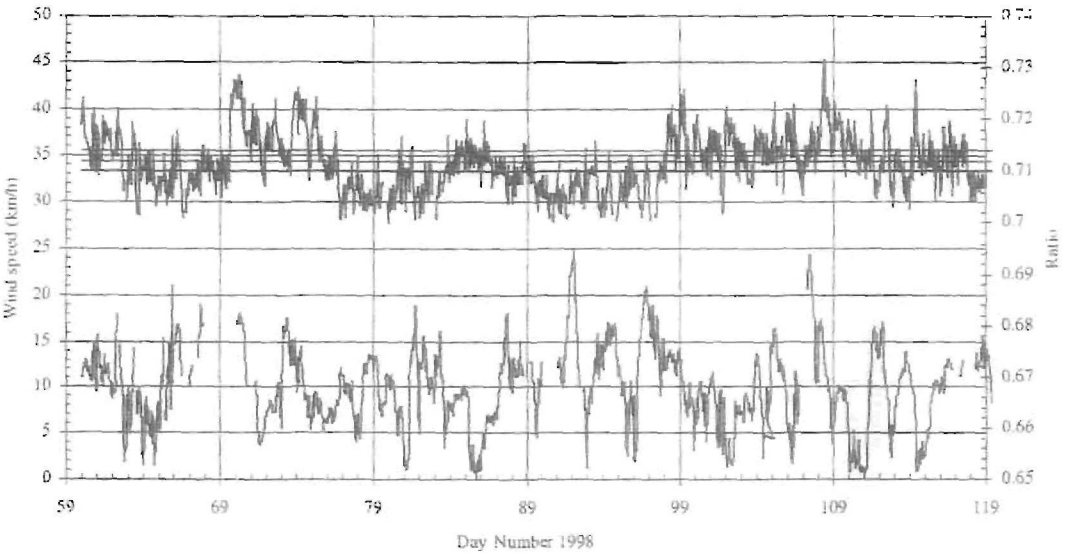

Figure 3.2: Hermanus/SANAE IV (top), with the wind speed (bottom), for days 60 to 119 in 1998. Adapted from *Maletsoa* (2000).

rates and wind speed. The correlation appeared to be quadratic. At wind speeds below 18 m/s the effect was not significant, while above that value the effect was important, with a 1% reduction in counting rate at ~31 m/s. This effect had some dependence on the direction of the wind. Figure 3.3 shows that 10% of the wind-speed data is above 18 m/s at SANAE IV. In this figure, one is also able to see that the most probable wind speed is 8-12 m/s.

Studies on the same subject include, among others, *Fujita and Otani* (1952), *Lockwood and Calawa* (1957), and *Suda and Kodama* (1963). The authors conclude that even though a barometer is installed in a room exposed to high wind speed, it does not properly indicate the undisturbed ambient pressure due to the aerodynamic effect of winds. Numerous attempts have been made to construct a barometer which can eliminate this wind effect. *Kodama et al.* (1967) suggest that the best sensor would be hexahedral shaped. At the SANAE IV base a static pressure head supplied by *Shulman* (1997) is used. In theory it should eliminate the wind effect, but does not, as will be shown later Section 3.4.

Figure 3.4 shows the calculated barometric coefficients, β, introduced in Section 2.11. In this case four barometric coefficients are calculated. The bottom one of these is β for the Pochefstroom monitor. This monitor is in a low-wind environment, and is hardly affected by wind speeds above 18 m/s. The other three plots are all data for the SANAE IV neutron monitor.

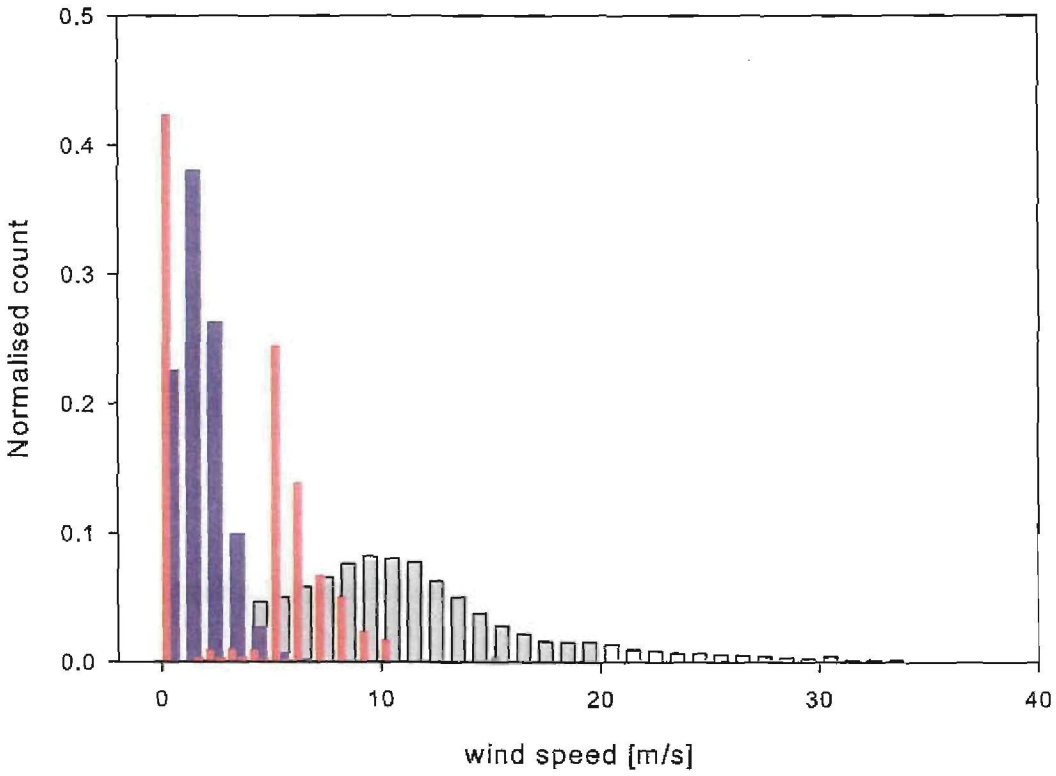

Figure 3.3: Histogram of wind speeds at the SANAE IV base, Nelspruit and Sutherland. The red bars are for Sutherland, the blue bars Nelspruit, and the gray bars for SANAE IV. The counting rates have been normaised in such a way that the total amount of data points will be one.

Each of these plots was corrected with different pressure data. From bottom to top they are Bernoulli-corrected, outside and inside pressure. The outside pressure was measured with the static pressure head, and the inside pressure by a barometer inside the base. The Bernoulli corrected pressure is in essence the outside pressure with $1/2\rho v^2$ added to each pressure measurements, as it is believed that this accounts for laminar flow in the static pressure head. *Malan and Moraal* (2002) state that the wind effect on β is twofold; the barometric coefficient at the SANAE IV base had a much larger standard deviation than at the Potchefstroom neutron monitor. Furthermore, the pressure variations at SANAE were at least three times larger than at Potchefstroom, which makes pressure corrections more uncertain. This is corroborated by Figure 3.3 which shows that the wind speeds at a station such as SANAE IV are exceptionally high. In this figure the wind speeds supplied by the South African weather services (SAWS) are shown for the three stations SANAE IV, Sutherland and Nelspruit. This clearly shows that stations typically find themselves in much more moderate locations than at SANAE IV. For

the Sutherland and Nelspruit stations the wind speed data is from 1998 till 2006, while for the SANAE monitor only data from 2000 till 2006 can be plotted.

In studies by *Malan and Moraal* (2002) and *Maletsoa* (2000) a method of implementing Bernoulli's effect to describe the data is applied. To study their methods, the Bernoulli effect will be derived.

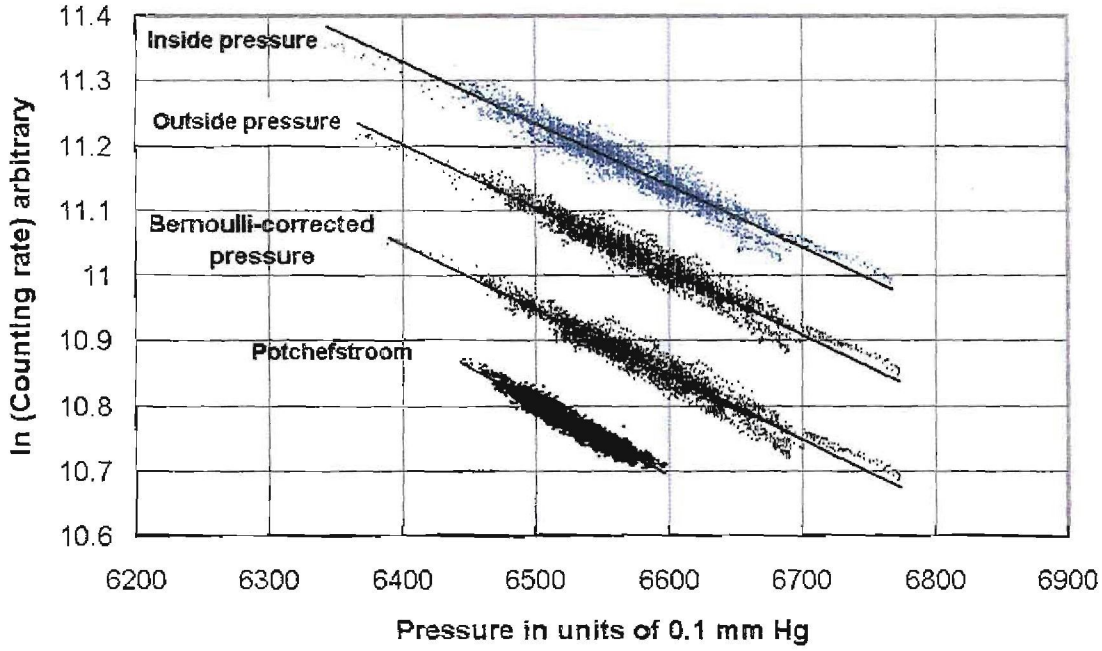

Figure 3.4: Regression curves of the logarithm of hourly counting rate of Potchefstroom and SANAE IV neutron monitors respectively. The SANAE IV counting rates were determined using three different pressure corrections, as indicated by the top three regressions. Adapted from *Malan and Moraal* (2002).

3.3 The Bernoulli effect

The effect of bulk motion of a fluid on its pressure is called the Bernoulli effect. In understanding certain principles of this effect, it is useful to derive it from first principles. The derivation follows from *Choudhuri* (1998).

Consider a fluid element with a volume element δV, density ρ, velocity v, and mass $\rho\delta V$. Newton's second law of motion states

$$\rho\delta V\frac{d\mathbf{v}}{dt} = \delta\mathbf{F}_{volume} + \delta\mathbf{F}_{surface}, \tag{3.1}$$

where the acceleration of the fluid element is the Lagrangian derivative ($d\mathbf{v}/dt$). The total force is divided into two parts, the volume force ($\delta\mathbf{F}_{volume}$) and the surface force ($\delta\mathbf{F}_{surface}$). The volume force is that force that works in on all points inside the body of the fluid. The surface force on a fluid element is the force acting on it across the surface bounding the fluid element.

Because the volume force works in on all points within the body, the force can be written as

$$\delta\mathbf{F}_{volume} = \rho\delta V\mathbf{F}, \tag{3.2}$$

where the force $\mathbf{F}$ is the body force per unit mass.

The surface force is by definition the force that works in on a surface element $d\mathbf{S}$. This force is proportional to the area it works on, and because both the force and the surface elements are vectors, the relation needs to be written as a second-rank tensor. This relation is

$$(d\mathbf{F}_{surface})_i = -P_{ij}dS_j, \tag{3.3}$$

where

$$P_{ij} = \begin{pmatrix} P_{11} & P_{12} & P_{13} \\ P_{21} & P_{22} & P_{23} \\ P_{31} & P_{32} & P_{33} \end{pmatrix}.$$

The total surface force can be found by integrating over the surface of the fluid volume, that is

$$(\mathbf{F}_{surface})_i = -\oint P_{ij}dS_j. \tag{3.4}$$

From Gauss's theorem the above equation can be rewritten in a volume integral, that is

$$(\mathbf{F}_{surface})_i = -\int \frac{\partial P_{ij}}{\partial x_j}dV. \tag{3.5}$$

The surface force on the volume element δV is then given by

$$(\delta\mathbf{F}_{surface})_i = -\frac{\partial P_{ij}}{\partial x_j}\delta V. \tag{3.6}$$

by substituting (3.6) and (3.2) into (3.1) it follows

$$\rho\frac{d\mathbf{v}}{dt} = \rho\mathbf{F} - \frac{\partial\mathbf{P}_{ij}}{\partial\mathbf{x}}\delta V. \tag{3.7}$$

It is an experimentally established fact that a fluid in static equilibrium has a surface force that works perpendicular on the fluid element area. Mathematically, for such a static fluid the relation is

$$P_{ij} = P\delta_{ij}. \tag{3.8}$$

This is just the diagonal of the second-order tensor P_{ij}, and when substituted into (3.3) it follows that

$$d\mathbf{F}_{surface} = -Pd\mathbf{S}, \tag{3.9}$$

where P is the pressure, defined as the force acting per unit area.

For a fluid with internal motions, (3.9) does not hold. Furthermore if (3.8) is substituted into (3.7) it follows that

$$\rho\frac{dv_i}{dt} = \rho F_i - \frac{\partial P_i}{\partial x_i}. \tag{3.10}$$

By making use of the relation between the Lagrangian and Eulerian derivatives, which is

$$\frac{dQ}{dt} = \frac{\partial Q}{\partial t} + \mathbf{v}\cdot\nabla Q, \tag{3.11}$$

(3.10) becomes

$$\frac{\partial \mathbf{v}}{\partial t} + (\mathbf{v}\cdot\nabla)\mathbf{v} = -\frac{1}{\rho}\nabla P + \mathbf{F}. \tag{3.12}$$

This is known as the Euler equation. Using the vector identity

$$(\mathbf{v}\cdot\nabla)\mathbf{v} = \frac{1}{2}\nabla(\mathbf{v}\cdot\mathbf{v}) - \mathbf{v}\times(\nabla\times\mathbf{v}), \tag{3.13}$$

the Euler equation can be written in the form

$$\frac{\partial \mathbf{v}}{\partial t} + \frac{1}{2}\nabla(\mathbf{v}\cdot\mathbf{v}) - \mathbf{v}\times(\nabla\times\mathbf{v}) = -\frac{1}{\rho}\nabla P + \mathbf{F}. \tag{3.14}$$

Assuming that the ideal fluid has a steady flow -that is a flow which is independent of time- and further that the volume force on the fluid is conservative, that is

$$\mathbf{F} = \nabla\Phi,$$

(3.14) becomes

$$\nabla(\frac{1}{2}v^2) - \mathbf{v}\times(\nabla\times\mathbf{v}) = -\frac{1}{\rho}\nabla P - \nabla\Phi. \tag{3.15}$$

With fluids in motion, it is important to describe the motion of a fluid element. The path along which a fluid element moves is called a streamline. When integrating along such a streamline,

it is possible to describe the motion of the fluid element. If $d\mathbf{l}$ is a line element of the streamline, (3.15) becomes

$$\int d\mathbf{l} \cdot [\nabla(\frac{1}{2}v^2) - \mathbf{v} \times (\nabla \times \mathbf{v}) + \frac{1}{\rho}\nabla P + \nabla\Phi] = 0. \tag{3.16}$$

Noting that the line element $d\mathbf{l}$ and velocity $\mathbf{v}$ are parallel to each other, the term $d\mathbf{l} \cdot \mathbf{v} \times (\nabla \times \mathbf{v})$ is eliminated, and (3.16) becomes

$$\frac{1}{2}v^2 + \int \frac{dP}{\rho} + \Phi = c, \tag{3.17}$$

where c is a constant. The term $\int dP/\rho$ is to be evaluated from a reference point on the streamline to another point where all the other variables are considered. This result is known as the Bernoulli principle. Assuming that the fluid is incompressible, and the potential force is dependent on the height and the gravity working in on the fluid element, $\Phi = gh$, then

$$\frac{1}{2}\rho v^2 + P + \rho gh = c, \tag{3.18}$$

along a streamline in the incompressible fluid. This is known as the Bernoulli equation for an incompressible fluid, as used in the subsequent work.

3.4 Bernoulli effect at SANAE

This section will now show to what extent the wind effect at the SANAE IV base is due to the Bernoulli effect.

The Bernoulli effect (3.18) can in our specific case be rewritten as

$$\frac{1}{2}\rho v_1^2 + \rho g h_1 + p_1 = \frac{1}{2}\rho v_2^2 + \rho g h_2 + p_2, \tag{3.19}$$

where the subscript 1 is for the inside barometer and the subscript 2 for the static pressure head barometer. If we assume that $h_1 = h_2$ then (3.19) reduces to

$$p_2 - p_1 = \frac{1}{2}\rho(v_1^2 - v_2^2). \tag{3.20}$$

Furthermore the static pressure head should, in theory, eliminate the wind speed and therefore $v_2 = 0$. From this (3.20) becomes

$$\Delta p = \frac{1}{2}\rho v_1^2, \tag{3.21}$$

where $\Delta p = p_2 - p_1$.

The ideal way to test the Bernoulli effect is to plot measured differences in the pressure of the two barometers against $\frac{1}{2}\rho v^2$, as was done by *Malan and Moraal* (2002). The pressure readings of the two barometers are affected by the wind speeds at each location. There is no indication of how much the static pressure head corrects for this wind effect, therefore the graph of $p_2 - p_1$ versus $\frac{1}{2}\rho v^2$ is plotted.

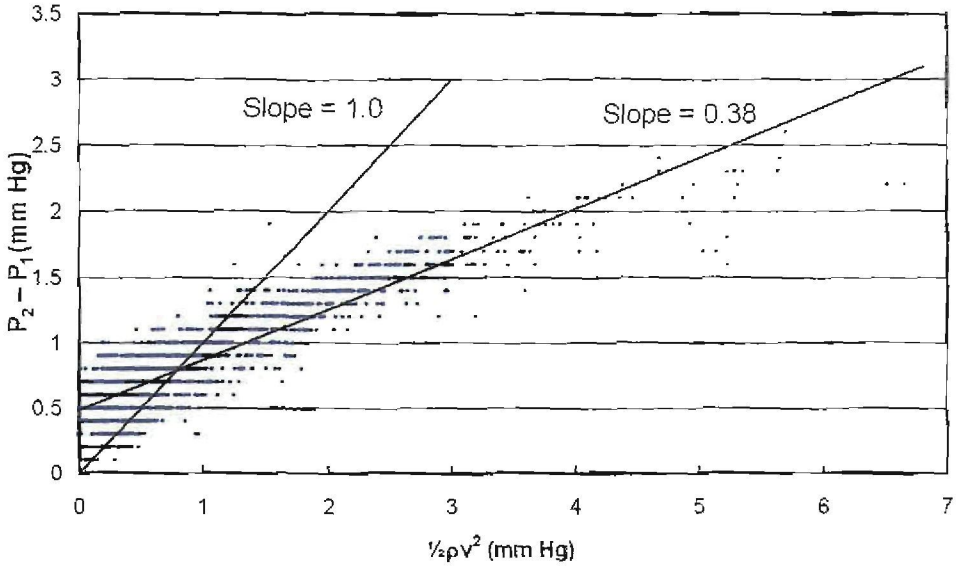

Figure 3.5: The difference between external and internal pressure ($P_2 - P_1$) against $1/2\rho v^2$. This graph gives an indication of the effect of the static pressure head. The slope = 1.0 line is for the Bernoulli effect fully describing the wind effect. The slope = 0.38 line is the actual average slope of the data. Adapted from *Malan and Moraal* (2002).

Figure 3.5 shows two lines, the line with a slope equal to one is that line which describes the Bernoulli effect, according to (3.21). That is, if the data points can be described by this line, then the Bernoulli effect is 100% responsible for the difference between the two pressures. This is not the case, as the line best describing the data points has a slope of 0.38. This then indicates that the fraction of Bernoulli effect the static pressure head "sees" is only 38%.

3.5 Conclusion

In this chapter it was shown how large an effect wind has on the atmospheric pressure as measured by barometers. It was also shown how the Bernoulli effect may accommodate for this effect, from *Malan and Moraal* (2002) and *Maletsoa* (2000). But this Bernoulli effect analysis does not give a satisfactory result. The reason for not getting the same results as with the

Mawson neutron monitor is unknown. In view of this unsatisfactory situation, one is forced to consider an alternative method. In the next chapter the GPS will be introduced as an alternative barometer that is not susceptible to wind effects.

Chapter 4

The Global Positioning System (GPS)

4.1 Introduction

The main theme of this dissertation is to find a method to eliminate the effect that wind has on atmospheric pressure readings, so one is able to properly correct the counting rate of neutron monitors. In Chapter 3 the Bernoulli effect was not effective in quantifying the wind speed problem, and therefore the results where not satisfying. In *Malan and Moraal* (2002) it is suggested that GPS technology should be considered to find a suitable solution to determine the atmospheric pressure. This chapter is devoted to justifying why GPS may be able to eliminate the wind speed problem, and how GPS works. Firstly, the basic principle of GPS is described. Then a short history is given on GPS and how it was created. After that a discussion about the different types of GNSS follows, as well as the basic components of these systems. Finally, the method to determine the position of a receiver, and the applications of the system are discussed.

4.2 The GPS principle

When an electromagnetic wave travels through a medium its speed is dependent on the refractive index of that medium. Suppose a signal gets sent perpendicular to the earth's surface, then it is possible to calculate the time it will take to reach the surface. The value of the pressure P at sea level is 1 atmosphere, which in turn can be written as 1013.25 hPa. Furthermore this can be rewritten as $1.01\text{x}10^5$ Nm^{-2}, which is $1.02\text{x}10^5$ kgm^{-3}. Since the density of air at sea level

is 1.299 kgm^{-3}, the total thickness of the atmosphere is approximately $1.02x10^4$ $kgm^{-2}/1.299$ kgm^{-3} = 7852 m. This is the thickness that the atmosphere would have if it had the same density as at sea-level.

The refractive index of a medium is defined to be

$$n \equiv \frac{c}{v}, \tag{4.1}$$

where c is the speed of light in a vacuum, defined through $c = 1/\sqrt{\mu_0 \epsilon_0}$ and v is the speed of light in a medium, defined through $v = 1/\sqrt{\mu\epsilon}$. For the neutral atmosphere it is safe to assume that $\mu = \mu_0$. Substituting this into the refractive index, one finds

$$\begin{aligned} v &= c\frac{\sqrt{\epsilon_0\mu_0}}{\sqrt{\epsilon\mu_0}} \\ &= c\sqrt{\frac{\epsilon_0}{\epsilon}} \\ &= c\sqrt{\frac{\epsilon_0}{\epsilon_0\epsilon_r}} \\ &= c\sqrt{0.9994} \\ &= 0.999705c, \end{aligned}$$

where ϵ_r is taken to be 1.0006. Consequently an electromagnetic signal is delayed by a distance $(1 - 0.999705) * 7852 \approx 2.31$ m when it propagates through the neutral atmosphere. This distance is called the zenith tropospheric delay (ZTD). In terms of a time delay it is 2.31 m/($3x10^8$ ms^{-1}) = 7.3 ns.

This is the basis on how GPS technology can be implemented to find the atmospheric pressure for a specific location. As the pressure varies, so will the time delay. The details are developed in Chapter 5. This chapter focuses on the GPS system in general. This section therefore shows that GPS technology is a viable option for pressure correction of neutron monitor counts.

4.3 Origin of GPS

The primary goal of GPS was to track and locate equipment, vehicles or people globally to a high degree of accuracy. At first this was done by making use of ground-based systems, e.g. DECCA, LORAN and Omega. In these systems, ground-based long-wave radio transmitters were used instead of satellites. The systems consisted of master stations and slave stations

(receivers). The time it takes the signal to reach the slave is used to determine the distance to the station. Multiple master stations could very accurately determine the coordinates of a slave station (receiver).

The first satellite-based positioning system was Transit, which was deployed by the U.S. military in the 1960s. This system made use of the Doppler shift on the signal. The Doppler shift is caused by the movement of the satellite relative to the receiver and therefore one is able to detect on which side of the satellite the receiver is situated, and hence determine the coordinates of the receiver. This system was limited by low accuracy and lack of 24-hour availability.

In 1973 the U.S. Department of Defense (DoD) directed the Joint Program Office (JPO) to develop a satellite radio navigation system. According to *Kaplan* (1996), the system was required to offer global coverage, work under any weather conditions, be highly accurate, and serve high-dynamic platforms. This system is known as the Navigation System with Timing and Ranging (NAVSTAR) Global Positioning System (GPS). The original purpose of this was the location and tracking of military units and equipment.

4.4 Global Navigation Satellite Systems (GNSS)

There are several other satellite-based navigation systems, similar to GPS, operated by various countries. The four major systems are NAVSTAR GPS, the Global Orbiting Navigation Satellite System (GLONASS), Galileo, and the Beidou (translated to English as "Compass"). These four satellite constellations were developed and are owned by the United States, Russia, the European Union and China, respectively. Galileo and Beidou are still being deployed and are not functioning at full capacity, while GLONASS is already operational although its full satellite constellation is not yet in place.

In Table 4.3.1 the four main GNSSs are shown, as well as their basic properties. Both Russia and the U.S.A. started the development and launch of the satellites in the 1970s. The more recent GNSSs were started in the early 2000s. Each GNSS consists of the most optimal number of satellites for its design purpose. These satellites are arranged in a constellation in such a way that they can be most effective. Suppose a constellation consists of 24 satellites, with six satellites in each orbit; the constellation is then made up out of four orbits. All orbits have an

inclination towards the equator; in the case of NAVSTAR GPS it is 55°, Each orbit consists of 360°, with NAVSTAR GPS having six satellites in each orbit, which means that the separation between satellites (phase angle) is given as $360°/6 = 60°$.

Table 4.3.1: The basic properties of the space segments of the four major GNSSs.

Properties	NAVSTAR GPS	GLONASS	Galileo	Beidou
Starting date	1973	mid 1970s	2002	1993
Launch of first satellite	1978	1982	2005	2000
Country	U.S.A.	Russia	Europe	China
Number of satellites	24	24	30	35
Inclination towards the equator	55°	65°	56°	55°
Phase angle	60°	120°	40°	180°

GLONASS was started by the former Soviet Union's Ministry of Defence. The original purpose of the system was to support military navigation requirements. It was broadened at a later stage to include civilian users. The receivers of the GLONASS system are generally incompatible with those of the NAVSTAR GPS system, although a number of manufacturers have recently produced multiple-constellation receivers.

The European equivalent of GPS is called Galileo. The Galileo satellite system will use the same positioning techniques as the NAVSTAR GPS. One difference between the NAVSTAR GPS and the Galileo systems is that the latter sends three signals at three distinct frequencies compared to only two from the old generation GPS satellites. This will increase the accuracy with which the ionospheric effects can be subtracted. The Galileo system will also be open to the public, but fees will be charged for more accurate positioning.

The Beidou system is in concept the same as NAVSTAR GPS, it is based on the same principles. At present the the system has only four satellites in orbit, which gives an accuracy of 20 m over China. This is far below the typical GPS accuracies; in 2000 a committee running this project found that for an accurate system 35 satellites are required. These still need to be launched.

Much research has been done to increase the accuracy that may be attained by using all the systems together. GNSS has become a widely used aid to navigation worldwide, and a useful tool

for map-making, land surveying, commerce, and other scientific uses. GNSS also provides a precise time reference used in many applications, including the scientific study of earthquakes, and synchronisation of telecommunications networks.

4.5 GPS components

Each GNSS satellite system differs in some ways from the others, and because the NAVSTAR GPS system is the most commonly used system, its details will be discussed. According to *Leick* (1990) the GPS comprises three components, the space component, the operational control component, and the user equipment component. In the following subsections these components will be discussed in detail.

4.5.1 The space component

This component refers to the space part of the system, which consists of 24 active satellites uniformly distributed around the globe. These are medium earth orbit (MEO)-satellites which orbit at an altitude of 20 200 km from the earth, and have a period of ~12 hours. The orbital planes all have an inclination of 55° relative to the equator. The satellites are separated by a phase angle of 60°.

Figure 4.1 shows each satellite's orbit around the earth for the NAVSTAR system. The satellites do not follow polar orbits, for that reduces the accuracy of the coordinates. Although there are only 24 satellites required in the main system, more satellites are still being launched into orbit to make the system more secure and increase its accuracy.

The satellites were deployed during different periods. The first group of satellites, commonly referred to as Block I, was launched from 1978 until 1985. These 11 satellites were meant to last for ~5 years, but most of them were used for about ten years. None of these satellites are still operational at present. Each Block I satellite contained one Caesium (Cs) and two Rubidium (Rb) atomic clocks.

The second group, known as the Block II, was launched from beginning 1989 until the end of 1990. There were nine of these satellites, and they were much bigger than the Block I satellites,

Figure 4.1: The orbits of NAVSTAR GPS created by the United States of America. Adapted from http://www.kowoma.de/en/gps/orbits.htm.

having a service life of eight years.

The third group, known as the Block IIA, was more advanced than Block II. These satellites were launched from the end of 1990 until the end of 1997. A total of 19 of these satellites were launched. The most important difference between them and the Block I satellites is the fact that the Block II satellites have four atomic clocks; two Caesium and two Rubidium. These clocks make it possible for the satellites to operate accurately over several days without any interference from ground control.

The fourth group of satellites, known as the Block IIR/IIR-M satellites, was launched from January 1997. The R-M is an acronym for replacement and modernised Block II satellite. These satellites have 3 Rb clocks for determining the time. They also possess the ability to detect nuclear explosions, but this is not accessible to the public.

The last group, referred to as Block IIF satellites, provides a third frequency that makes the determination of position even more accurate. These satellites were launched starting in 2005. They are equipped with hydrogen maser clocks, and provide more accurate times.

4.5.2 The operational control component

This component is required to ensure the accuracy and successful working of the satellites. The master control station is situated on the ground, and from there it sends and receives signals to determine the status of the satellites, the signal integrity, the position of the satellite, and the clock corrections. The control station is also able to redirect the path of the satellite, in such

way as to ensure that the satellite follows the designated orbit. The master control station is situated at Falcon Air Force Base, Colorado Springs, and is controlled by the U.S. Military.

Other ground stations are used to upload and download data from the satellites. These stations ensure real-time measurements and data sets. They are situated around the world, and at any time all satellites, including spare satellites, are being monitored. The more secondary ground stations available, the more satellite observations can be made at the same time, increasing the accuracy of the satellite data. Currently these secondary ground stations are located at Colorado Springs, Kwajalein, Ascension Island, Hawaii, Diego Garcia, Cape Canaveral and a few other locations.

4.5.3 The user equipment component

This component has to do with the actual device the user has available. This device can have various degrees of accuracy, depending on the type of work it is required to do. It receives the signal of four or more GPS satellites and converts these data to three coordinates and time. There are two main types of receivers, single-frequency and dual-frequency, depending on the accuracy that is required.

According to *Kaplan* (1996), a GPS receiver consists of five main components, viz. an antenna, a receiver, a processor, input/output (I/O) device and a power source. The receiver used in our case at the SANAE IV base is a Trimble 4000SSI. It was installed on 18 December 1997. The antenna is a Dorne Margolin choke-ring antenna and was installed by the Alfred Wegener Institute for Polar and Marine Research, Bremerhaven, Germany, at latitude 71°40'25.68" S and longitude 2°50'30.12" W at an altitude of 862.4 m above the WGS84 ellipsoid..

4.6 Positioning with GPS

When a satellite sends a signal towards earth, the signal contains the position of the satellite, as well as the time the signal was sent. The signal data are recorded by the receiver for positioning calculations. From the time-difference between the time the receiver received the signal and the time the signal was sent, one can determine the distance between the satellite and the

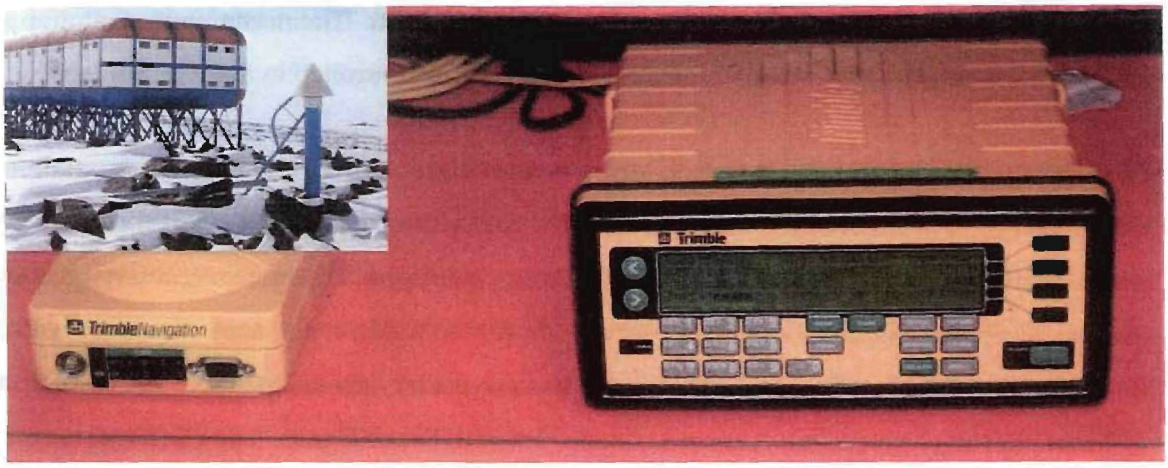

Figure 4.2: A photo of the GPS receiver at the SANAE IV base. The insert shows the antenna outside the base.

receiver. When using two satellites one can find the intersecting radius of the two satellites to be where the receiver will be. When looking at Figure 4.3 there are two positions where the receiver can be found, A and B.

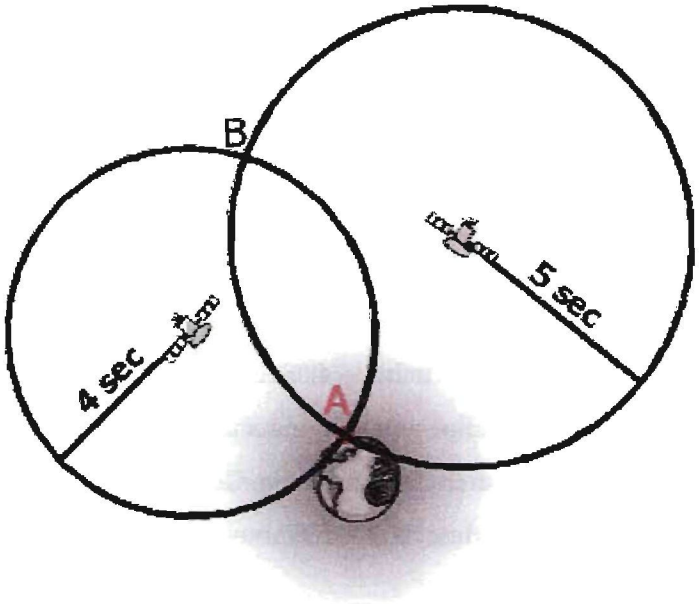

Figure 4.3: From the signal intersection, one is able to determine the position of the receiver on the earth's surface. Adapted from http://www.kowoma.de/en/gps/orbits.htm.

There are two ways to fix this problem. The first is to choose the obvious point nearest to the earth, and the other solution is by introducing a third satellite. This method of three intersecting satellite radii is called trilateration. The more satellites involved in the process the more accurately one can determine the position. A problem with the method of trilateration is that

the clock times of the satellites and the receivers may differ much. Satellites are equipped with highly accurate atomic and laser clocks which are very expensive. The timing at the receivers is much less accurate compared to the satellites. This causes inaccuracies in the distance estimates, as shown in Figure 4.4. These three satellites demarcate a volume element where the receiver should be. From this volume one can find the error on the position. The more satellites one has available, the more accurate the position.

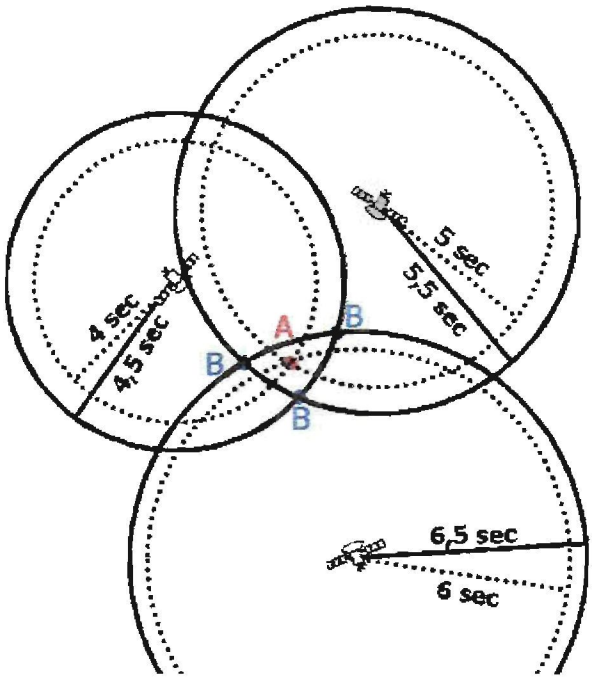

Figure 4.4: Three satellites are used to determine the volume that contains the receiver. The dotted line occurs because of the time difference between the receiver and the satellites. Adapted from http://www.kowoma.de/en/gps/orbits.htm.

In the previous paragraphs only a two-dimensional plane was considered. However, it is a requirement that GPS should be able to determine position in three dimensions. It is for this reason that three satellites are needed to determine the position of the receiver in three dimensions. This is important for our study with the GPS. A fourth satellite is necessary to determine the error due to the receiver offset.

4.7 GNSS applications

According to *Combrink* (2006), there are several uses for the GPS. Some of them are:

- Accurate navigation for the aviation and maritime communities

- Spacecraft guidance
- Military targeting and guidance
- Navigation or tracking of ground-based vehicles
- Accurate surveying, mapping, datum conversions and geographic information systems
- Geodetic applications, such as monitoring tectonic motions, crustal deformation, earth tides and continental break-up
- GPS time transfer
- Characterising of the troposphere and ionosphere

4.8 Pressure application

In this dissertation, the main focus is on yet another GNSS application, viz. to determine atmospheric pressure by making use of GPS. In Section 4.2 a basic estimation was made of the tropospheric delay of a GPS signal. If this delay is known, as well as what the atmosphere is constituted of and how the mass is distributed, then one is able to determine the atmospheric pressure. This application is not affected by wind. However, and unfortunately, this delay is severely affected by the amount of PWV in the atmosphere, the inter-frequency bias and the slant-to-vertical total electron content conversion error. The main effect in this dissertation is the PWV effect, as attention has been given to the other problems by the HartRAO Space Geodesy Programme. Therefore only the PWV problem will be discussed in detail in Chapter 5.

Chapter 5

Atmospheric effects on the GPS signal

5.1 Introduction

In the previous chapter GNSS technology and the basis on which it works were discussed. In this chapter, the NAVSTAR GPS technology is used to get the atmospheric pressure data, because of this GPS will refer to the GNSS technology as well. Furthermore, simple calculations showed that GPS technology may indeed be accurate enough to be used as a barometer for neutron monitor corrections. In this chapter a detailed discussion is given on the atmospheric characteristics that influence GPS signals. It turns out that the amount of water vapour in the atmosphere causes the largest uncertainty in the accuracy of GPS atmospheric time delay. In view of this, the first part will focus on the derivation and meaning of the Clausius-Clapeyron relation and water vapour equation in the atmosphere. Thereafter, a detailed theoretical derivation will be given of the delay suffered by electromagnetic signals in the atmosphere, both in the neutral atmosphere and in the ionosphere.

5.2 The Clausius-Clapeyron relation

The concepts PWV, relative humidity, absolute humidity, and vapour pressure are needed in this work. To sufficiently understand these theoretical ideas, the Clausius-Clapeyron relation, as well as the water vapour equation, will be derived. The Clausius-Clapeyron relation is derived from fundamental ideas in thermal physics; this will be done in the same manner as *Schroeder* (1999).

The phase boundary of a liquid or gas is the boundary where both the substances are equally stable. At this boundary, the Gibbs free energy is the same for both phases. Thus

$$G_l = G_g, \tag{5.1}$$

at the phase boundary. For a system which has a constant pressure P and temperature T, the sum of the work to create the system, and the work recovered when it is destroyed, is given by the Gibbs free energy

$$G \equiv U - TS + PV, \tag{5.2}$$

where U is the total energy, S the final entropy of the system, and V the volume.

If one assumes that the temperature and pressure changes are infinitesimal, as shown in Figure 5.1, then the change is able to proceed in such a manner as to let the two phases be equally stable. Therefore the infinitesimal changes in the Gibbs free energy are the same

$$dG_l = dG_g, \tag{5.3}$$

at the phase boundary. From the definition of Gibbs free energy

$$dG = -SdT + VdP + \mu dN, \tag{5.4}$$

where μ is the chemical potentiol, and N the number of particles. The Gibbs free energy for the liquid and gas are the same, therefor (5.3) is reformulated as

$$-S_l dT + V_l dP = -S_g dT + V_g dP, \tag{5.5}$$

where dN is equal to zero, because the number of particles in each phase is equal, and therefore cannot change.

From (5.5) it follows that, the slope of the phase boundary in Figure 5.1 is given by

$$\frac{dP}{dT} = \frac{S_g - S_l}{V_g - V_l} \equiv \frac{\Delta S}{\Delta V}. \tag{5.6}$$

Noting that $\Delta S \equiv L/T$, (5.6) becomes

$$\frac{dP}{dT} = \frac{L}{T\Delta V}, \tag{5.7}$$

where the latent heat (L) is the heat (Q) per unit mass (m), given by

$$L \equiv \frac{Q}{m}. \tag{5.8}$$

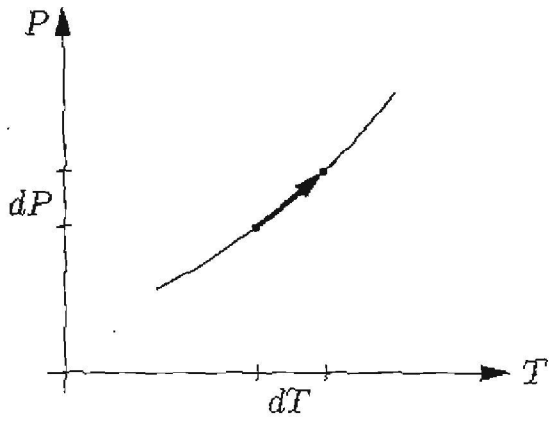

Figure 5.1: Infinitesimal changes in both pressure and temperature in such a way that the phase boundary remains constant. Adapted from *Schroeder* (1999).

Equation (5.7) is known as the Clausius-Clapeyron relation, and applies to any phase boundary. From the Clausius-Clapeyron relation one is able to derive the water vapour pressure equation. This equation is important as it describes the process of water vapour equilibrium in the atmosphere. Firstly, assume that over a small line element of the phase boundary the latent heat is constant. Secondly, assume that one ofth phases is a gas, and therefore ΔV can be taken to be the volume V. The ideal gas law states

$$PV = nRT, \tag{5.9}$$

where n is the number of moles, and R is the universal gas constant. When substituting this into the Clausius-Clapeyron relation, it follows that

$$\frac{dP}{dT} = \frac{LP}{nRT^2}. \tag{5.10}$$

By substituting $L = nl$, where l is the specific latent heat, into (5.10) and rewriting it, one finds

$$\frac{dP}{P} = \frac{l}{R}\frac{dT}{T^2}. \tag{5.11}$$

Integrating over both sides

$$lnP = -\frac{l}{R}\frac{1}{T} + c_1, \tag{5.12}$$

and rewriting it in exponential form

$$P = c_1 e^{\frac{-l}{RT}}, \tag{5.13}$$

where c_1 is a constant. By assuming that at T_0, the pressure is P_0, the constant c_1 has a value

$$c_1 = P_0 e^{\frac{l}{R}(\frac{1}{T_0})}. \tag{5.14}$$

Substituting (5.14) into (5.13), the formula for determining the pressure is found to be

$$P = P_0 e^{\frac{l}{R}(\frac{1}{T_0} - \frac{1}{T})}. \tag{5.15}$$

This is called the vapour pressure equation. Using data from *Keenan et al.* (1978) and *Lide* (1994), the value of P_0 at temperature $T_0 = 273.14$ K, is determined to be 612 Pa (i.e. $\sim 6.12x10^{-3}$ atmospheres). Furthermore, the universal gas constant R has a value of 8.31 J/(mol K), and the value of the latent heat (l) is equal to $\sim$ 40930 J/mol. When substituting this into (5.15), one finds that

$$\begin{aligned} P &= 612e^{\frac{40930}{8.31}(\frac{1}{273.14} - \frac{1}{T})} \text{ Pa}, \\ &= 612e^{4925.39(\frac{1}{273.14} - \frac{1}{T})} \text{ Pa}, \end{aligned}$$

$$P = 612e^{18.03(1-273.14/T)} \text{ Pa}, \tag{5.16}$$

if the temperature is expressed in degrees Celcius, this expression becomes

$$P = 612e^{\frac{18.03T}{273.14+T}} \text{ Pa}. \tag{5.17}$$

This water vapour pressure is derived from simple, basic principles. Its physical meaning is the additional pressure caused by PWV in the atmosphere. This expression differs somewhat from the widely used Kuemmel water vapour (KWV) expression used by *Kuemmel* (1997)

$$P = 610.78e^{\frac{17.2694T}{238.3+T}} \text{ Pa}, \tag{5.18}$$

(where the temperature is again measured in degrees Celcius). The difference between them is illustrated in Figure 5.2.

The reason why (5.17) and (5.18) do not agree at higher and lower temperatures, is because the latent heat is not constant over temperature as is assumed in (5.17). The derivation shows the origin of the equation, but henceforth the Kuemmel water vapour (KWV) equation will be used.

5.3 Clausius-Clapeyron relation in practice

In the previous section the Clausius-Clapeyron relation was derived from fundamental physics. The fundamental equation was compared to the KWV equation (5.18), where it was found that

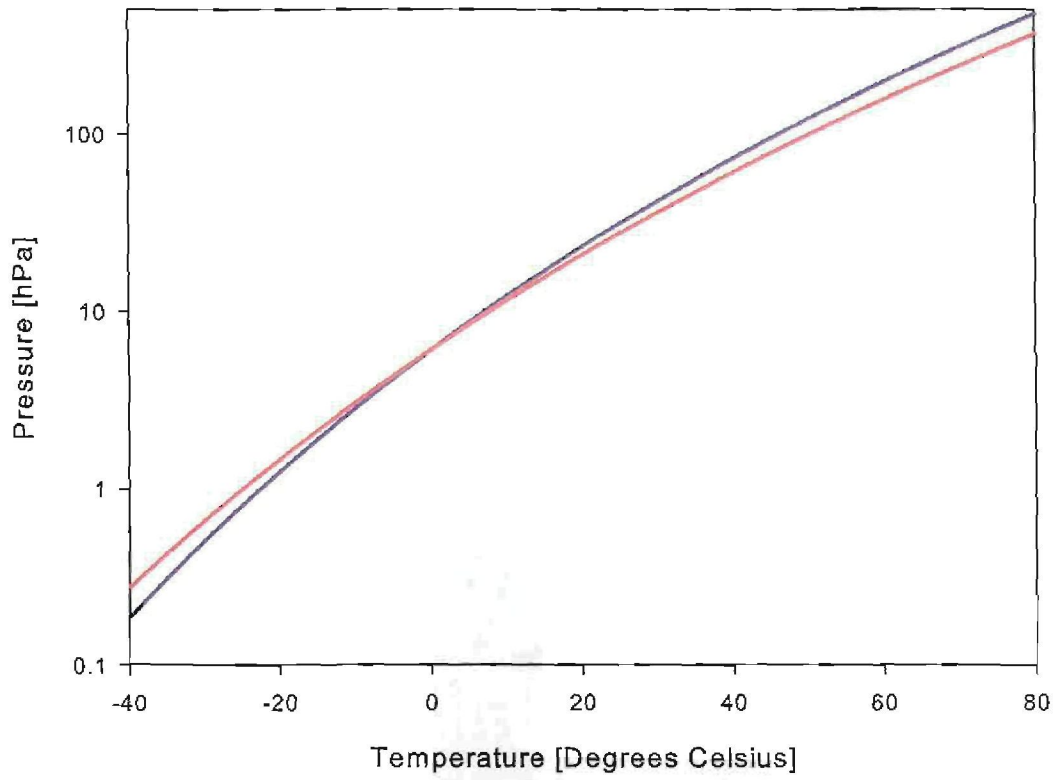

Figure 5.2: The blue line is the Kuemmel water vapour equation (5.18), and the red line the fundamentally derived water vapour equation (5.17). The pressure has a logarithmic scale to show the difference between these two expressions.

they are in essence the same equation. In this section the theory is going to be used to explain the data. There are two concepts used to describe water vapour pressure; the first is the so called PWV, and the second concept is KWV.

The PWV data is found by using bilinear interpolation methods on the National Centers for Environmental Prediction (NCEP) data sets. According to *Kalnay et al.* (1996) the main focus of these weather groups is to predict the weather data at certain points on the surface of the earth. These predictions are made using real time data collected by various weather stations around the globe. The data have been appropriately interpolated by the HartRAO Space Geodesy Programme to obtain PWV values for the SANAE IV base. In Figure 5.3 the PWV values are plotted against atmospheric temperature in a density plot. The atmospheric temperature data are by courtesy of SAWS. In this figure the black line indicates the value for KWV at those specific temperatures. The KWV line is that line which predicts the maximum amount of pressure the water will contribute to the atmospheric pressure. The fact that the PWV data

points lie above the KWV line, tells one that the PWV data are inconsistent. This is because the grid points are only predictions, and furthermore they were interpolated to the SANE IV base.

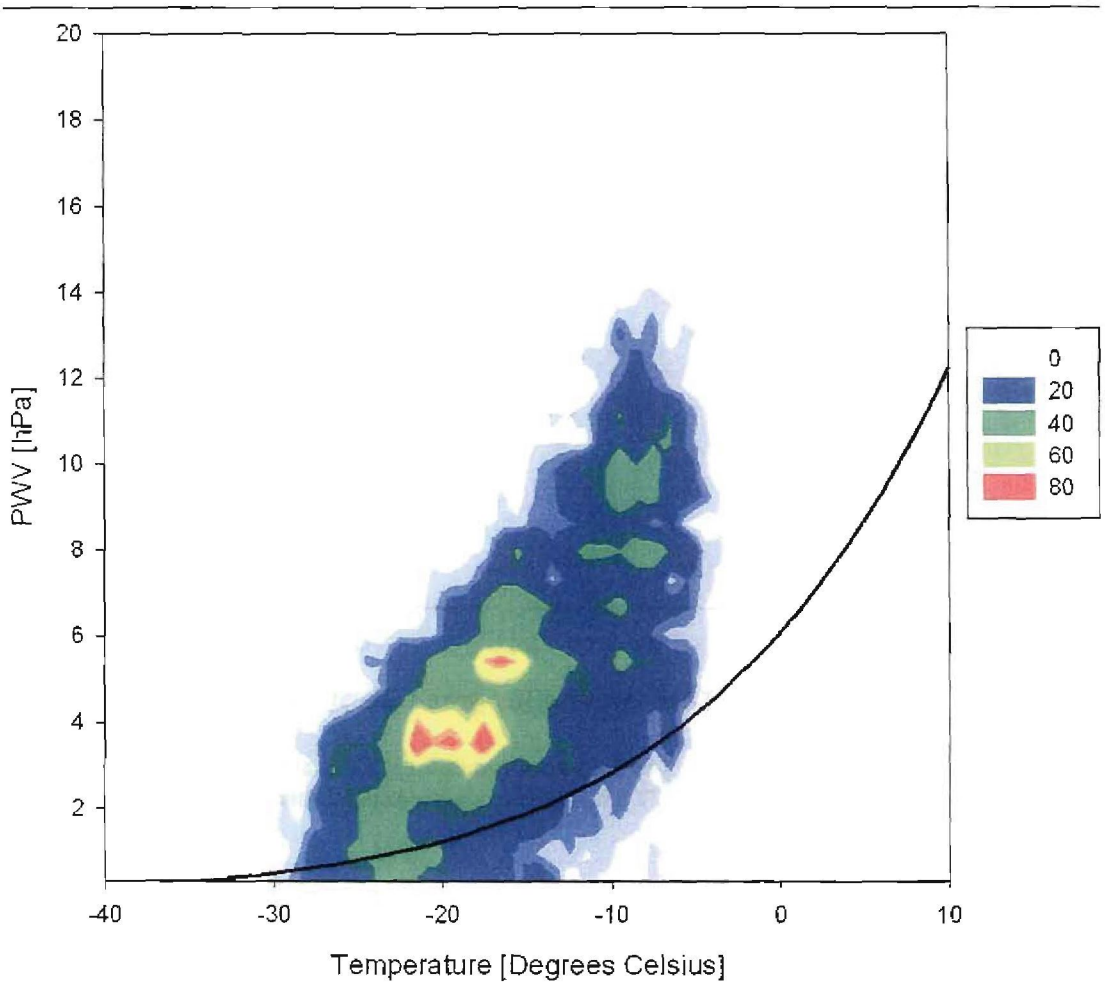

Figure 5.3: The density graph of atmospheric temperature and PWV. This is for the SANAE IV station in Antarctica, for data from start 1998 till end 2006. On the side of the graph the density of data points is indicated.

In Figure 5.4 the relation between KWV and atmospheric temperature is shown. In this figure three stations are plotted, the black data points are for the SANAE IV base, the red data points for Sutherland, and the blue data points for Nelspuit. The pink plot is for the KWV relation for those specific atmospheric temperatures. As can be seen all the data points are equal or less than the KWV line. This is because the data points are calculated by multiplying the KWV values with RH/100, where RH is in percentages. Therefore all the points can only be equal or less than KWV. It is apparent that there is a significant difference between the measured PWV and KWV values. This significant difference will be discussed in depth in Chapter 6.

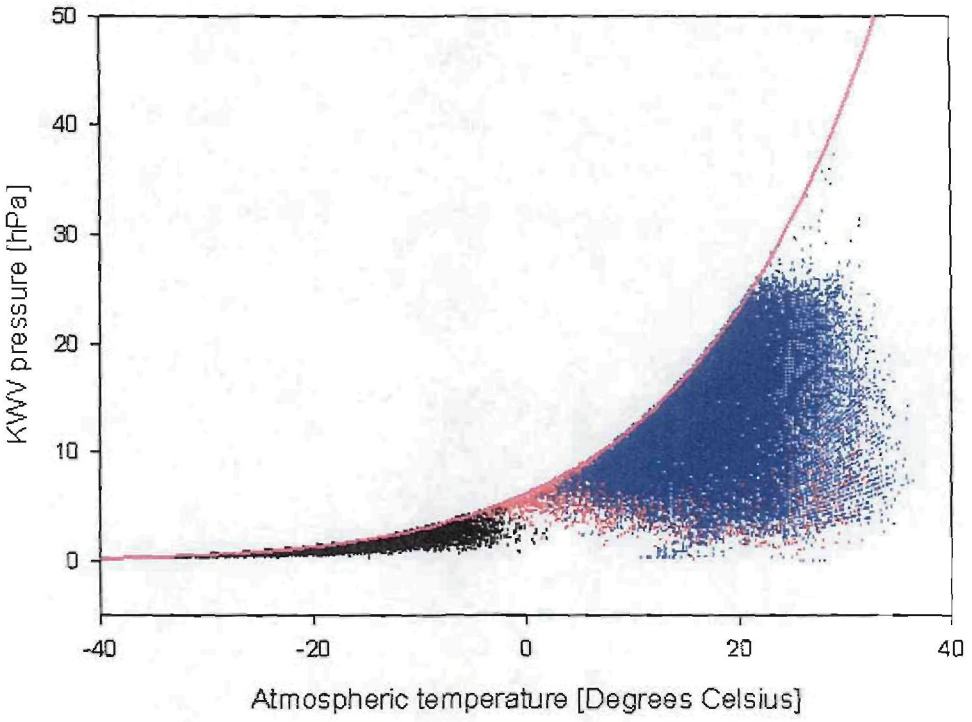

Figure 5.4: The KWV values for the three stations SANAE IV, Nelspruit, and Sutherland. The pink plot is the KWV value. The data is from beginning 1998 till end 2006.

Relative humidity is defined by $RH = \frac{P_{H_2O}}{P^*_{H_2O}} \text{x} 100\%$ where P_{H_2O} is the partial pressure of water vapour and $P^*_{H_2O}$ the saturated water vapour pressure. The term saturated indicates that the atmosphere has all the water in it that is possible.

5.4 The propagation of electromagnetic waves in matter

Having established the significant, and highly variable, partial pressure of PWV in the atmosphere, this section now describes in detail how electromagnetic waves are dispersed in the atmosphere. These basic principles are usually ignored in studies of this kind, and the results are merely accepted. The index of refraction for a medium is defined as $n = c/v$, where v is the phase speed of the wave in a medium and c the speed of an electromagnetic wave in a vacuum. It is a well-known fact that the index of refraction depends on the frequency of the electromagnetic wave in a dispersive media; a phenomenon known as dispersion. In this section the index of refraction of the neutral and ionized atmosphere, and its effect on electromagnetic waves will be discussed.

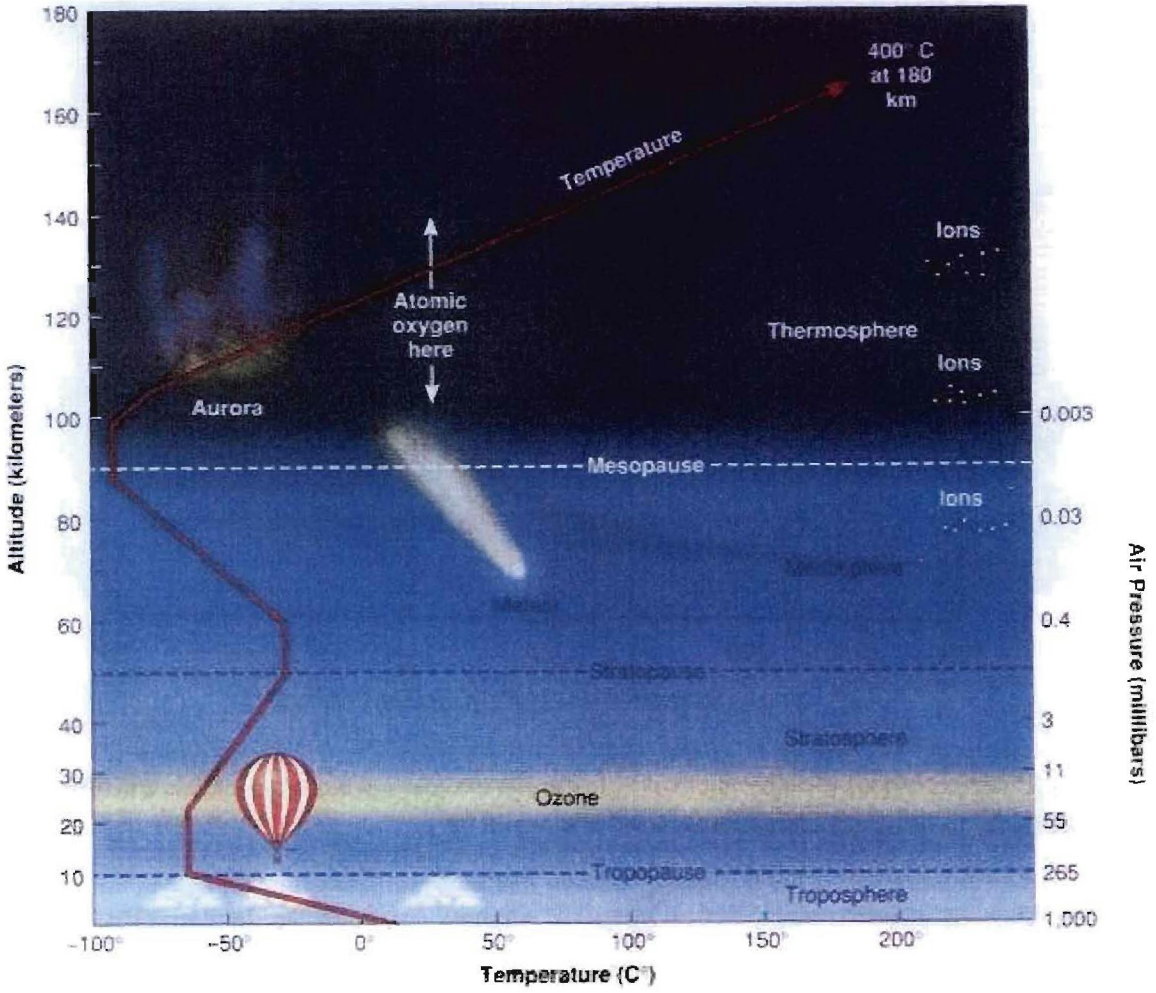

Figure 5.5: Profile of the earth's atmosphere with its different layers. Adapted from http://faculty.millikin.edu/ erobertson.nsm.faculty.mu/GlobalStudiesClimate2003/Atmprofile.html.

According to *Combrink* (2003) the atmosphere is constituted of five parts; the troposphere, ozonosphere, stratosphere, mesosphere and thermosphere. These layers can be characterised into two main groups, that of the charged part and the neutral part. The neutral part includes the troposphere, ozonosphere, stratosphere, and lower mesosphere. It extends over altitudes of 0-70 km. The charged part, called the ionosphere, consists of the layers above 70 km. It includes the upper mesosphere and thermosphere. The index of refraction differs for each of these two layers, because it is affected by different properties in the two main groups. The way these properties affect the index of refraction will be discussed in the following two subsections.

5.4.1 The tropospheric delay

In *Griffiths* (1999), a model for dispersion on an atomic scale is developed. For a neutral gas, nuclei with electrons attached to them by imaginary spring are used as the model. Figure 5.6 shows the simplistic way the model is constructed. On the left hand side of the figure an incoming electromagnetic wave with velocity v is shown.

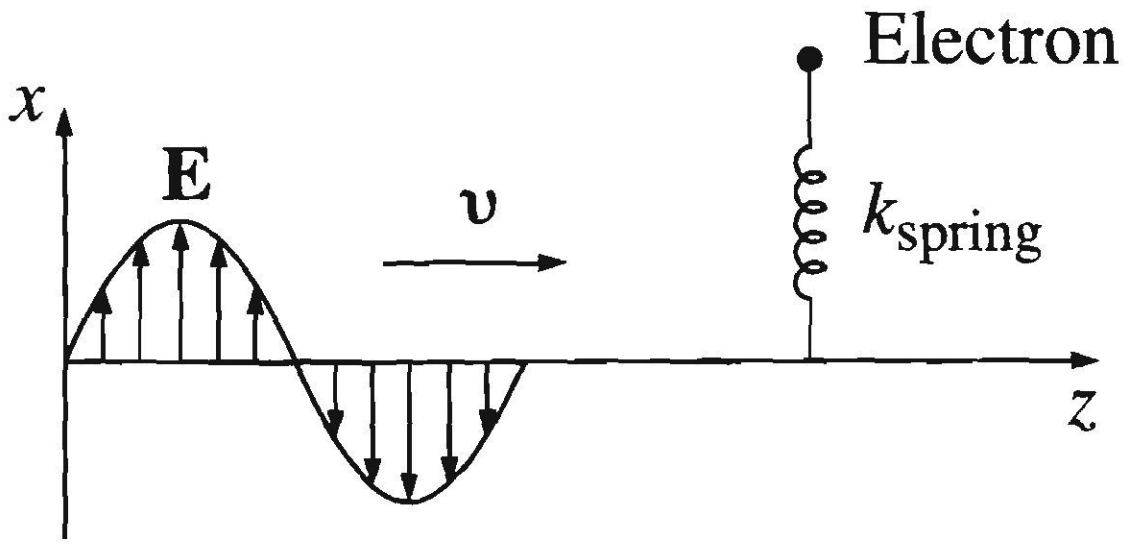

Figure 5.6: The simplistic model that is used to explain dispersion on atomic scale. Adapted from *Griffiths* (1999).

There are three forces working in on the electron:

- The centrifugal force on the electron as it orbits the atom's nucleus. This force can be expressed as

$$F_{\text{binding}} = -k_{\text{spring}} = -m\omega_0^2 x, \tag{5.19}$$

where $-k_{\text{spring}}$ is a constant, m is the mass of the electron, x the displacement and ω_0 the natural oscillation frequency. This natural oscillation frequency included in the centrifugal force is given by

$$\omega_0 = \sqrt{k_{\text{spring}}/m}, \tag{5.20}$$

where ω_0 is the frequency at which a free system vibrates.

- Suppose the incoming electromagnetic wave is polarized in the x-direction, then the driv-

ing force acting on the electron is given by

$$F_{\text{driving}} = qE = qE_0 cos(\omega t), \tag{5.21}$$

where ω is the frequency of the wave, q the charge of the electron, and E_0 the amplitude of the wave.

- The last force called the damping force is given by

$$\omega_0 = -m dx/dt, \tag{5.22}$$

with the damping coefficient and the negative sign indicating that it works against the movement of the electron. The damping is due to the fact that the oscillating charges take away energy from the electromagnetic waves.

From Newton's second law it follows that

$$m\frac{d^2x}{dt^2} + m\gamma\frac{dx}{dt} + m\omega_0^2 x = qE_0 \cos(\omega t). \tag{5.23}$$

Therefore this model expresses the electron as a damped harmonic oscillator being driven at frequency ω. With these forces taken into consideration, the dipole moment is the real part of

$$\tilde{p}(t) = q\tilde{x}(t) = \frac{q^2/m}{\omega_0^2 - \omega^2 - i\gamma\omega} E_0 e^{-i\omega t}, \tag{5.24}$$

where $\tilde{x}(t)$ is the system oscillation with driving frequency ω. It is given as

$$\tilde{x}(t) = \tilde{x}_0 e^{i\omega t}. \tag{5.25}$$

Each molecule has different electrons, each with its own orientation, and therefore different damping coefficients and natural frequencies. Assume that there are f_j electrons with frequency ω_j and damping coefficients γ_j in each molecule, then for N molecules the polarization (dipole moment per unit volume) will be given by the real part of

$$\tilde{\mathbf{P}} = \frac{Nq^2}{m}\left(\sum_j \frac{f_j}{\omega_0^2 - \omega^2 - i\gamma_j\omega}\right)\tilde{\mathbf{E}}. \tag{5.26}$$

From noting that there is a phase difference between $\tilde{\mathbf{P}}$ and $\tilde{\mathbf{E}}$ and that the polarization by definition is given by

$$\tilde{\mathbf{P}} = \varepsilon_0 \tilde{\chi}_e \tilde{\mathbf{E}}, \tag{5.27}$$

then the electromagnetic wave

$$\tilde{\mathbf{E}}(z,t) = \tilde{\mathbf{E}}_0 e^{(-\kappa z)e^{i(kz-\omega t)}}. \tag{5.28}$$

By definition the complex wave number is defined to be

$$\tilde{k} = \frac{\omega}{c}\sqrt{\tilde{\epsilon}_r}. \tag{5.29}$$

Therefore the complex wave number is given by

$$\tilde{k} = \frac{\omega}{c}\sqrt{1 + \frac{Nq^2}{m\epsilon_0}\sum_j \frac{f_j}{\omega_0^2 - \omega^2 - i\gamma\omega}}, \tag{5.30}$$

where

$$\tilde{\epsilon}_r = 1 + \frac{Nq^2}{m\epsilon_0}\sum_j \frac{f_j}{\omega_0^2 - \omega^2 - i\gamma\omega}. \tag{5.31}$$

By definition the natural frequency is defined to be

$$\omega_0^2 \equiv \frac{Nq^2}{m\epsilon_0}, \tag{5.32}$$

by substituting (5.32) into (5.30), taking $j = 1$, and then rationalising $\tilde{k}$, one finds

$$\tilde{k}^2 = \frac{\omega^2}{c^2}[1 + \omega_0^2\frac{(\omega_0^2 - \omega^2)}{(\omega_0^2 - \omega^2)^2 + \gamma^2\omega^2} + i\omega_0^2\frac{\gamma\omega}{(\omega_0^2 - \omega^2)^2 + \gamma^2\omega^2}]. \tag{5.33}$$

This implies that $\tilde{k}$ itself is given by $\tilde{k} = +i\kappa$. This implies that $\tilde{k}^2 = k^2 - \kappa^2 + ik\kappa$, so that

$$u = k^2 - \kappa^2, \tag{5.34}$$

$$v = 2k\kappa, \tag{5.35}$$

one finds the solutions of k and κ

$$k = \sqrt{\frac{u}{2}\sqrt{1 + \frac{v^2}{u^2}} + 1}, \tag{5.36}$$

$$\kappa = \sqrt{\frac{u}{2}\sqrt{1 + \frac{v^2}{u^2}} - 1}. \tag{5.37}$$

The signs of both the square roots are positive, otherwise $k^2 < 0$, and $\kappa^2 < 0$, and hence k and κ are imaginary.

The power of the electromagnetic wave is proportional to E^2, and therefore also to $e^{-2\kappa z}$. For this reason the quantity

$$\alpha = 2\kappa, \tag{5.38}$$

is called the absorption coefficient. The phase velocity is given by ω/k and the index of refraction by $n = ck/\omega$. Therefore

$$n = \frac{ck}{\omega} = \sqrt{\frac{u}{2}\sqrt{1+\frac{v^2}{u^2}}+1}, \tag{5.39}$$

and

$$\alpha = 2\kappa = 2u\sqrt{2u\sqrt{1+\frac{v^2}{u^2}}-1}, \tag{5.40}$$

where it follows from (5.34) and (5.35) out of (5.34) that

$$u = 1+\omega_0^2\frac{\omega_0^2-\omega^2}{(\omega_0^2-\omega^2)^2+\gamma^2\omega^2}, \tag{5.41}$$

and

$$v = \omega_0^2\frac{\gamma\omega}{(\omega_0^2-\omega^2)^2+\gamma^2\omega^2}. \tag{5.42}$$

Expression (5.33) can be approximated to find the complex wave number to be

$$\tilde{k} \approx \frac{\omega}{c}[1+\omega_0^2\frac{(\omega_0^2-\omega^2)}{(\omega_0^2-\omega^2)^2+\gamma^2\omega^2}+i\omega_0^2\frac{\gamma\omega}{(\omega_0^2-\omega^2)^2+\gamma^2\omega^2}]. \tag{5.43}$$

Using this approximation one finds the expression of n as

$$n = \frac{ck}{\omega} = 1+\frac{1}{2}\frac{\omega_0^2(\omega_0^2-\omega^2)}{(\omega_0^2-\omega^2)^2+\gamma^2\omega^2}. \tag{5.44}$$

For radio and optical frequencies the damping term is small, and thus n in (5.44) reduces to

$$n = 1+\frac{\omega_p^2}{2(\omega_0^2-\omega^2)}. \tag{5.45}$$

The transport of optical waves is dispersive in the troposphere. The propagation of radio waves is non-dispersive in the troposphere. This is due to the fact that its frequency falls in a highly dispersive band as is shown in Figure 5.7.

Figure 5.7 shows the absorption coefficient (α) for three values of the damping coefficient (γ). The blue plot is for γ 10 times that of the natural frequency (ω_0), for the gray plot γ equal to ω_0, and for the black plot γ is 0.1 times that of ω_0. For the black plot a part of the numerical solution is undefined when $\gamma < \sqrt{2}-1\omega_0$. This causes the $\sqrt{2u}$ part of (5.40) to become imaginary and therefore does not show on the figure. For the blue and gray plots this does not happen as γ is large enough.

There is an interesting limit for α. It occurs at $\omega/\omega_0 = \varepsilon$, where $\varepsilon \ll 1$. This tells us that at frequencies where $\omega \ll \omega_0$ there is a linear relation. This relation is found by substituting ε into (5.40), the relation is $\alpha \approx \varepsilon = \omega/\omega_0$.

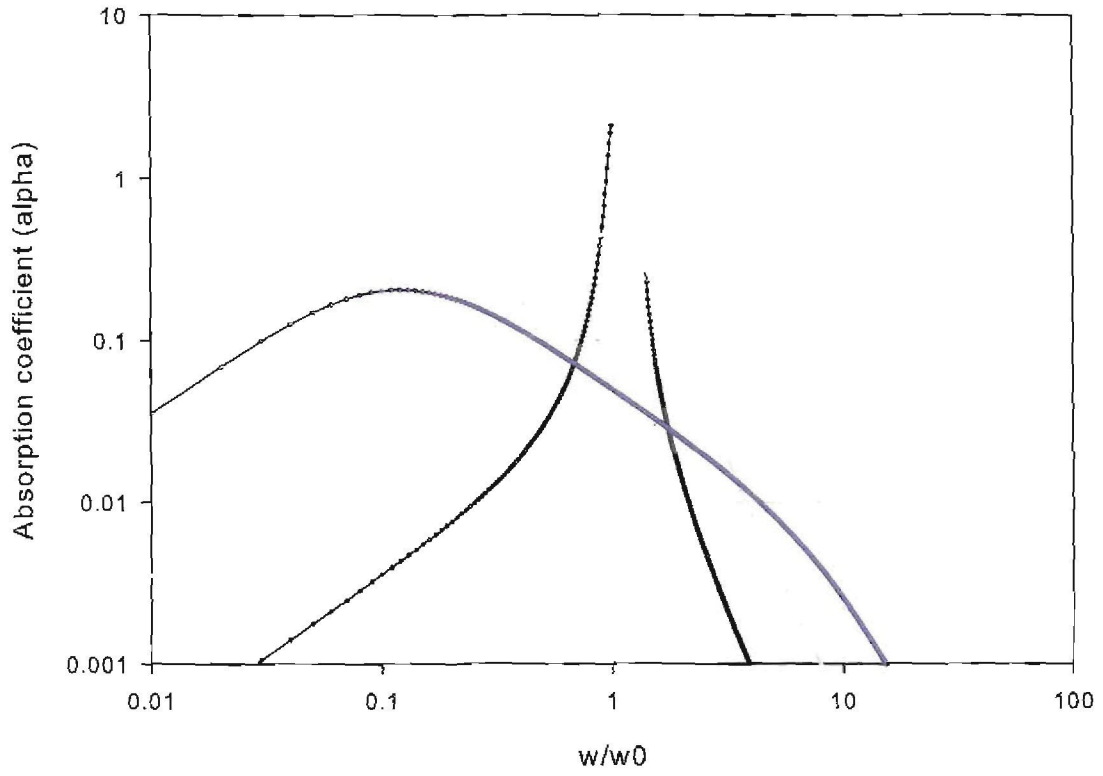

Figure 5.7: General expressions for the absorption coefficient. The blue plot is for $\gamma = 10\omega_0$, for the gray plot $\gamma = \omega_0$, and for the black plot $\gamma = 0.1\omega_0$.

For the index of refraction, Figure 5.8, the limit for $\omega/\omega_0 \ll 1$ is given as $\sqrt{2} - 1$. This limit can be found from (5.39), by substituting $\omega/\omega_0 \ll 1$ into the expression. This figure is sketched on a logarithmic scale on both axis, and therefore only the values of positive $n - 1$ is seen. The negative $n - 1$ values are not seen and are exactly the replica of the positive values except that its limit is at $\omega/\omega_0 \gg 1$. This limit has a value of $-\sqrt{2} + 1$.

After having established the general dispersion expressions, it remains to calculate the natural frequency ω_0. There are three ways to calculate this for the troposphere. In the first method the natural frequency is calculated by making use of its definition in (5.32)

$$f_0^2 = \frac{\omega_0^2}{4\pi^2} = \frac{Nq^2}{4\pi^2 m_e \epsilon_0}, \tag{5.46}$$

where q is the charge of an electron, m_e its mass, and ϵ_0 the permittivity of free space. The electron density (N) is determined by

$$N = \frac{\rho_{\text{air}}}{m_{\text{air}}} N_A, \tag{5.47}$$

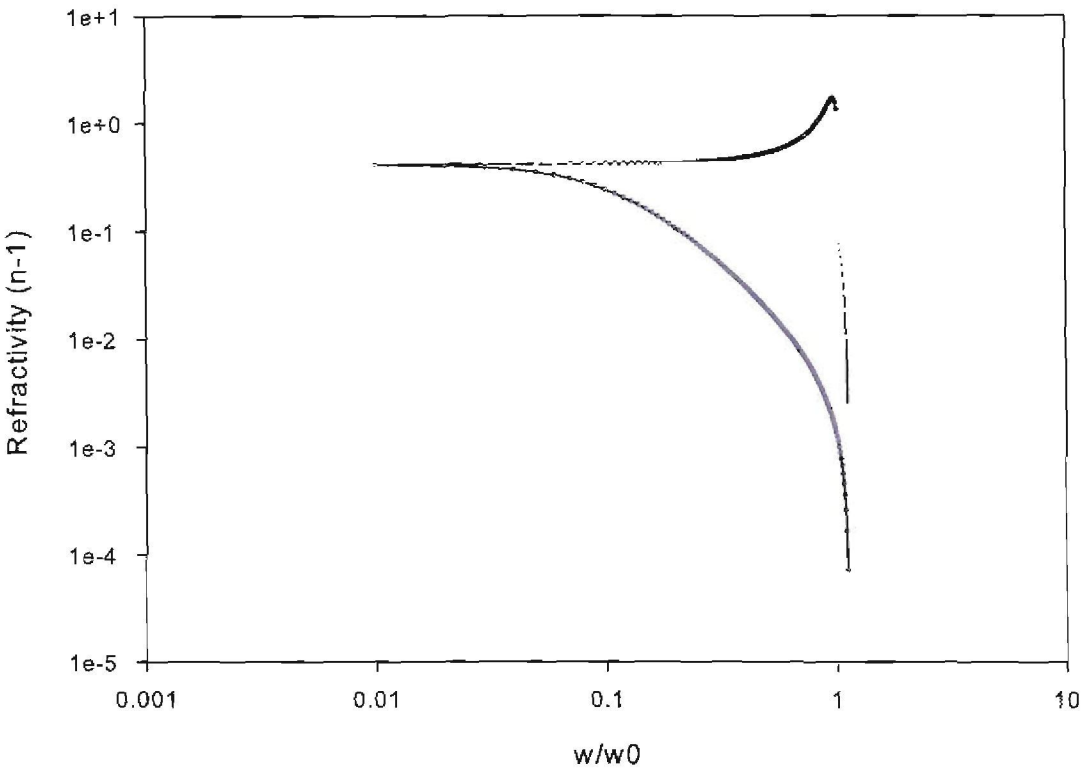

Figure 5.8: General expressions for the index of refraction. The blue plot is for $\gamma = 10\omega_0$, for the gray plot $\gamma = \omega_0$, and for the black plot $\gamma = 0.1\omega_0$.

where ρ_{air} is the average density of air at ambient temperature and pressure, m_{air} the molar mass of air, and N_A Avogadro's number. The value of N is

$$\begin{aligned} N &= \frac{1.169\ \text{kg m}^{-3}}{28\text{x}10^{-3}\ \text{kg mol}^{-1}} 6.022\text{x}10^{23}\ \text{mol}^{-1} \\ &= 2.57\text{x}10^{25}\ \text{m}^{-3}. \end{aligned}$$

This expression needs to be multiplied by the number of electrons in the outer most shell of the molecule. In this case the diatomic nitrogen molecule has 10 electrons in the outer shells. This gives the value of N_A to be $2.57\text{x}10^{26}\ \text{m}^{-3}$. Substituting this value into (5.46) one finds the value of the resonance frequency to be

$$f_0 = 1.44\text{x}10^{14}\ \text{Hz}. \tag{5.48}$$

By making use of the model in *Griffiths* (1999) (example 4.1), that is (5.19), one is able to find

the angular natural frequency

$$\omega_0^2 = \frac{k}{m_e} = \frac{F}{m_e x} = \frac{qE}{m_e x} = \frac{q^2}{4\pi\epsilon_0 a^3 m_e} = \frac{q^2}{4\pi\epsilon_0 a^3 m_e}, \tag{5.49}$$

where the electric field E of a point charge is

$$E = \frac{qx}{4\pi\epsilon_0 a^3}. \tag{5.50}$$

The natural frequency is therefore given by

$$f_o = \sqrt{\frac{q^2}{16\pi^3\epsilon_0 a^3 m_e}}. \tag{5.51}$$

The value of a for the outer electron shell of the nitrogen molecule is in the same order as the Bohr radius. The distance a from the nucleus is therefore taken to be the Bohr radius that is $a = 5.29\text{x}10^{-9}$. The value for the natural frequency is

$$f_0 = 7.15\text{x}10^{15} \text{ Hz}. \tag{5.52}$$

The last method is derived from the well known Bohr hydrogen model. The speed of the Bohr hydrogen electron is determined by

$$v_e = \frac{h}{2\pi m_e a}, \tag{5.53}$$

where h is the Planck constant, m_e the electron mass, and a the Bohr radius. The speed of the electron v_e has a value of $2.2\text{x}10^6$ ms^{-1}. Assuming the orbit of the electron is circular, the natural frequency of the electron is easily found to have a value of

$$f_0 = \frac{v_e}{2\pi} = 6.6\text{x}10^{13} \text{ Hz} = 66 \text{ THz}. \tag{5.54}$$

These three crude models give natural oscillation frequencies of $1.44\text{x}10^{14}$ Hz, $7.15\text{x}10^{15}$ Hz and $6.6\text{x}10^{13}$ Hz, with an average of $2.45\text{x}10^{15}$ Hz. This is $1\text{x}10^6$ times larger than the transmission frequencies of $f_1 = 1.57542$ GHz and $f_2 = 1.22760$ GHz of GPS. Thus, the limit $\omega/\omega_0 \ll 1$ is certainly valid in the troposphere, therefore (5.45) is valid, and the propagation of the GPS signal through the troposphere is dispersionless.

5.4.2 The ionospheric delay

The ionosphere is formed when atoms in the upper atmosphere are ionized. This happens when atoms absorb UV-radiation energy from the sun, and the electrons of these atoms gain

enough kinetic energy to be displaced from their orbits. This process forms free electrons and ions, and these are then called the ionosphere. These particles also recombine continuously so that only a fraction of the ionosphere is charged at a specific time. The ionosphere can be divided into three main layers given in Table 5.3.1.

Table 5.3.1: Properties of the ionospheric layers. Adapted from Medeiros (2000)

Layer	Altitude (km)	Maximum reflected frequency (MHz)	Chemical component
D	65-80	16	Ozone
E	80-115	28	Oxygen
F_1	140-250	16	Nitrogen
F_2	250-400	16	Oxygen

This ionospheric medium is a plasma. The electrons (as well as the ions, but at much lower frequencies) gyrate about the geomagnetic field line in this plasma. This causes an oscillation frequency for the electrons that is several orders of magnitude lower than the optical frequencies just derived for the troposphere. In fact, it will now be shown through the standard technique of dispersion equations in Plasma Physics, that this so-called plasma frequency of the ionosphere is in the same order of magnitude as the transmission frequencies of the GPS. Hence, the ionospheric propagation is highly dispersive.

According to *Choudhuri* (1998) the index of refraction is found by using Maxwell's equations

$$\nabla \times \mathbf{E} = -\frac{\partial \mathbf{B}}{t}, \tag{5.55}$$

and

$$\nabla \times \mathbf{B} = \mu_0 \mathbf{J} + \mu_0 \varepsilon_0 \frac{\partial \mathbf{E}}{\partial t}, \tag{5.56}$$

where $\mathbf{E}$ and $\mathbf{B}$ are the electric and magnetic components of the electromagnetic waves, and $\mathbf{J}$ is the current density. From the $e^{i(k\cdot r-\omega t)}$ dependence of electromagnetic waves and their transverse nature, one is able to write

$$(\omega^2 - c^2k^2)\mathbf{E} = \frac{-i\omega}{\varepsilon_0}\mathbf{J}. \tag{5.57}$$

The inertial mass of ions, much larger than that of electrons suggests that the motion of elec-

trons will be the only source of current

$$\mathbf{J} = -n_0 q \mathbf{v}, \tag{5.58}$$

with q the charge of an electron, n_0 the number density of electrons and $\mathbf{v}$ their velocity.

From Newton's second law

$$m\frac{d\mathbf{v}}{dt} = -e\mathbf{E}, \tag{5.59}$$

and the assumption that the waves have an $e^{i(k.r-\omega t)}$ dependency, it follows

$$(\omega^2 - c^2k^2)\mathbf{E} = \frac{n_0 q^2}{\varepsilon_0 m_e}\mathbf{E}, \tag{5.60}$$

where $\mathbf{v} = \frac{e\mathbf{E}}{im\omega}$.

By definition the plasma frequency is given as

$$\omega_p^2 \equiv \frac{n_0 e^2}{\epsilon_0 m}. \tag{5.61}$$

Substituting this definition into (5.60) one finds the dispersion relation

$$\omega^2 = \omega_p^2 + c^2\kappa^2, \tag{5.62}$$

where ω_0 is the plasma frequency, c the speed of light in a vacuum, and κ the wave number. The dispersion relation can be substituted into the definition of the refraction index $n = c\kappa/\omega$

$$\begin{aligned} n &= \frac{c\kappa}{\sqrt{\omega_0^2 + c^2\kappa^2}} \\ &= \frac{1}{\sqrt{1 + \frac{\omega_0^2}{c^2\kappa^2}}} \\ &\approx \frac{1}{1 + \frac{\omega_0^2}{2c^2\kappa^2}} \\ &\approx 1 - \frac{\omega_0^2}{2c^2\kappa^2}. \end{aligned}$$

using (5.62) to get rid of the $c^2\kappa^2$ term, n is

$$n = 1 - \frac{\omega_p^2}{2(\omega^2 - \omega_0^2)}. \tag{5.63}$$

This is the same expression as was found for the troposphere given by (5.45). In essence both the absorption coefficient and refraction index of the ionosphere and troposphere are the same, except for the plasma/natural frequency ω_p/ω_0. The natural frequency of the troposphere is

taken to be the frequency at which the electrons rotate around the nucleus. In the case of the ionosphere, ω_p is proportional to the square root of the number density of electrons in the ionosphere, which can be integrated to yield the total electron content (TEC) of the ionosphere.

The TEC is defined as the number of electrons in a column of unit area cross section along the trans ionospheric ray path, written as

$$E_T = \int_0^{h_0} N dh, \tag{5.64}$$

where N is the spatial density of electrons, h is the coordinates of propagation of the wave, and h_0 corresponds to the effective top of the ionosphere. TEC is highly variable and depends on numerous factors, such as local time, latitude, season and solar activity.

For the radio frequencies of GPS signals, one finds to first order that the refractivity is

$$N_e \cong \mp \frac{1}{2}\frac{\omega_p^2}{\omega^2} = \mp \frac{40.3 H z^2 m^3}{f^2} n_0. \tag{5.65}$$

When m is negative then it refers to the phase velocity, and when it is positive it refers to the group velocity. The value of n_0 for the ionosphere is in the order of $10^{12} m^{-3}$, so we find for the 1.6 GHz GPS signal that a typical value for the refractivity of the ionosphere would be $N_e \approx 1.6 \times 10^{-5}$. The experienced distance error due to the ionosphere, is defined as

$$\Delta L_e \equiv \int_0^{\infty} N_e(z) dz, \tag{5.66}$$

where z is the coordinate of propagation. Thus the vertical path correction for the ionosphere is given by:

$$\Delta L_e = \mp \frac{40.3 H z^2 m^3}{f^2} \int_0^{\infty} n_0(z) dz = \mp \frac{40.3 H z^2 m^3}{f^2} E_T, \tag{5.67}$$

where E_T is the TEC. For a typical value of TEC the 1.6 GHz GPS signal will have an ionospheric distant error of $\mp$8m.

Thus from (5.67) it is clear that the path correction is dependent on the TEC, and inversely proportional to the square of the frequency of the incoming electromagnetic wave. From this one can tell that the transport of radio waves in the ionosphere is dispersive.

Chapter 6

Data Analysis

6.1 Problem statement

Neutron monitors need to be corrected for atmospheric pressure, due to the cosmic-ray cascade effect in the atmosphere. In Chapter 3 the effect of wind on the pressure readings of the paroscientific barometer was made clear. In *Malan and Moraal* (2002) it is suggested that GPS technology should be used to determine this pressure, and in Chapter 4 it was shown how one might be able to do this. GPS technology can predict the atmospheric pressure without the wind affecting it. One of the problems with the GPS-method is that it is affected by water vapour in the atmosphere. The other problems relate to interfrequency bias, phase jitter and slant-to-vertical mapping error.

The main idea of the data analysis method is to find a method by which both the water vapour and wind effects can be eliminated by combining the two data sets and finding a corrected data set. In *Malan and Moraal* (2002) the Bernoulli effect was found only to describe 38% of the effect of wind on the pressure data. KWV values are very low at SANAE IV base, and therefore it should be a suitable spot for the data analysis.

In this chapter the reasons for using the specific location and instrumentation are discussed. Secondly, the simple regression plots between the different pressure methods are discussed. Finally, the different water vapour pressure equations will be compared to determine the best way to include water vapour.

6.2 Motivation

In this section the motivation for the location, and the use of specific instrumentation is given. The PWV histograms, wind histograms and the implications thereof are also described in this section.

As is known, the wind problem at the SANAE IV base causes significant problems in the counting rate of the neutron monitors. In Figure 3.3 the histogram for wind speeds at three different locations is shown. The three locations are the SANAE IV base, Nelspruit and Sutherland. For the SANAE IV base the mean of the data is 10.3 m/s, the median 9.7 m/s, and the standard deviation 6.1 m/s. The values range from 0.0 m/s to speeds up to 42.4 m/s. For the Sutherland base the mean of the data is 3.4 m/s, the median 5.0 m/s, and the standard deviation 3.2 m/s. The values range from 0.0 m/s to speeds up to 15.0 m/s. For the Nelspruit base the mean of the data is 1.7 m/s, the median 1.7 m/s, and the standard deviation 1.2 m/s. The values range from 0.0 m/s to speeds up to 61.7 m/s. Thus, the SANAE IV base has much higher wind speeds than any one of these two bases. It has a mean 6.9 m/s greater than Sutherland, and 8.7 m/s greater than Nelspruit. SANAE IV does not have the greatest maximum value, Nelspruit has a maximum value 19.3 m/s larger than SANAE IV. This value does not mean much as it is only an outlier. From this it is obvious that SANAE IV has greater than normal wind speeds. Therefore this base is suitable for the proposed study, with regard to wind speed.

The reason low water vapour values are so important, is that it makes it possible to implement GPS technology. As was shown in Chapter 4 the GPS is largely affected by water vapour in the atmosphere. To determine the water vapour in the atmosphere is by making use of the KWV pressure theory; discussed in Section 5.2. The histogram for the KWV equation, given by (5.18) for three bases is shown in Figure 6.1. The gray bars are for the SANAE IV base, the red bars for Sutherland, and the blue bars for Nelspruit. In the figure the relatively low KWV values for the SANAE IV base, compared to the other two bases, are apparent. For the SANAE IV base the mean is 2.0 hPa, the median is 1.6 hPa and the standard deviation is 1.1 hPa. The values range from 0.3 hPa to 7.1 hPa. For the Sutherland base the mean is 7.6 hPa, the median is 7.0 hPa and the standard deviation is 3.2 hPa. The values range from 0.0 hPa to 37.2 hPa. For the Nelspruit base the mean is 14.2 hPa, the median is 14.3 hPa and the standard deviation is 6.0 hPa. The values range from 0.0 hPa to 37.2 hPa. Thus, SANAE IV has the

lowest mean, standard deviation and maximum values. Sutherland has the second highest values and Nelspruit the highest.

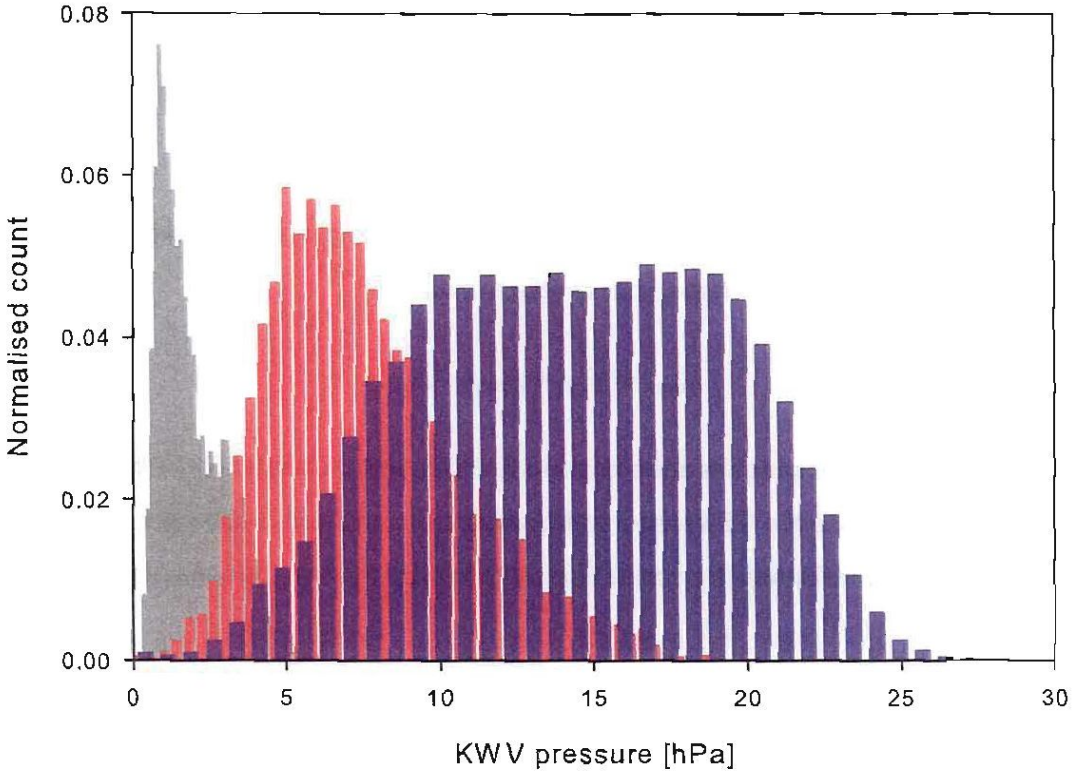

Figure 6.1: Histogram of KWV at the three different bases. The gray bars are for SANAE IV, the red bars for Sutherland, and the blue bars for Nelspruit.

6.3 Simple regression plots

In this section five methods for determining the atmospheric pressure at the SANAE IV base are discussed. The first method is by making use of the paroscientific barometer which was discussed in Section 2.11.3. This method's equipment is affected by wind, as was discussed in Section 3.2. The barometer is also affected by the additional pressure of the water vapour in the atmosphere. This term will be from this point onwards be referred to as P_{pwv}, in addition to the pressure of dry air, P_{air}.

The data for this chapter came from different sources, and are for different time ranges. Most of these data are for the period beginning of 2000 till end of 2006. Where these dates differ

for a certain set of data, it will be mentioned. The neutron monitor pressure data, for the SANAE IV base are from the USP of the NWU. The weather data, consisting of the wind speed, temperature and relative humidity were supplied by the SAWS. All GPS-related data were obtained from the HartRAO Space Geodesy Programme, which serves as the regional data and analysis centre for geodesy. Lastly, the PWV data were obtained from NCEP, and the interpolation thereof was done by the HartRAO Space Geodesy Programme. All the data have been averaged to 6-hourly values..

The pressure method is affected by the pressure of the air and water vapour, as well as the effect of wind. In principle, therefore, one is able to state that

$$P_{\text{baro}} = P_{\text{air}} + P_{\text{pwv}} + P_{\text{wind}}. \tag{6.1}$$

The wind term in this equation is added due to the findings in Chapter 3; the Bernoulli effect. The rest of the methods are GPS-based and therefore this method is the only method of the five considered here influenced by wind. This method will therefore be used as the "reference" method.

If all major variables are taken out of the GPS and barometric determined pressures, one should in theory have a line, with slope m=1, through the origin. Around this line there should be scatter, the amount of scatter determining the accuracy of the combined data sets. In Section 2.10.2. it was shown that when the pressure increases with 1 mm Hg, the counting rate of the neutron monitor decreases by 1%. According to *Malan and Moraal* (2002) the statistical accuracy required at SANAE IV is 0.14%, therefore the atmospheric pressure should be accurate to 0.14 mm Hg. In this dissertation the unit used for atmospheric pressure is hPa, and 1 mm Hg is equal to 1.33 hPa, therefore the atmospheric pressure should be accurate to 0.19 hPa.

The pressure values for the first GPS method (Method 2), are named $P_{\text{GPS(0)}}$. The zero refers to the fact that no PWV will be taken into account. This means that it is assumed that the atmosphere is only constituted of air, and no water vapour. Therefore this data set will not have the advantage of having the PWV eliminated, as with the other GPS methods.

Method 2 is based on the assumption that the PWV in the atmosphere is zero. A standard atmosphere of 1013 hPa is equivalent to a ZTD of 2303 mm. Thus from the proportionality

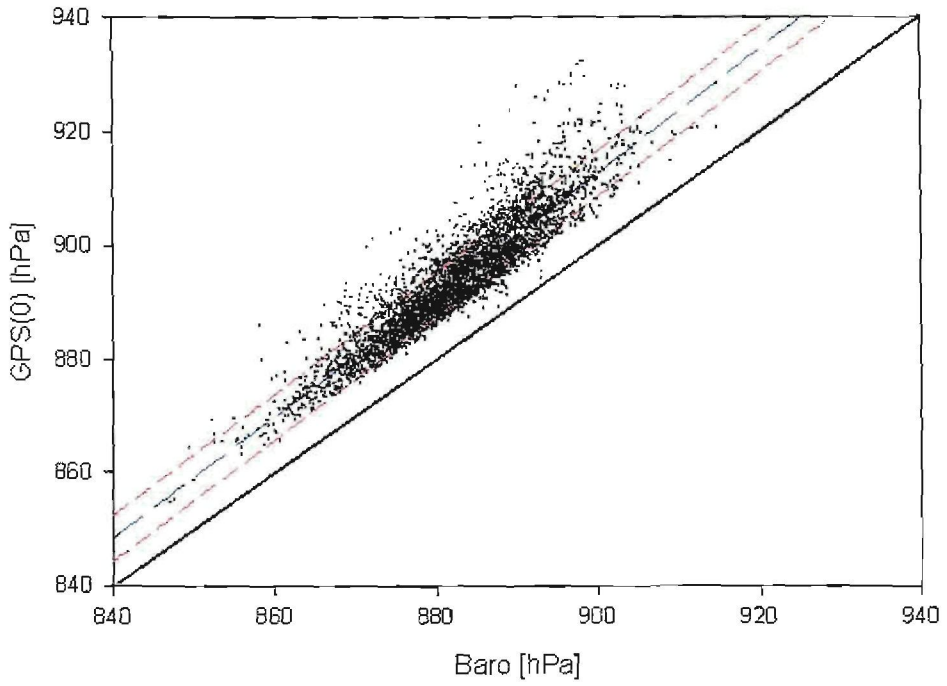

Figure 6.2: The relation between $P_{\text{GPS(0)}}$ and P_{baro}. The black line is for a line with slope m=1 through the origin, the blue line is the linear fit, and the red dashed lines indicate the 66% prediction band.

$P/ZTD = P(1\text{ atm})/ZTD(1\text{ atm})$, it follows that atmospheric pressure from ZTD is given by

$$P = \frac{\text{ZTD (mm)}}{2.2725}\ \text{hPa}. \tag{6.2}$$

In this method the atmospheric pressure is in theory affected by

$$P_{\text{GPS(0)}} = P_{\text{air}} + P_{\text{pwv}} + P_{D_{H_2O}}. \tag{6.3}$$

The $P_{D_{H_2O}}$ term refers to the dipole effect of water molecules on the GPS-signal. According to *Combrink* (2006) the delay of an electromagnetic signal in the troposphere depends on the density of each species of gas present therein. The expression given by *Debye* (1929)

$$N = \sum_{i=1}^{q} \rho_i (A_i + B_i/T), \tag{6.4}$$

is used to determine the delay. The density is indicated by ρ_i, the temperature by T and A_i and B_i are constraints for the specific species of gas. For diatomic and monatomic gases $B_i = 0$, however for H_2O, $B_i \neq 0$ because it has a permanent dipole moment. The details thereof and the derivation of (6.5) fall outside the scope of this study. For a discussion see *Combrink* (2006). The difference between (6.1) and (6.3) is found in the wind and water dipole terms.

In Figure 6.2 the linear relation between $P_{\text{GPS}(0)}$ and P_{baro} is shown. The black line in the figure is for the expected value if wind and the dipole effect of PWV does not affect the data sets. For this linear relation the equation of the line is $P_{\text{GPS}(0)} = -54.58 + 1.07(P_{\text{baro}})$. The line has a 66% prediction band of ~4.05 hPa, and a R^2 value of 0.843. The offset is due to the $P_{D_{H_2O}}$ term in (6.3). In the next three methods the PWV term will be included which will eliminate the $P_{D_{H_2O}}$ effect.

The pressure is determined via an equation given by *Combrink* (2006). It is

$$P_{GPS(pwv)} = \frac{\text{ZTD} - (0.102 + \frac{2396}{98.2+T})\text{PWV}}{2.2725}, \tag{6.5}$$

where P is the atmospheric pressure measured in hPa, T the atmospheric temperature measured in K, ZTD the zenith tropospheric delay measured in mm, and PWV the precipitable water vapour measured in mm. The units of PWV are mm, which indicates the thickness of the layer of water which will be obtained if the water vapour density above a specific point is integrated and the vapour allowed to condensate.

In Method 3 the NCEP-data sets were used to determine PWV; see Section 5.3. Using this data-set, one is able to determine the atmospheric pressure using (6.5). The pressure term of this method is named $P_{\text{GPS(pwv)}}$. This method's atmospheric pressure takes the PWV term into consideration, and therefore

$$P_{\text{GPS(pwv)}} = P_{\text{air}} + P_{\text{pwv}}. \tag{6.6}$$

The dipole term $P_{D_{H_2O}}$ does not influence the pressure term anymore, and therefore this term is the same as for the paroscientific barometer, (6.1), except that the wind term is not included.

Figure 6.3 is for $P_{\text{GPS(pwv)}}$ against P_{baro}. The equation of the best linear fit to this data is $P_{\text{GPS(pwv)}} = -92.75 + 1.11(P_{\text{baro}})$. The line has a 66% prediction band of ~6.25 hPa, and an R^2 value of 0.705. The data set is above the m=1 line, but not as much above as for Figure 6.2. This is because of the added PWV term, which eliminates the $P_{D_{H_2O}}$ term. The three indicators of accuracy, the 66% prediction band, standard deviation, and R^2 term all have bigger values than for Figure 6.2. This shows that the accuracy of our Method 3 has decreased, not increased as expected. The possible reason for this inaccuracy might be that our linear interpolation done on the NCEP-data, in Section 5.3, is inaccurate.

Method 4 makes use of an alternative method for determining the water vapour in the atmo-

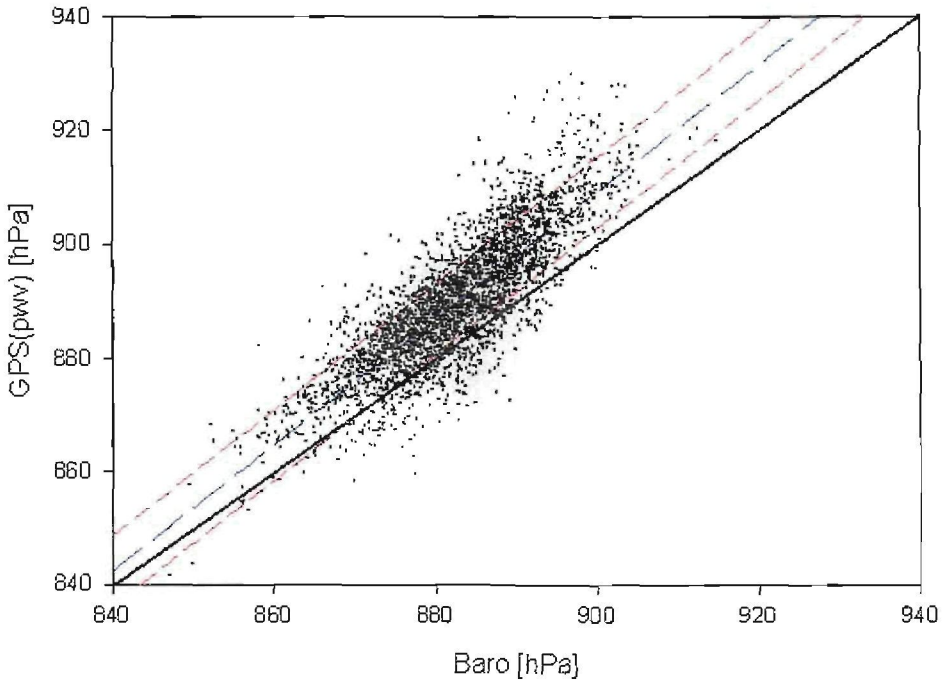

Figure 6.3: The linear relation between $P_{\text{GPS(PWV)}}$ and P_{baro}. The black line is for a line with slope m=1 through the origin, the blue line is the linear fit, and the red dashed lines are the 66% prediction band.

sphere, and using it to find the atmospheric pressure by GPS. This formula is given by *Merry* (2006)

$$P = \frac{\text{ZTD}}{2.2725} - (\frac{1255}{T} + 0.05)RH\text{x}KWV, \tag{6.7}$$

where P_e is the water vapour pressure in hPa, T the atmospheric temperature in K, and RH the relative humidity (maximum 1). This equation is similar to (6.5) except for the PWV term replaced by the $KWV\text{x}RH$ term. The total water vapour pressure is given by the *Kuemmel* (1997) expression in (5.18). The values of RH were supplied by SAWS. All data measured for calculating the atmospheric pressure were taken locally, that is at the base itself. This will probably make the pressure values more accurate than with the NCEP-interpolation method.

Figure 6.4 shows the linear relation between $P_{\text{GPS(kwv)}}$ and P_{baro}. The $P_{\text{GPS(kwv)}}$ term is the atmospheric pressure as determined using Method 4. For this relation the equation of the best linear fit is $P_{\text{GPS(kwv)}} = -97.78 + 1.12(P_{\text{baro}})$. The line has a 66% prediction band of ~6.32 hPa, and a R^2 value of 0.705. This graph is in essence the same as Figure 6.3. The only two differences are firstly the offset which is much smaller for Figure 6.4, and secondly the standard deviation which is smaller than for Figure 6.3. The standard deviation is ~5 hPa smaller than Figure 6.3. Although the standard deviation is smaller than Figure 6.3, it is still ~5 hPa bigger

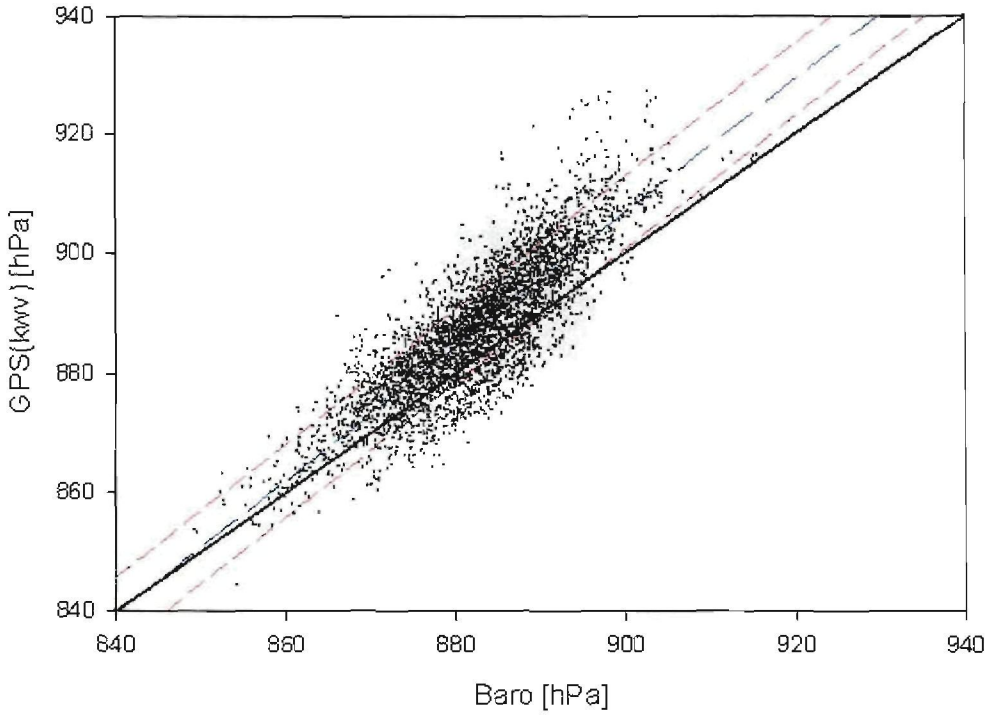

Figure 6.4: The linear relation between $P_{GPS(kwv)}$ and P_{baro}. The black line is for a line with slope m=1 through the origin, the blue line is the linear fit, and the red dashed lines are the 66% prediction band.

than Figure 6.2. This indicates that Method 4 is more accurate than Method 3. Some variables still need to be eradicated to become more accurate than Method 2.

Two problems in determining the water vapour pressure may exist. The first of these is that (5.18) has not been constructed for temperatures as low as for the SANAE IV base. The other problem is that the relative humidity was determined at ground level and the value may depend on altitude. Furthermore the relative humidity may be faulty, this will be discussed in Section 6.5.

Method 5 uses the same technique as Method 4, with the exception of the way the water vapour equation is determined. Instead of the KWV equation, the Goff-Gratch water vapour equation will be used. According to *Vomel* (2006) the Goff-Gratch equation of 1957 is used to predict the correct values for the total water vapour pressure between temperatures of -60°C and 102°C. The equation is

$$\begin{aligned} \mathrm{Log}_{10}P_e &= 10.79574(1-273.16/T) - 5.02800\mathrm{Log}_{10}(T/273.16) + 1.50475\,10^{-4}(1-10^{-8.2969(T/273.16-1)}) \\ &+ 0.42873\,10^{-3}(10^{+4.76955(1-273.16/T)}-1) + 0.78614, \end{aligned}$$

where the total water vapour pressure P_e is measured in hPa, and atmospheric temperature T in K.

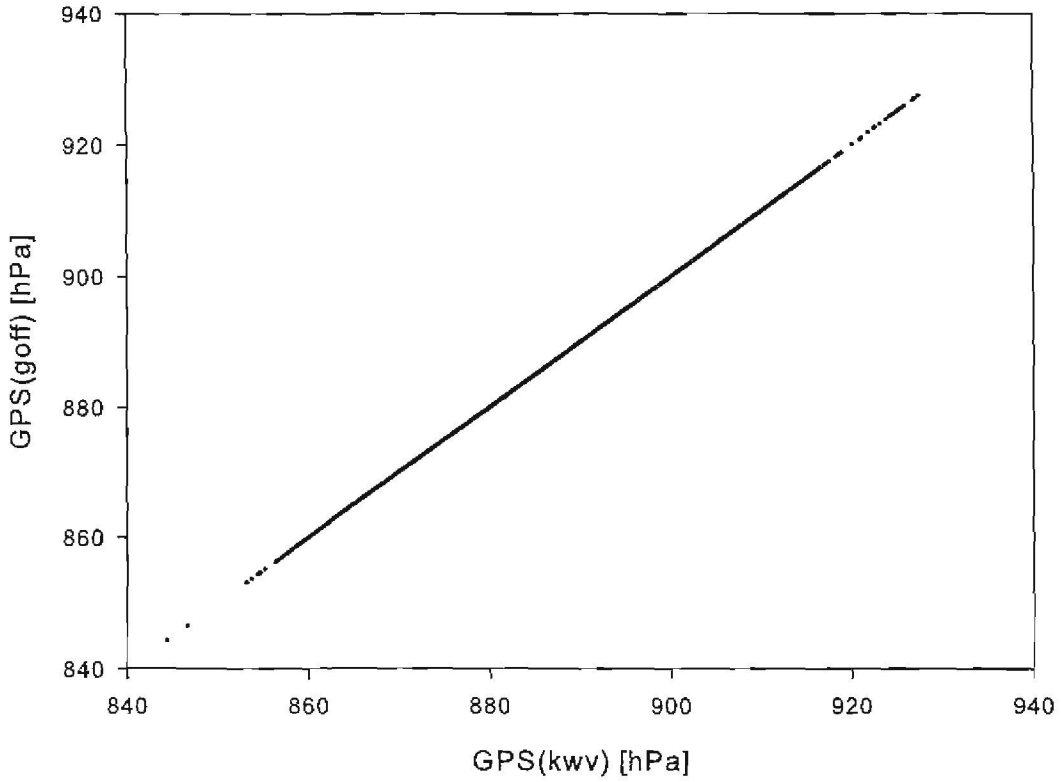

Figure 6.5: The linear relation between $P_{GPS(goff)}$ and $P_{GPS(kwv)}$. The result is a straight line through the origin.

In Figure 6.5 the relationship between $P_{GPS(goff)}$ and $P_{GPS(kwv)}$ is shown. It is apparent that there is a very strong if not exact correlation between these two atmospheric pressures. For this linear relation the two methods are almost identical, and therefore the Goff-Gratch method will not be used.

Therefore by not taking the water vapour into account one finds a significant deviation between the GPS pressure and the barometric pressure. The problem is that one has a very large offset. When including the water vapour one finds a very small offset, but larger standard deviations. What is rather interesting is the way the water vapour equations differ so much. In the next section the different GPS-pressures will be compared one another to learn some

properties of the water vapour equations.

6.4 Validation of PWV methods

In the previous section, five different methods of finding the atmospheric pressure were discussed. The first of these methods was by a Paroscientific barometer. The second method was done assuming that PWV does not influence the pressure much, and therefore was neglected. The last three methods used different ways to determine the water vapour pressure. In this section those last three results are plotted against one another to find out whether they are the same or whether they differ significantly. In this section it is assumed that the RH as supplied by the SAWS is correct.

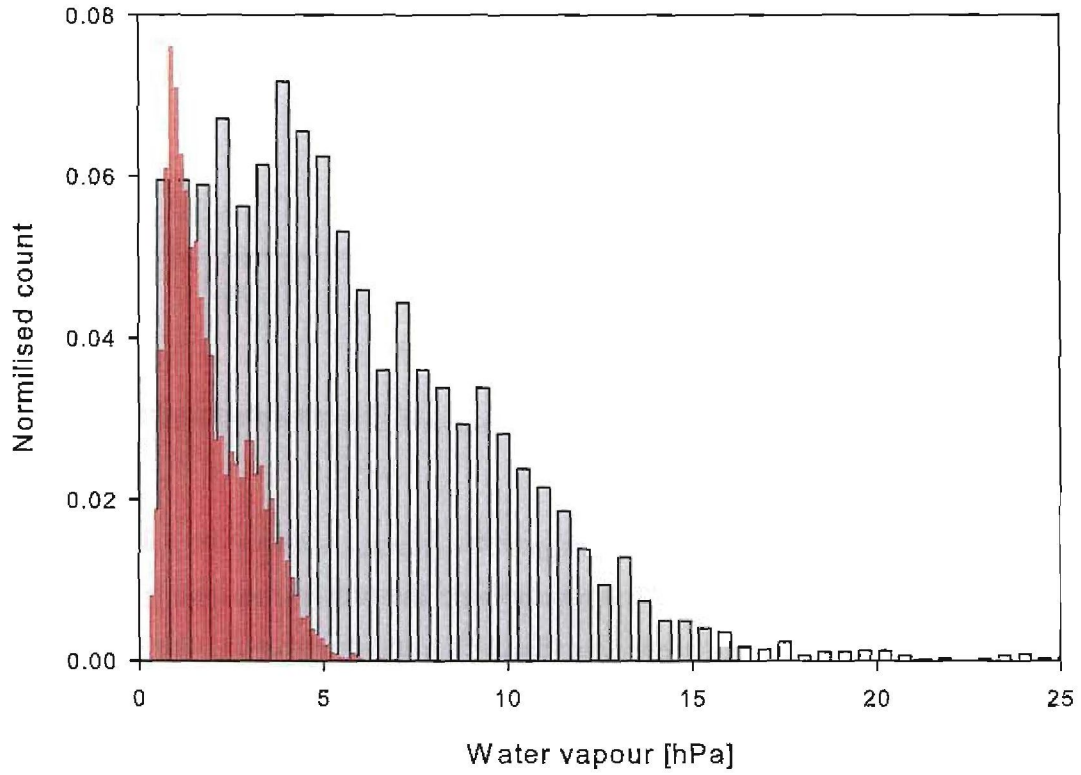

Figure 6.6: Both the KWV and PWV histograms for the SANAE IV base. The red bars are for the KWV values, and the gray bars for the PWV values. The PWV spread is up to 25 hPa compared to only 5 hPa for the KWV values.

Figure 6.6 shows the water vapour histogram for the SANAE IV base. In this histogram the gray bars are for the PWV values and the red bars for the KWV values. For the PWV values

the mean of the data is 5.7 hPa, the median 4.9 hPa, and the standard deviation 3.9 hPa. The values range from 0.4 hPa to 27.6 hPa. For the KWV values the mean of the data is 2.0 hPa, the median 1.6 hPa, and the standard deviation 1.1 hPa. The values range from 0.3 hPa to 7.1 hPa. From this figure and the statistics thereof the inconsistency of the PWV data already discussed in Section 4.3 becomes apparent.

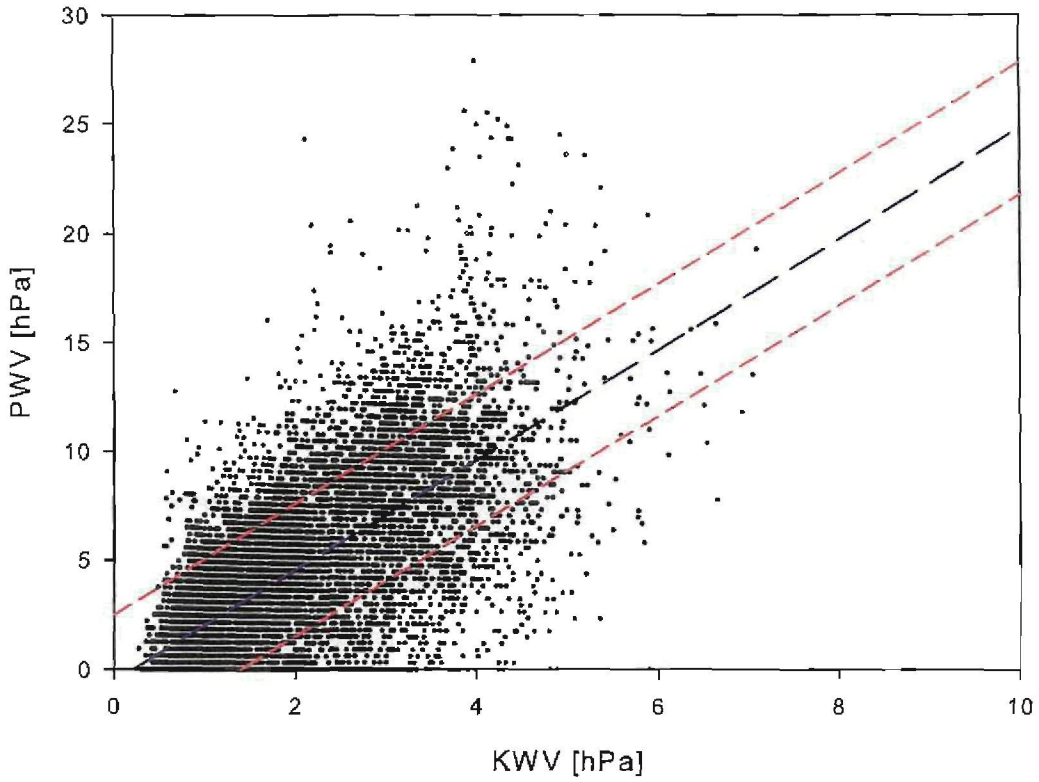

Figure 6.7: The linear relation between corrected PWV and KWV. The blue line is the linear fit, and the red dashed lines are the 66% prediction band.

Figure 6.7 shows that the correlation between KWV and PWV is very poor. One would expect the slope to be equal to one, as both these variables are indicators of atmospheric water vapour. At water vapour pressures below 0.3 hPa there are no data points for KWV, but for PWV there are numerous data points below this water vapour pressure. The reason for this is the fact that PWV values are sometimes zero and therefore will convert to values very close to 0 hPa. For KWV this is not true, as the values are determined by the RH and temperature; not one of these variables is able to produce values close to 0 hPa.

In Figure 6.8 $P_{GPS(pwv)}$ is plotted against $P_{GPS(0)}$. For this linear relation the equation of the line

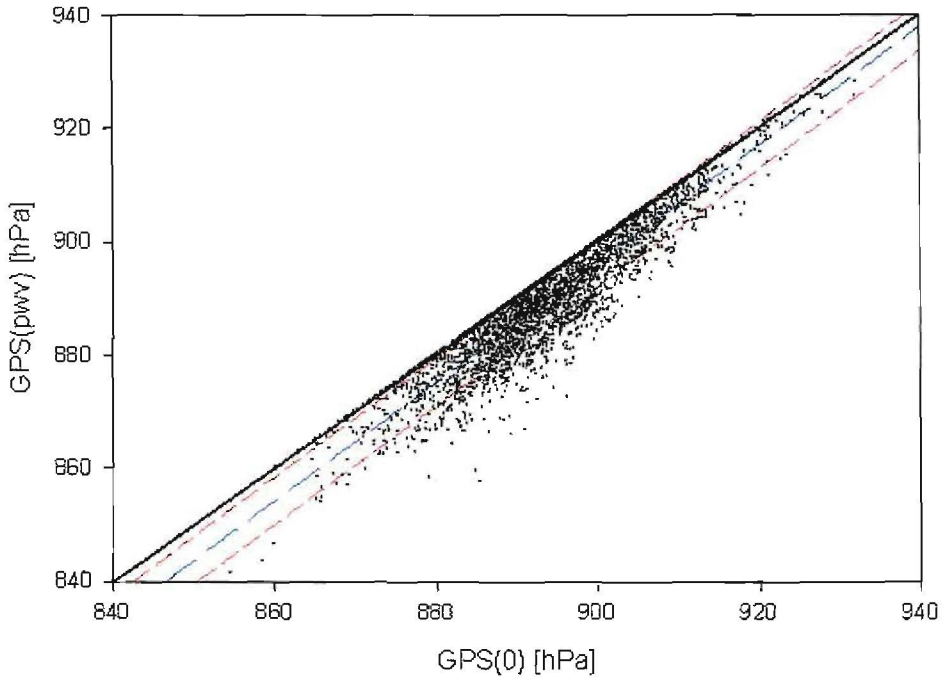

Figure 6.8: The relation between $P_{GPS(pwv)}$ and $P_{GPS(0)}$. The black line is for a line with slope m=1 through the origin, the blue line is the linear fit, and the red dashed lines are the 66% prediction band.

is $P_{GPS(pwv)} = -44.17 + 1.04(P_{GPS(0)})$. The line has a 66% prediction band of ~4.19 hPa, and a R^2 value of 0.869. Furthermore, all the points are less or equal to the m=1 line. This shows that the maximum line for this relation is where PWV=0, because then $P_{GPS(pwv)} = P_{GPS(0)}$. When PWV≠0, $P_{GPS(pwv)} < P_{GPS(0)}$, because the D_{H_2O} effect is substracted. Furthermore one is able to detect that the frequency of low $P_{GPS(pwv)}$ values increase with decreasing $P_{GPS(0)}$ values. This shows that at low pressures PWV values are higher. This makes sense as the higher PWV is, the greater the $P_{D_{H_2O}}$ effect.

The relation between $P_{GPS(kwv)}$ and $P_{GPS(0)}$ is shown in Figure 6.9. For this relation the equation of the best linear fit is $P_{GPS(kwv)} = -49.19 + 1.05(P_{GPS(0)})$. The line has a 66% prediction band of ~3.87 hPa, and a R^2 value of 0.887. The accuracy indicators show that the data are less spread out than for Figure 6.8. This suggests that the $P_{GPS(kwv)}$ values are higher for $P_{GPS(0)}$ than for the $P_{GPS(pwv)}$ values. To find out if this is true, one should plot $P_{GPS(kwv)}$ against $P_{GPS(pwv)}$. This is done in Figure 6.10. For this linear relation the equation of the line is $P_{GPS(kwv)} = 30.98 + 0.96(P_{GPS(pwv)})$. The line has a 66% prediction band of ~2.96 hPa, and a R^2 value of 0.935. There is definitely a good linear relation between $P_{GPS(kwv)}$ and $P_{GPS(pwv)}$.

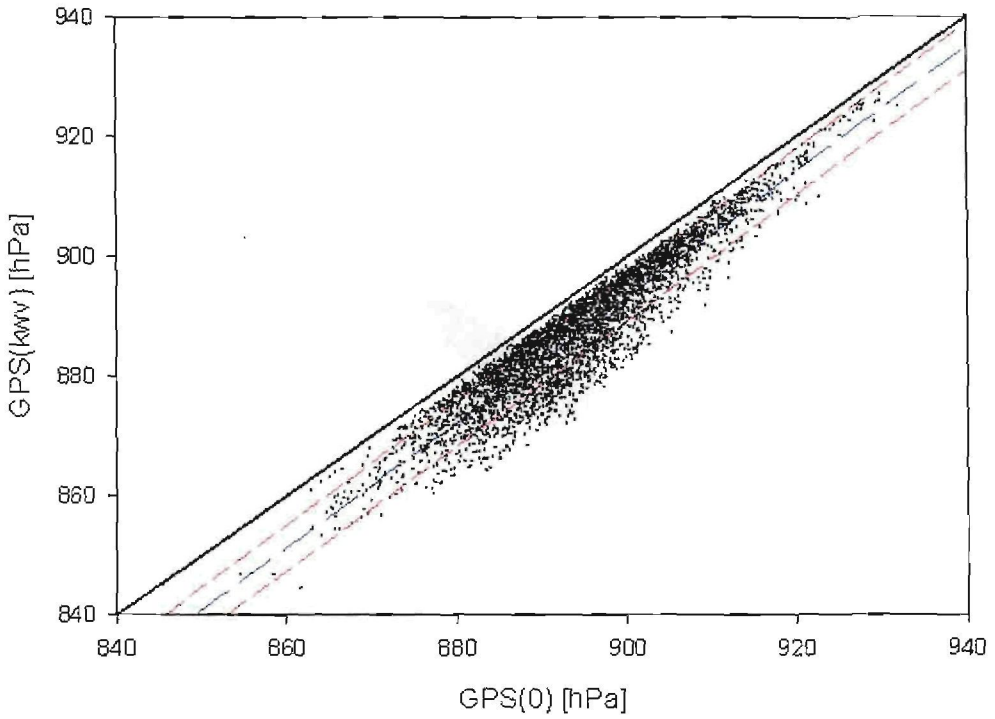

Figure 6.9: The relation between $P_{GPS(kwv)}$ and $P_{GPS(0)}$. The black line is for a line with slope m=1 through the origin, the blue line is the linear fit, and the red dashed lines are the 66% prediction band.

This indicates that both terms represent water vapour. There is one property that is rather concerning: it is the fact that the best fit line is below the m=1 line throughout the data range. It confirms a property seen in the previous figure. It confirms the fact that the KWV term has a smaller influence on the atmospheric pressure calculation than the PWV term. The fact that the influence is bigger at higher atmopheric pressure, suggests that the influence is larger where the water vapour on average is lower. This then supports our claims that the PWV data are inaccurate, because the low PWV values are overestimated.

In this section it was shown that the PWV and KWV terms are not in good agreement. What is suspect is the way they are off centre from the m=1 line, suggesting that they have different meanings or accuracies. Furthermore it was shown in Section 5.3 that the PWV values and the *Kuemmel* (1997) expressions do not correlate. Therefore from here onwards the PWV term will only be used to help explain the KWV properties.

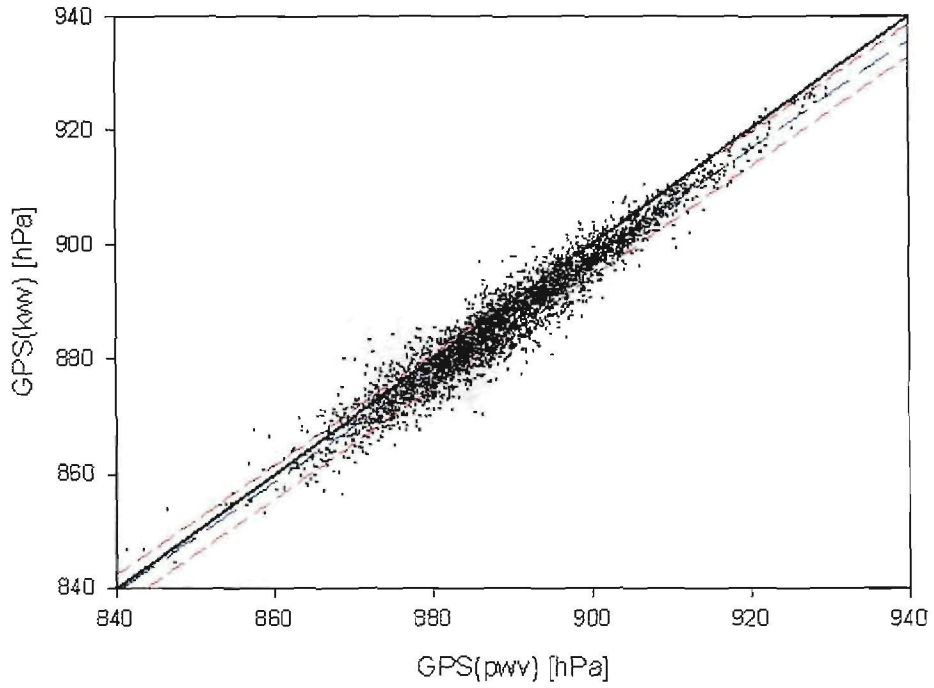

Figure 6.10: The linear relation between $P_{GPS(kwv)}$ and $P_{GPS(pwv)}$. The black line is for a line with slope m=1 through the origin, the blue line is the linear fit, and the red dashed lines are the 66% prediction band.

6.5 Relative humidity and its components

In this chapter the relative humidity (RH) and its properties will be discussed. This includes a discussion on the theoretically expected data values compared to those values supplied by SAWS. A correction for RH will be made and the validity thereof will be discussed. Lastly, the linear results in Chapter 6 will be compared to results, using the corrected RH.

In Figure 6.11 the histogram for the relative humidity, as defined in Section 5.3, supplied by SAWS for the SANAE IV base is shown. In this figure the histogram has two maxima, one at ~50% the other at ~80%. There are very few values below ~20%, and very few values above 90%. For the SANAE IV base the mean of the data is 63.0 %, the median 62.5 %, and the standard deviation 18.0 %.

When the RH is plotted as a function of atmospheric temperature, a density plot is found, the maximum value of which slants from high to low atmospheric temperature. This is shown in Figure 6.12. The top maximum relative humidity line is not equal to 100%. This is not what

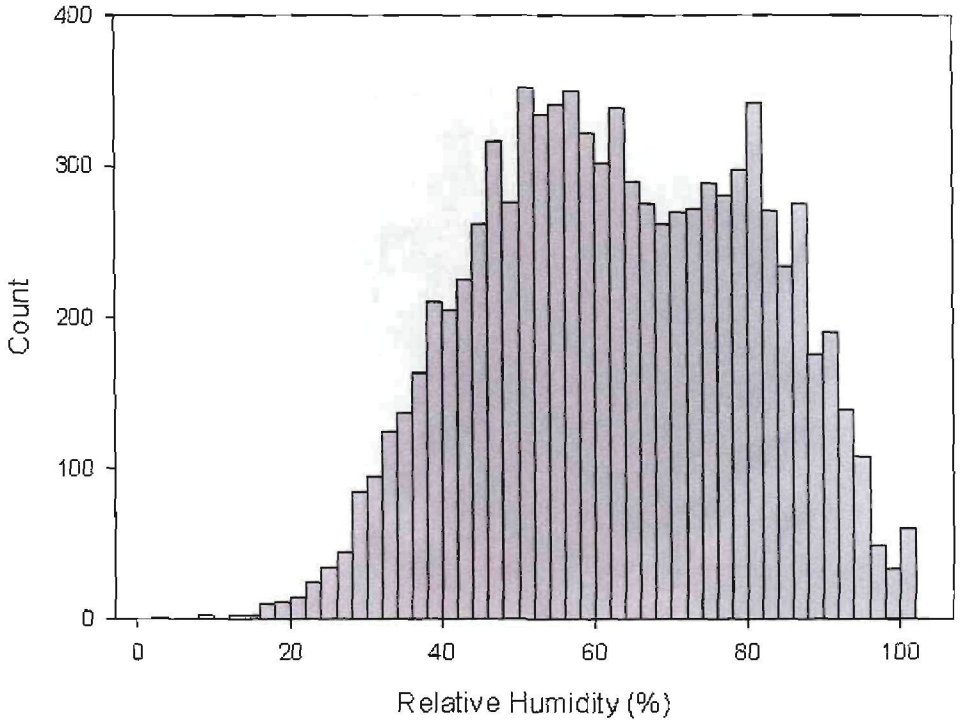

Figure 6.11: Relative humidity histogram constructed from SAWS data. The data is day quarterly, from 1998 till 2006.

is expected, as it is obvious that the maximum RH, i.e. the dewpoint, should not have any correlation with atmospheric temperature. No apparent reasons for this unexpected result can be given. Therefore the data will be adjusted to give a more theoretically sound result.

Assuming that the observations contain an error, they are adjusted by finding the regression of the maximum line and shifting all data to 100% with the help of it. This corrected data set is shown in Figure 6.13. The new RH will be called the corrected RH. Figure 6.13 shows what is theoretically expected; the maximum line is constant at 100% RH. It is important to validate the corrected RH. First, its validity will be tested by drawing a histogram, and comparing it to the RH histogram.

In Figure 6.14 the new corrected RH histogram is shown. For the SANAE IV base the mean of the data is 74.6 %, the median 74.7 %, and the standard deviation 17.4 %. The values range from 13.1 % to percentages up to 101.0 %. This value is possible due to the adjustment made to the RH. The histogram has two local maxima, one at ~70% and a larger one at ~95%. There is a relatively large local minimum at ~85%. The two peaks are consequences of the correcting

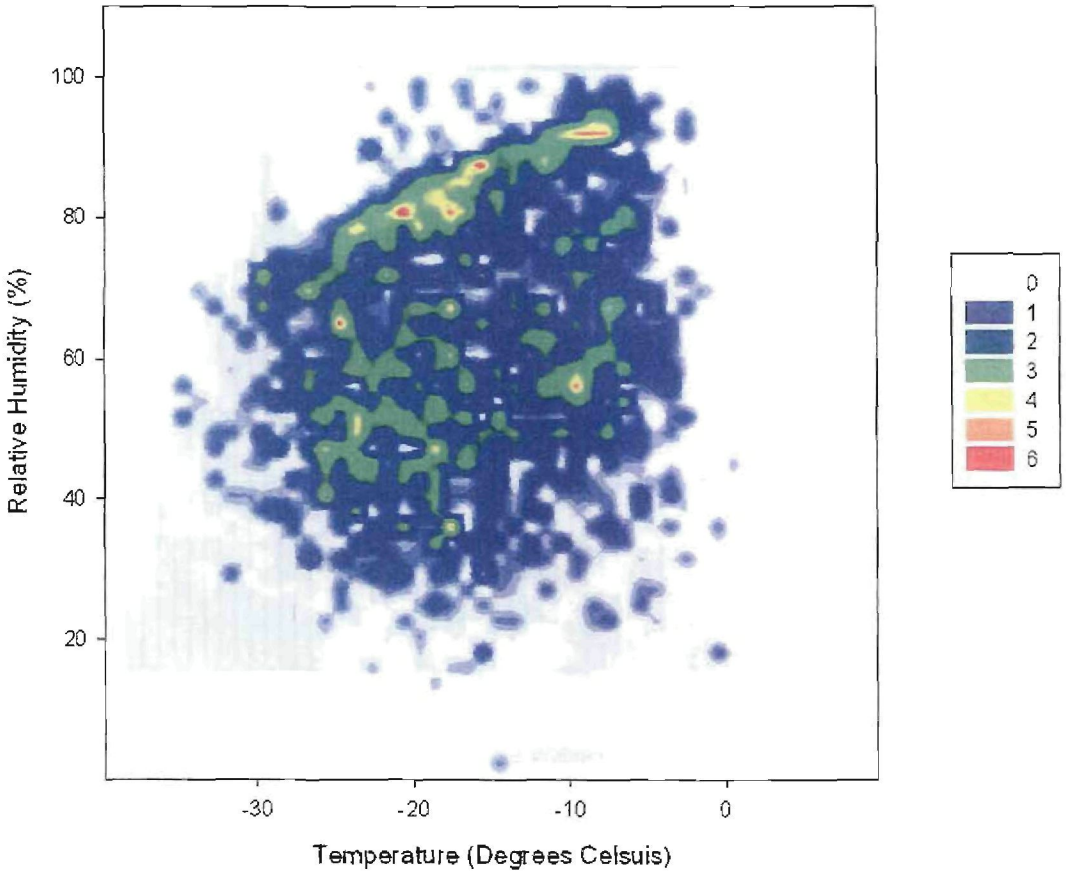

Figure 6.12: Density plot of relative humidity against atmospheric temperature. On the side of the graph, the density of data points is indicated.

of the RH. When one looks at Figure 6.12, two dense regions can be seen. Both these regions have slopes which make them dependent on atmospheric temperature. This is unphysical as has already been said. The slopes cause the histogram of RH, Figure 6.11, to have lower maxima and higher minima. The slope blurs out the densities in Figure 6.12. In Figure 6.13 the data are corrected, making the two density columns lie in straight horizontal lines. These horizontal lines can clearly be seen in the histogram of Figure 6.14. This does not validate the new corrected RH. The only way one is able to validate the method is to see if it makes the linear regression of barometric pressure versus GPS-derived pressure in Section 6.3 more accurate. This will now be attempted.

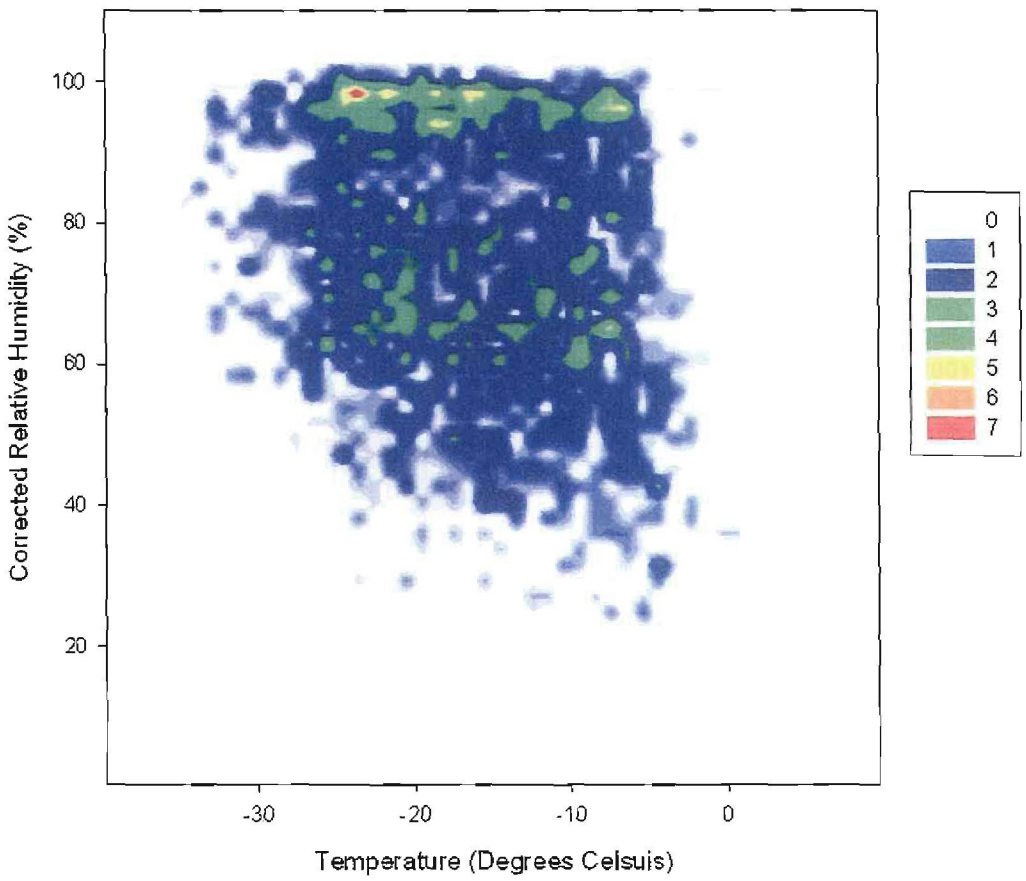

Figure 6.13: Density plot of corrected relative humidity against atmospheric temperature. The maximum line is constant at 100% corrected relative humidity. On the side of the graph, the density of data points is indicated.

6.6 The corrected regression plots

In this section the linear regressions of the $P_{GPS(kwv)}$ terms that have now been corrected will be discussed. The main idea is to validate the use of the new corrected RH term. The only way one is able to do this is to recalculate the accuracy indicators for the corrected KWV terms. This is done in the next three figures, in each figure the accuracy indicators will be discussed and compared to those in Section 6.3. At the end of the next section a conclusion will be given on the validity of the corrected RH.

In Figure 6.15 the linear relation between corrected $P_{GPS(kwv)}$ and P_{Baro} is shown. For this linear relation the equation of the line is corrected $P_{GPS(kwv)} = -98.37 + 1.12(P_{baro})$. The line has a 66% prediction band of ~6.25 hPa, and an R^2 value of 0.717. In Figure 6.4 the same

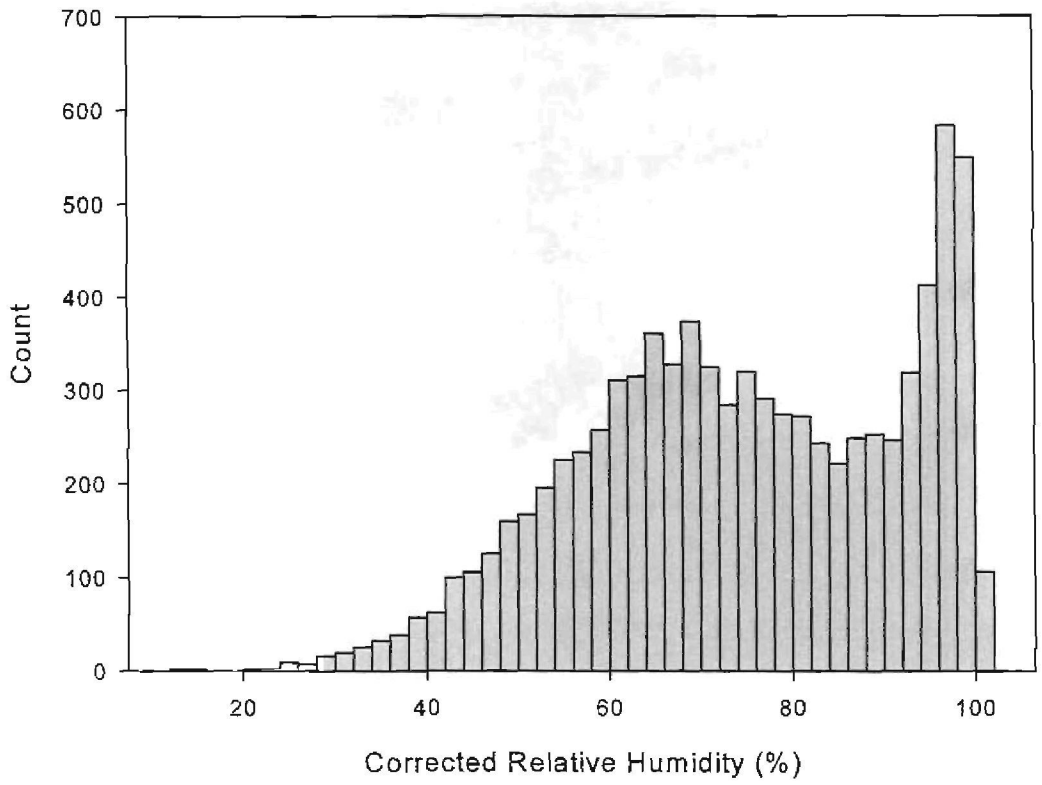

Figure 6.14: Histogram of the corrected relative humidity.

regression had a 66% prediction band value of 6.32 hPa, that is a difference of 0.07 hPa. The R^2 value was 0.705, that is a difference of 0.012. Thus the differences in the accuracy indicators are very small.

The corrected $P_{GPS(kwv)}$ term plotted against the $P_{GPS(0)}$term gives a linear relation, this is shown in Figure 6.16. For this linear relation the equation of the line is corrected $P_{GPS(kwv)} = -49.20 + 1.05(P_{GPS(0)})$. The line has a 66% prediction band of ~3.87 hPa, and an R^2 value of 0.887. In Figure 6.9 the same regression had a 66% prediction band value of 4.08 hPa, that is a difference of 0.21 hPa. The R^2 value in Figure 6.4 is 0.875, that is a difference of 0.012. The differences in the accuracy indicators are very small, but bigger than with the previous figure.

In Figure 6.17 the relation between corrected $P_{GPS(kwv)}$ and $P_{GPS(pwv)}$ is shown. For this linear relation the equation of the line is $P_{GPS(kwv)} = 30.98 + 0.968(P_{GPS(pwv)})$. The line has a 66% prediction band of ~2.96 hPa, and an R^2 value of 0.936. In Figure 6.10 the same regression had a 66% prediction band value of 2.98 hPa, that is a difference of 0.02 hPa. The R^2 value in Figure

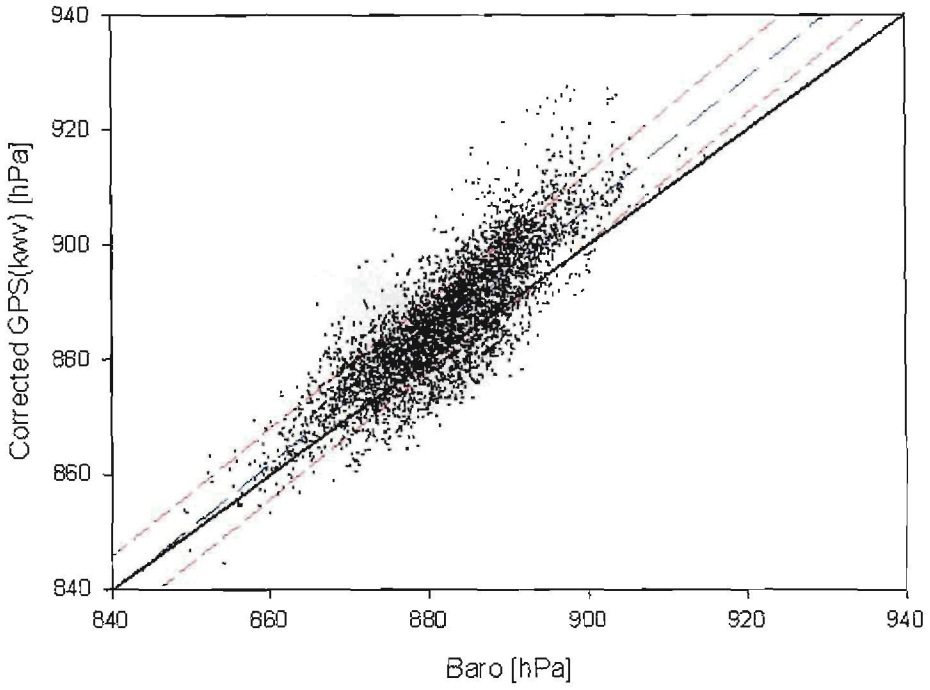

Figure 6.15: The linear relation between corrected $P_{GPS(kwv)}$ and P_{Baro}. The black line is for a line with slope m=1 through the origin, the blue line is the linear fit, and the red dashed lines represent 66% prediction band.

6.10 is 0.933, that is a difference of 0.003. Therefore the differences for this figure is the smallest of all three the figures.

In the discussions of the previous three figures, it was seen that the corrected RH term had a very small, if not none at all, role to play in the quality of the data. The reason for this is uncertain. The corrected RH did however make a difference to the accuracy, and for this reason, and the fact that it has a more physical meaning, it will be used from this point onwards. In the next section the atmospheric water vapour and its effect on the atmospheric pressure calculations will be investigated.

6.7 Properties of water vapour

In the previous section the question of the quality of the RH data was discussed. It was shown that by correcting the RH one gets similar results as in Section 6.3. In the following sections alternative ways to make the pressure data sets more accurate will be studied. In this section the properties of water vapour are studied. This study is started by showing that there is no

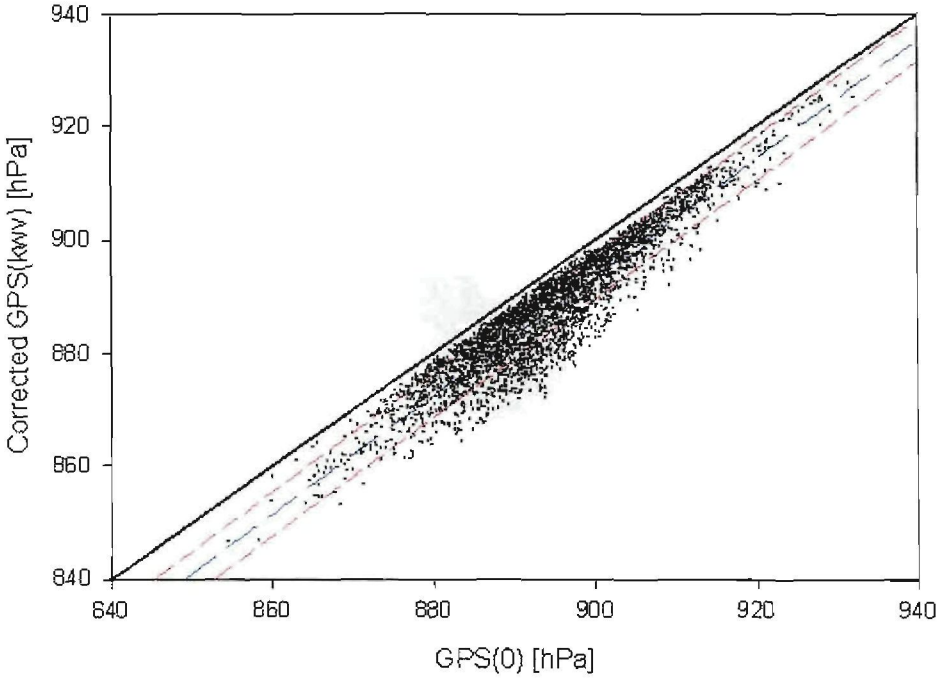

Figure 6.16: The linear relation between corrected $P_{GPS(kwv)}$ and $P_{GPS(0)}$. The black line is for a line with slope m=1 through the origin, the blue line is the linear fit, and the red dashed lines are the 66% prediction band.

correlation between atmospheric water vapour and wind speed; therefore they can be studied separately. Then the relation between the KWV- and PWV-equation will be investigated. Thereafter the correlation between precipitable water vapour and atmospheric temperature is analyzed. Furthermore, the relationship between derived atmospheric pressure and atmospheric water vapour pressure is studied. Thereafter the adjusted pressures will be plotted against each other as was done in Section 6.3. Lastly, a conclusion for the procedures and their success will be discussed.

6.7.1 Relationship between water vapour and wind speed

It should be emphasised that atmospheric water vapour is represented by two quantities, both of which has the temperature T as the determining variable, KWV and PWV; as has been discussed in Section 5.2. In this subsection the aim is to show that there is no relationship between wind speed and atmospheric water vapour. This is a motivation for the separate and independent study of wind speed and atmospheric water vapour effects.

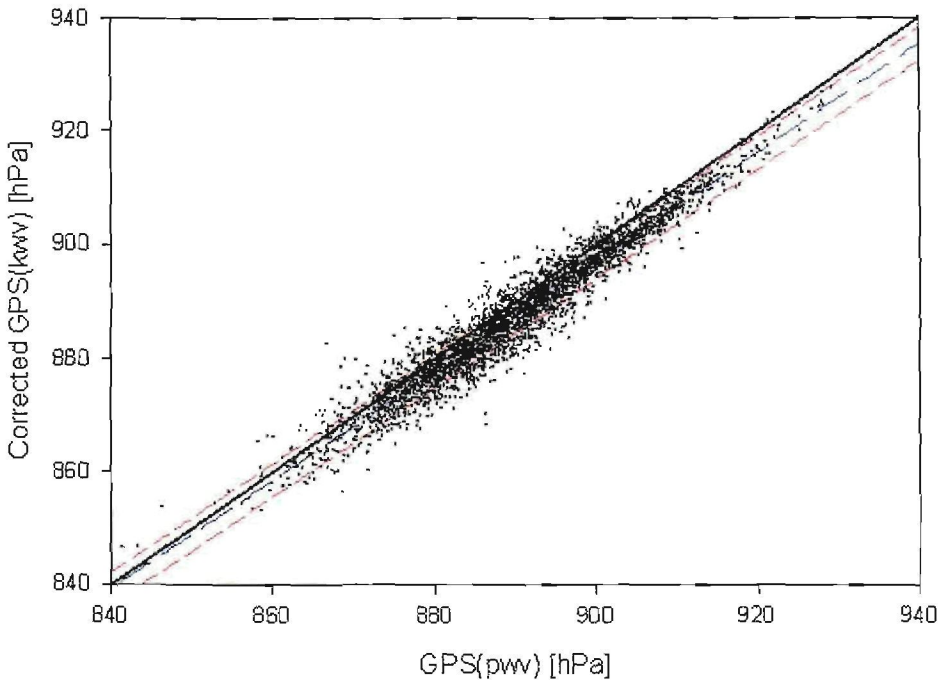

Figure 6.17: The linear relation between corrected $P_{GPS(kwv)}$ and $P_{GPS(pwv)}$. The black line is for a line with slope m=1 through the origin, the blue line are the linear fit, and the red dashed lines represent the 66% prediction band.

In Figure 6.18 the relation between PWV and wind speed is shown. The values in the figure are the average bin values for PWV. An average bin value is determined according to the bin it is found in. A bin is that section of wind speed with values $n \leq PWV < n + 1$ where $n = 0; 1; 2; ...; 40$. The black line in Figure 6.18 shows the linear relationship of the data points. In Figure 6.19 the relationship between KWV and wind speed is shown. The relationship is the same as for PWV shown in Figure 6.18. This is not unexpected as both PWV and KWV are indicators of atmospheric water vapour.

Through Figures 6.18 and 6.19 it therefore follows that that there is no correlation between atmospheric water vapour and wind speed. It is known that barometric pressure is influenced by wind speed, and GPS-derived pressure by atmospheric water vapour, Chapters 3 and 5. Therefore, the independence of these two variables points to the independence of correcting the different pressure data sets. Thus, correcting both the pressure data sets with wind speed, will have an effect on barometric pressure only, and not GPS-derived pressure. If one is able to study these variables separately and adjust the atmospheric pressure accordingly, then both variables may be excluded from the datasets. This will increase the correlation accuracy of the atmospheric pressure data sets.

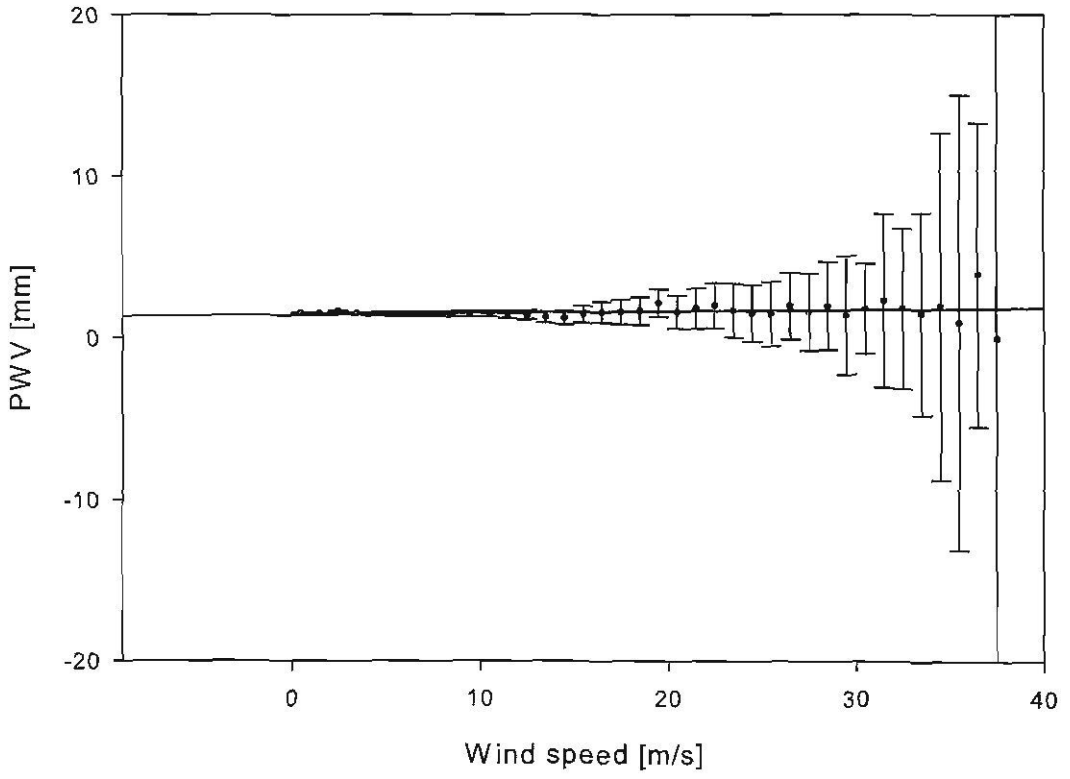

Figure 6.18: There is no relation between PWV and wind speed. The error bars indicate the standard deviation for the data points. The black line is the linear relation of the data points.

6.7.2 Contribution of water vapour to atmospheric pressure

In this subsection the aim is to show the contribution to atmospheric pressure by atmospheric water vapour. The relationship between these parameters is important as it gives insight in the properties of water vapour. The atmospheric pressure is plotted against both KWV and PWV. The subsection is finished by replotting the atmospheric pressures against each other and comparing them with those in Section 6.3.

In Figure 6.20 the average atmospheric bin pressure versus PWV is shown. The average atmospheric bin pressure is that pressure for $n \leq PWV < n + 0.1$ where $n = 0.0; 0.1; 0.2; ...; 4.0$. The error bars are for the standard deviation of an average atmospheric bin pressure data point. In this figure four linear regression plots are shown. The green plot is for the P_{baro}, the red plot is for $P_{\text{GPS(0)}}$, the black plot for $P_{\text{GPS(pwv)}}$ and the blue plot for $P_{\text{GPS(kwv)}}$.

One would expect the plot of P_{baro} to have none or little correlation with PWV. The reason is

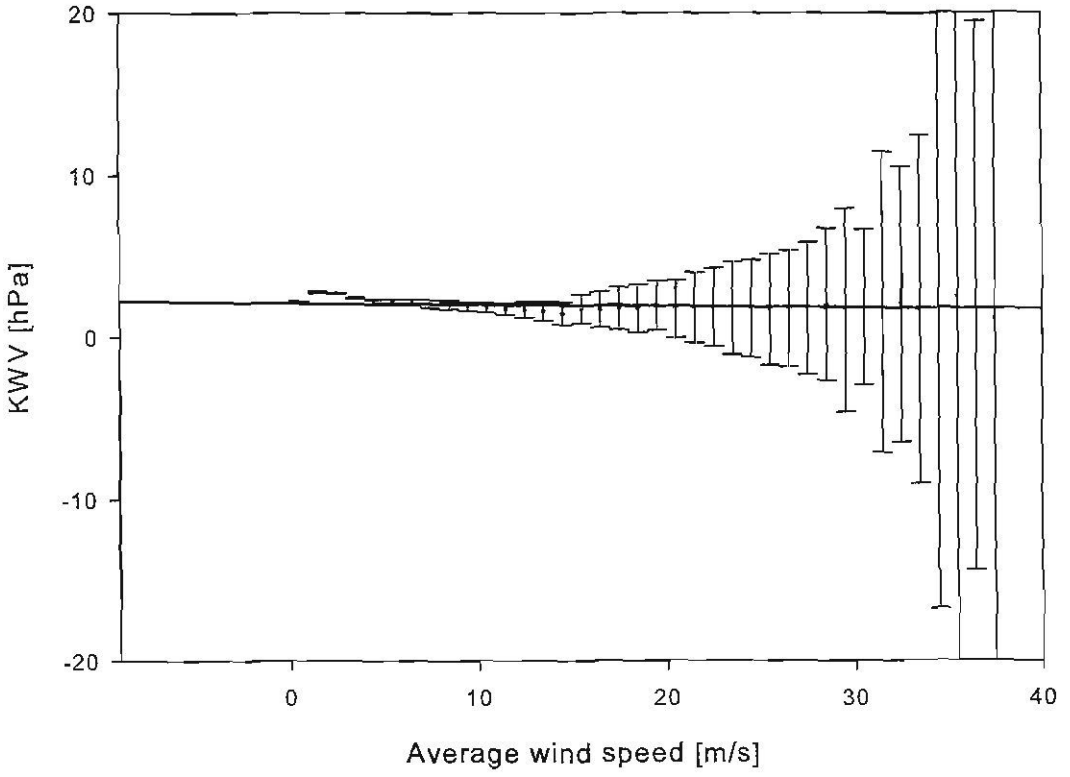

Figure 6.19: There is no relation between KWV and wind speed. The error bars indicate the standard deviation for the data points. The black line is the linear relation of the data points.

that according to (6.1), P_{baro} depends on the weight of the water molecules and not on their dipole property. This contribution of the weight will have at most a small effect on the slope of the correlation. One would expect P_{baro} to increase with increasing PWV; in Figure 6.20 this is not the case. The line has a negative slope, not the positive slope as is expected. A possible reason for this unexpected drop of pressure at high PWV is due to the properties of weather systems. High PWV values are an indication of a storm system at that specific location. Storm systems are co-existent with low-pressure systems. It is for this reason that at high PWV, P_{baro} might be lower.

For $P_{\text{GPS}(0)}$ the pressure is expected to increase drastically with increasing PWV. The reason for this is the extra effect of the dipole term, having an effect on $P_{\text{GPS}(0)}$. More PWV in the atmosphere enhances the effect of the dipole properties of water on $P_{\text{GPS}(0)}$. In Figure 6.20 this is not the case, a slight negative slope is seen. The slope has the same magnitude as P_{baro} slope, probably for the same reasons as above.

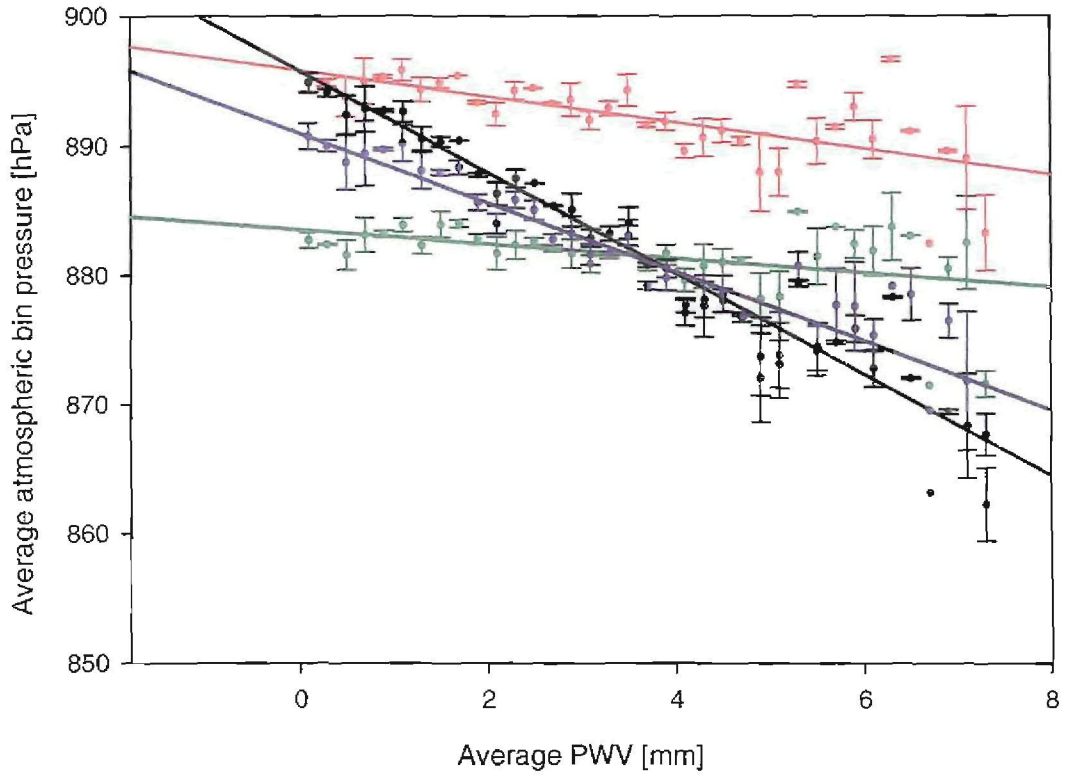

Figure 6.20: The linear relationships of the average atmospheric bin pressures against the average PWV. The green plot is for the P_{baro}, the red plot is for $P_{GPS(0)}$, the black plot for $P_{GPS(pwv)}$ and the blue plot for $P_{GPS(kwv)}$.

For the black and blue plots strong negative slopes are seen. Theoretically one would expect to have regressions with no slopes or slopes equal to P_{baro}. The introduction of PWV to the determination of atmospheric pressure has made it more dependent on PWV. The fact that the introduction of PWV has such an unexpected effects on atmospheric pressure is concerning. The problem does not lie in either the blue or black plot, these are mere consequences of the problem of $P_{GPS(pwv)}$. $P_{GPS(kwv)}$ and $P_{GPS(0)}$ are what is expected when one recognises that pressures are subtracted from P_{baro}. The higher the PWV value the bigger the value of pressure subtracted.

There are two indicators of atmospheric water vapour, and before a conclusion on the correlation between atmospheric pressure and water vapour can be discussed, KWV should be discussed as well. Figure 6.21 shows the average atmospheric bin pressure versus average KWV. In this figure the green plot represents P_{baro}, the red plot $P_{GPS(0)}$, the black plot is for $P_{GPS(pwv)}$ and the blue plot is for $P_{GPS(kwv)}$. The green plot, P_{baro}, has a small positive slope as

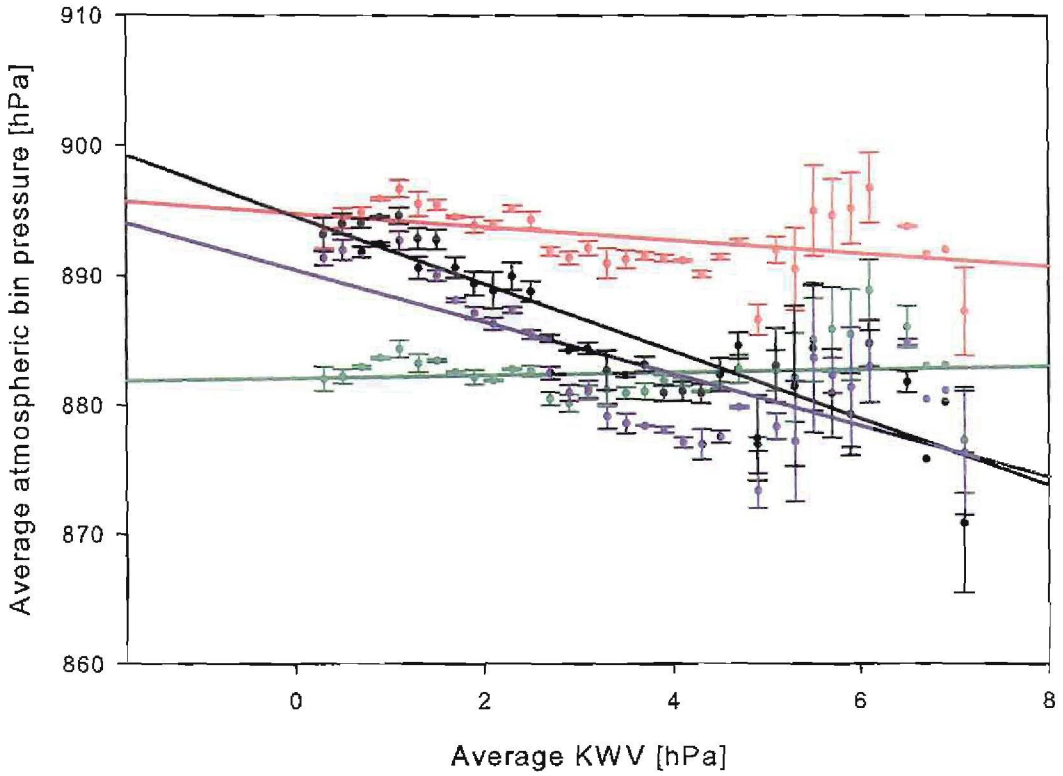

Figure 6.21: The linear relationships of the average atmospheric bin pressures against the average KWV. The green plot is for the P_{baro}, the red plot is for $P_{\text{GPS(0)}}$, the black plot for $P_{\text{GPS(pwv)}}$ and the blue plot for $P_{\text{GPS(kwv)}}$.

is theoretically expected. In both figures the red, blue, and black plots seems to be the same.

In the previous two figures it was shown that there is a correlation between $P_{\text{GPS(pwv)}}$, $P_{\text{GPS(kwv)}}$ and atmospheric water vapour. There is no correlation or very little between P_{baro} and atmospheric water vapour. Therefore one should subtract the P_{baro} term from the other terms and repeat Figures 6.20 and 6.21. This is done in Figures 6.22 and 6.23. The purpose of these graphs is to find the absolute dependence of the GPS-determined pressures. The term "absolute" indicates that the barometric pressure was subtracted.

In Figure 6.22 these absolute correlations are shown. The red plot is for $P_{\text{GPS(0)}} - P_{\text{baro}}$, the black plot is for $P_{\text{GPS(pwv)}} - P_{\text{baro}}$ and the blue plot is for $P_{\text{GPS(kwv)}} - P_{\text{baro}}$. All the plots have the same slope directions as in Figure 6.23. In this figure, the pressure values are only the residues, not the total pressure as in Figure 6.23. Two problems occur in the understanding of the figure. The first is the fact that there is such a significant difference between absolute $P_{\text{GPS(pwv)}}$ and

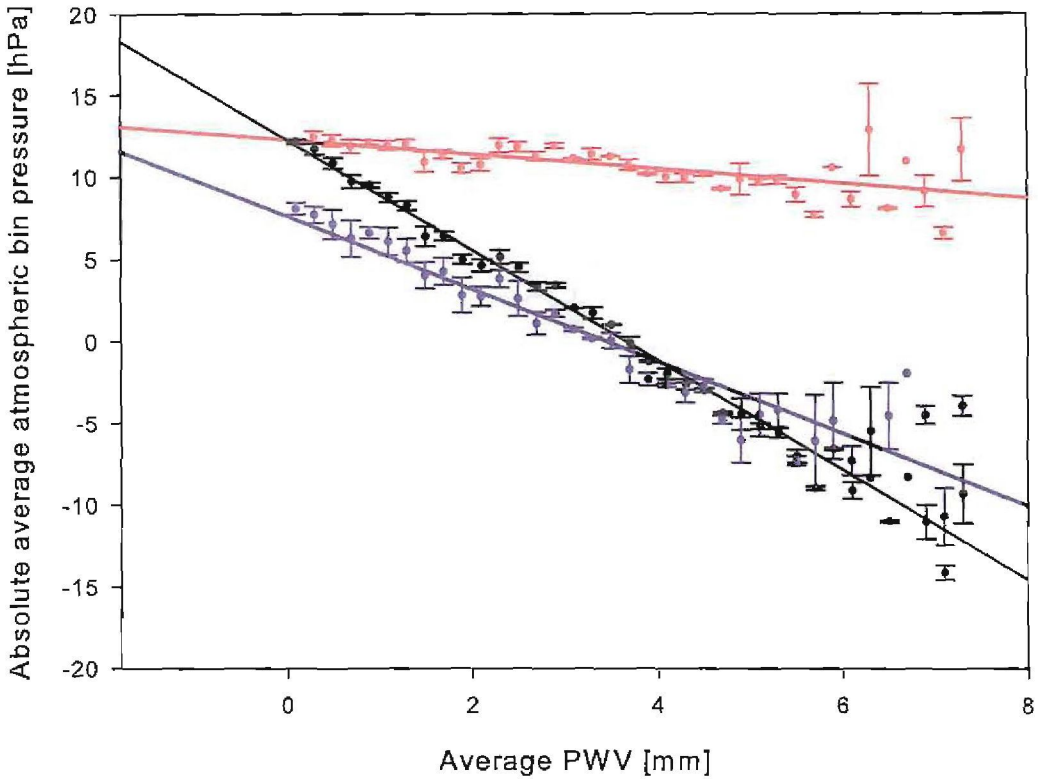

Figure 6.22: The linear relationships of the absolute average atmospheric bin pressures against the average PWV. The green plot is for the P_{baro}, the red plot is for $P_{GPS(0)}$, the black plot for $P_{GPS(pwv)}$ and the blue plot for $P_{GPS(kwv)}$.

$P_{GPS(kwv)}$. These two absolute pressures are only equal when KWV=PWV=4. The second unusual result is the fact that both the absolute $P_{GPS(pwv)}$ and $P_{GPS(kwv)}$ have values lower than P_{baro} at values ~3.5 PWV or KWV. This is unexpected, as one would expect P_{baro} to always be smaller or equal to the absolute $P_{GPS(pwv)}$ and $P_{GPS(kwv)}$ pressures. The reason for this is because when the atmospheric water vapour is included, only the wind term is left, which lowers P_{baro}. If PWV=0 then both $P_{GPS(pwv)} - P_{baro}$ and $P_{GPS(kwv)} - P_{baro}$ need to be equal to $P_{GPS(0)} - P_{baro}$. This is true for the black plot, but not for the blue plot. The reasons are unknown.

In Figure 6.23 the same results as in Figure 6.22 are shown with the exception of them being plotted against KWV. The black and blue plots are almost the same as in Figure 6.22 with two exceptions. The first is that these two linear regressions cross at a much higher relative water vapour value. Another thing which is of note is that in this figure there seems to be a kink in the blue and black plot. In both the plots this kink occurs at around ~4 hPa KWV value. The

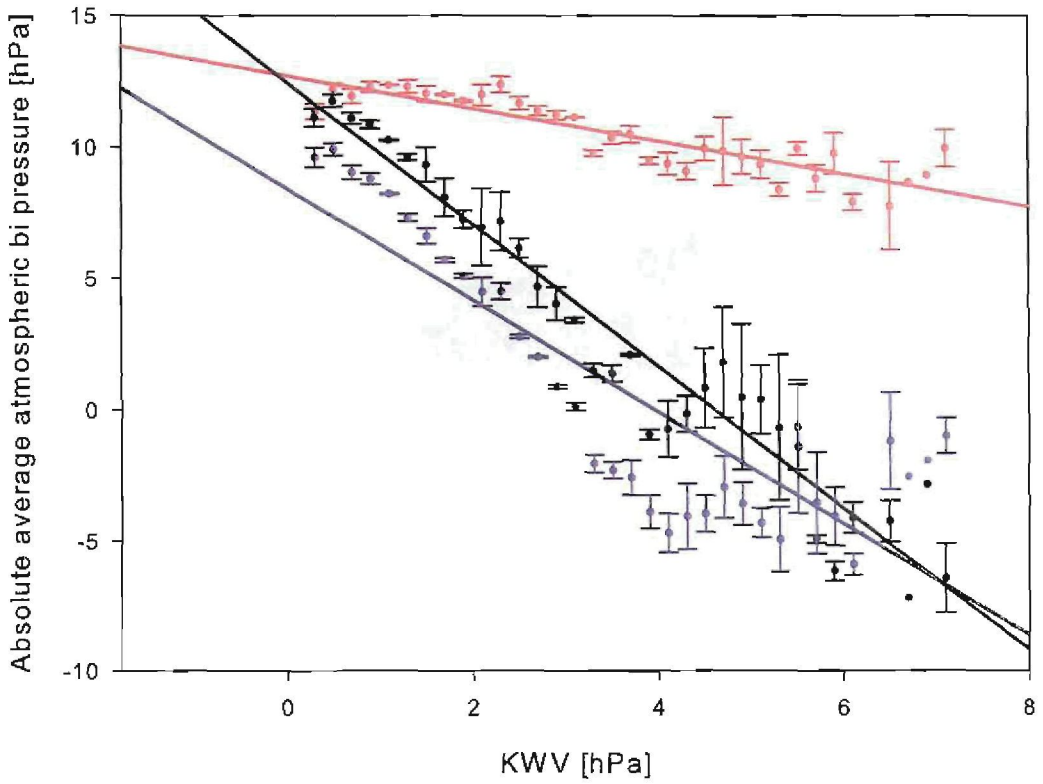

Figure 6.23: The linear relationships of the absolute average atmospheric bin pressures against the average KWV. The green plot is for the P_{baro}, the red plot is for $P_{\text{GPS(0)}}$, the black plot for $P_{\text{GPS(pwv)}}$ and the blue plot for $P_{\text{GPS(kwv)}}$.

kink was also found in Figure 6.22. The reason for this kink is unknown.

Assuming that the GPS-derived pressure should not depend on the water vapour, one can correct the data to have no correlation. In Figure 6.24 the correlation between $P_{\text{GPS(kwv)}}$ and KWV is shown. This correlation is more accurate than those in the previous pictures, as it is weighted. For this linear relation, the equation of the line is corrected $P_{\text{GPS(kwv)}} = 895.94 - 4.44(\text{KWV})$. The line has a 66% prediction band of ~10.39 hPa, and an R^2 value of 0.181. The data are adjusted, that is pressure gets added to all the pressures where $KWV \neq 0$. The rest of the points get added pressure according to the formula of the line. The end result is a straight line in such manner that there is no correlation between the two terms.

In Figure 6.25 the new $P_{\text{GPS(kwv)}}$ data are plotted against P_{baro}. This new $P_{\text{GPS(kwv)}}$ will be called adapted $P_{\text{GPS(kwv)}}$. The black plot is for a line with slope equal to 1 through the origin. For this linear relation the equation of the line is adapted $P_{\text{GPS(kwv)}} = -98.37 + 1.12(P_{\text{baro}})$. The

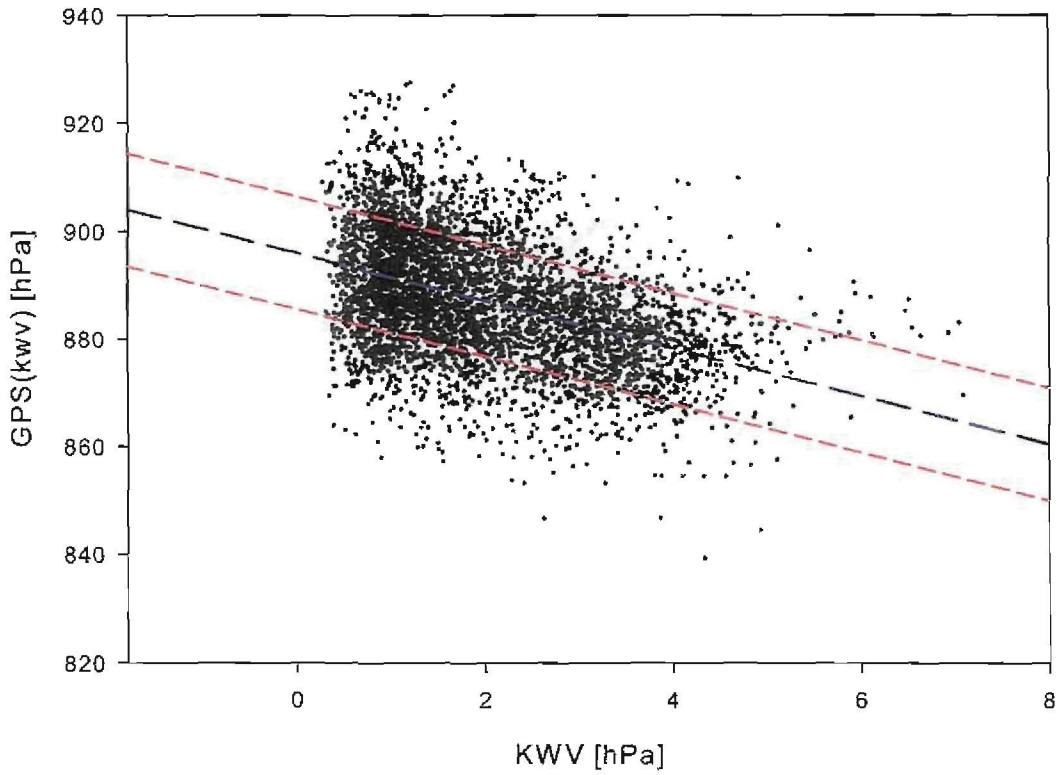

Figure 6.24: linear relation between $P_{GPS(kwv)}$ and KWV. The blue line is the linear fit and the red lines the 66% prediction band.

line has a 66% prediction band of ~4.69 hPa, and an R^2 value of 0.800. In Figure 6.6 the same regression has a 66% prediction band value of 6.32 hPa, that is a difference of 1.63 hPa. The R^2 value in Section 6.3 is 0.705, that is a difference of 0.095. These are rather big differences in the accuracy. According to this, the GPS-derived pressure agrees better with the hypothesis of this dissertation, if it does not correlate with the water vapour in the atmosphere.

6.8 Wind and its effect on atmospheric pressure

In Chapter 3 it was shown how much wind affects the pressure values of a Paroscientific barometer. In this section it will be shown whether there is any correlation between these pressure readings and wind. When this correlation is found and one is able to show how much this difference is it will be included in the data and will be corrected accordingly.

In Figure 6.26 the pressure as discussed in Section 6.3 is plotted against the wind speed. In

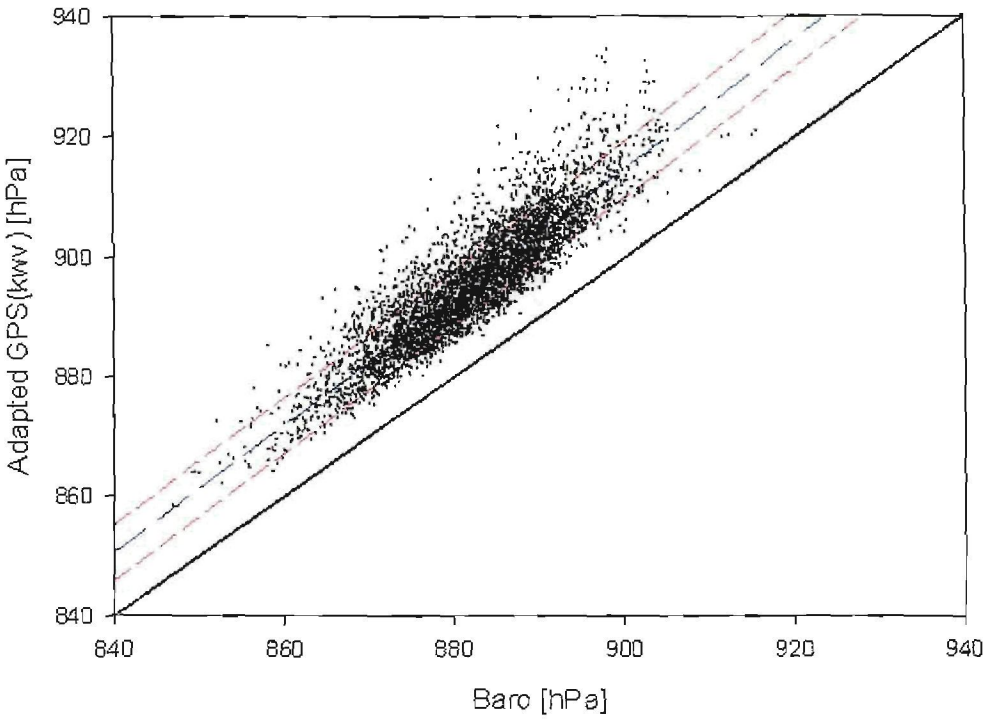

Figure 6.25: The linear relation between adjusted $P_{GPS(kwv)}$ and P_{baro}. The black line is for a line with slope m=1 through the origin, the blue line is the linear fit, and the red dashed lines represent the 66% prediction band.

this figure the green plot represents P_{baro}, the red plot $P_{GPS(0)}$, the black plot is for $P_{GPS(pwv)}$ and the blue plot is for $P_{GPS(kwv)}$. One would expect that all the GPS-derived pressures would not be dependent on the wind speed. The reason for this is because the GPS signal can not see the wind effect, or Bernoulli effect as was discussed in Chapter 3. Within the statistical uncertainties this is indeed the case.

Theoretically no GPS derived plot should have any correlation with wind speed, and the barometric pressure should have a negative slope. Therefore to find the absolute magnitude of the wind effect on the barometric pressure, one should subtract each GPS derived pressure from the barometric pressure; this is done in Figure 6.27. The red plot is for $P_{baro} - P_{GPS(0)}$, the black plot is for $P_{baro} - P_{GPS(pwv)}$ and the blue plot is for $P_{baro} - P_{GPS(kwv)}$. What is noticeable in this figure is the fact that all the graphs have the same small negative slope. This is as expected because the barometric pressure will always have pressure values equal to or smaller than the GPS derived pressure. This is due to the Bernoulli effect which was discussed in Chapter 3.

Assuming that the barometric pressure should not depend on the wind speed, one can correct

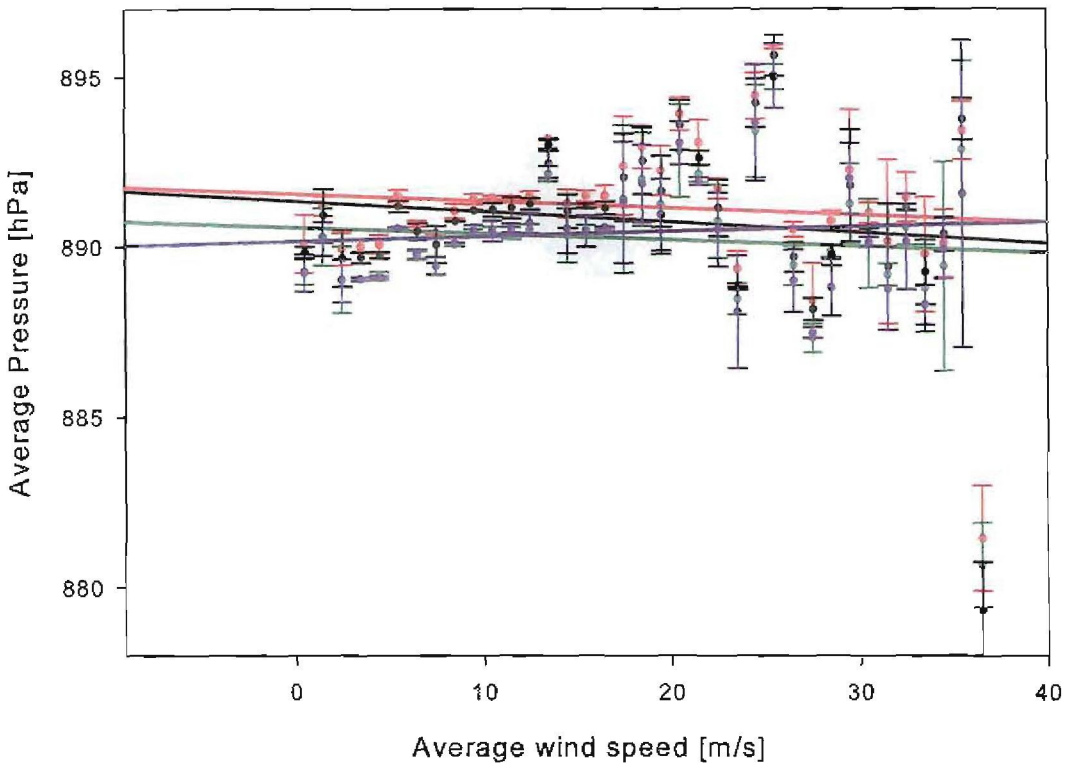

Figure 6.26: The linear relationships of the absolute average atmospheric bin pressures against the average wind speed. The green plot is for the P_{baro}, the red plot is for $P_{\text{GPS(0)}}$, the black plot for $P_{\text{GPS(pwv)}}$ and the blue plot for $P_{\text{GPS(kwv)}}$.

the data to have no correlation. In Figure 6.28 the correlation between P_{baro} and wind speed is shown. This correlation is more accurate than those in the previous pictures, as it is weighted. For this linear relation, the equation of the line is corrected $P_{\text{baro}} = 881.96 - 0.05(\text{windspeed})$. The line has a 66% prediction band of $\sim$8.73 hPa, and an R^2 value of 0.001. The data are adjusted, that is, pressure gets added to all the pressures where $KWV \neq 0$. The rest of the points get added pressure according to the formula of the line. The end result is a straight line in such manner that there is no correlation between the barometric pressure and wind speed.

In Figure 6.29 the $P_{\text{GPS(kwv)}}$ data are plotted against the new P_{baro}. This new P_{baro} will be called adapted P_{baro}. The black plot is for a line with slope equal to 1 through the origin. For this linear relation the equation of the line is adapted $P_{\text{GPS(kwv)}} = -98.06 + 1.12(P_{\text{baro}})$. The line has a 66% prediction band of $\sim$6.06 hPa, and an R^2 value of 0.716. In Figure 6.6 the same regression has a 66% prediction band value of 6.32 hPa, that is a difference of 0.26 hPa. The R^2 value in Figure 6.6 is 0.705, that is a difference of 0.011. These are rather small differences in

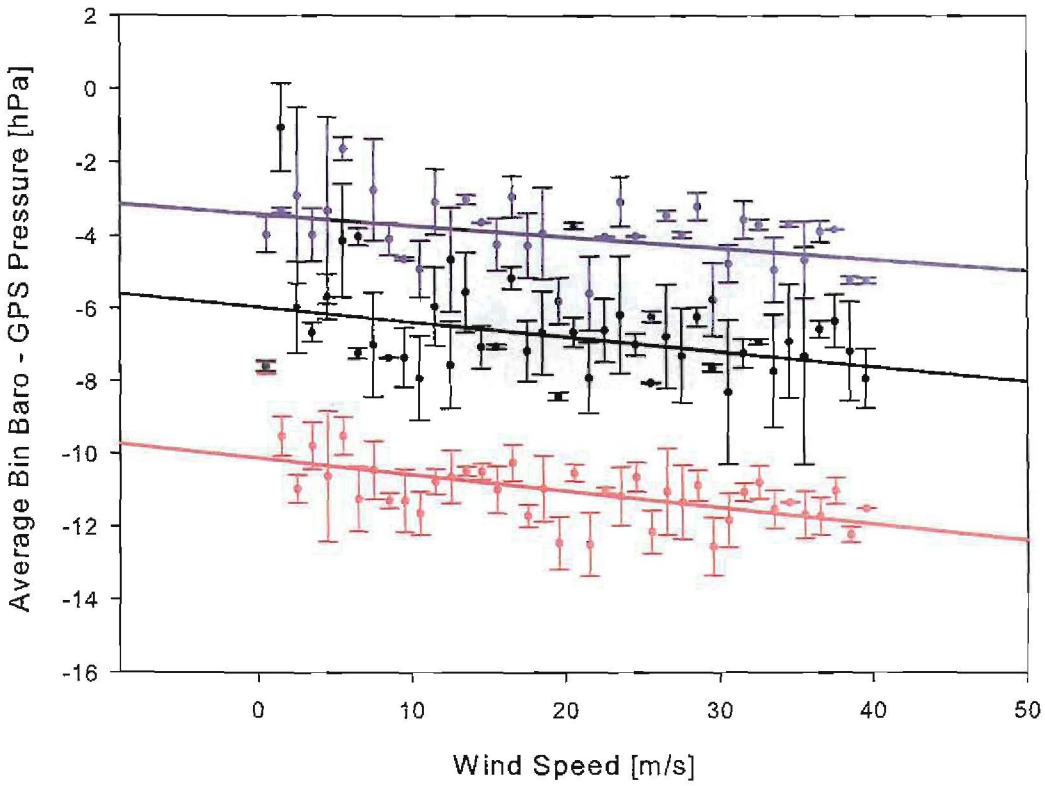

Figure 6.27: The linear relationships of the absolute average bin (Baro-GPS) pressures against the average wind speed. The red plot is for $P_{GPS(0)}$, the black plot for $P_{GPS(pwv)}$ and the blue plot for $P_{GPS(kwv)}$.

the accuracy. Therefore the wind speed has no or very little effect on the barometric pressure. Therefore the wind effect is not such a large effect as was suspected.

6.9 Seasonal effects

In this section it will be shown how seasonal effects influence weather variables used in this study. Thereafter these variables will be corrected accordingly, and a new linear plot of GPS(KWV) versus barometric pressure will be drawn. A conclusion will be made on this new accuracy at the end of the section.

In Figure 6.30 a time-series of the atmospheric temperature is plotted from beginning of 2000 till the end of 2006. It can be seen how the atmospheric temperature at the SANAE IV base increases and decreases periodically from summer to winter. In this graph the black line represents the harmonic function which corresponds the best with the data. The value of the

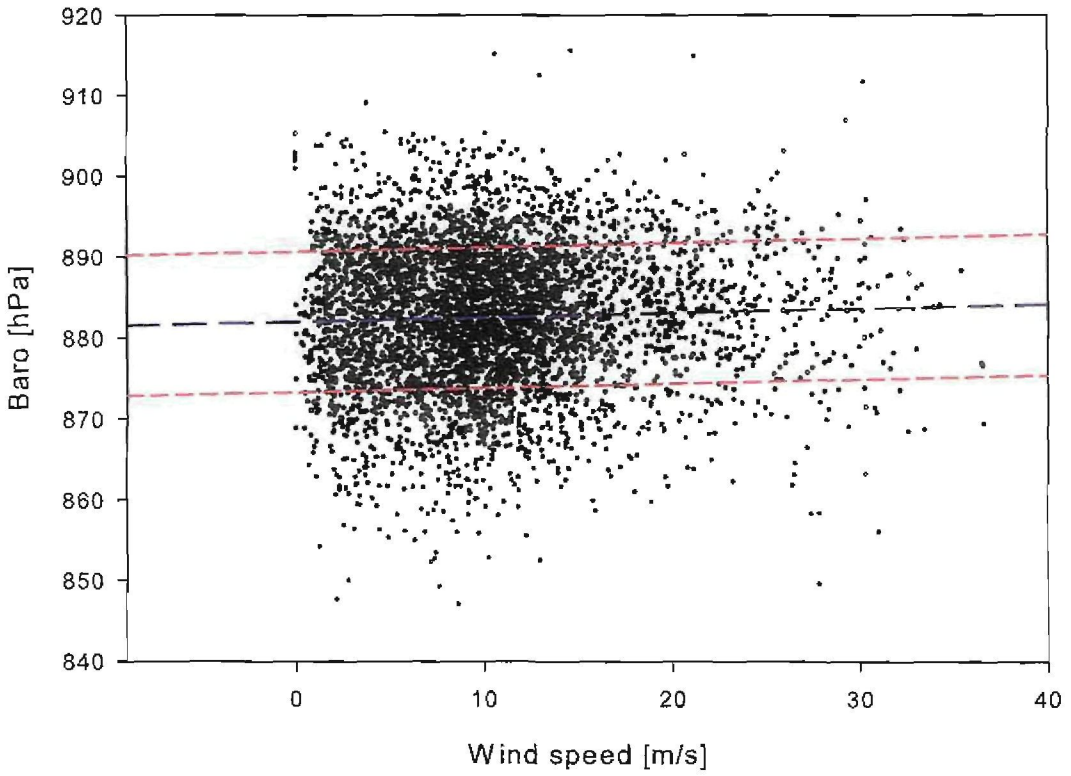

Figure 6.28: The linear relation between P_{baro} and wind speed. The blue line is the linear fit and the red lines the 66% prediction band.

atmospheric temperature T for this function is given by $T = -16.91 + 7.57\text{x}sin(2\pi d + 1.00)$, where d is the date in decimal years. The temperature is measured in degrees Celcius, and the angle in radians. The temperature is one of the most important weather variables as it affects the KWV so dramatically as is seen in (5.18).

The time line for wind speed measurements is shown in Figure 6.31. The wind speed and therefore the wind effect is the main focus of this dissertation, and therefore an important weather variable. The wind speed also has a seasonal periodicity, but unlike atmospheric temperature, it has an absolute sin function fit. This fit is given by wind $= 7.04 + 5.33\text{x}|sin(\pi d - 0.04)|$, where d is the date in decimal years. The noise, however, is so large that this seasonal effect is insignificant.

The important relationship between GPS(KWV) and barometric pressure is what one needs at the end of this section. It can be argued that both the GPS(KWV) and the barometric pressure data have these periodicities in them and will cancel out once plotted against each other. In

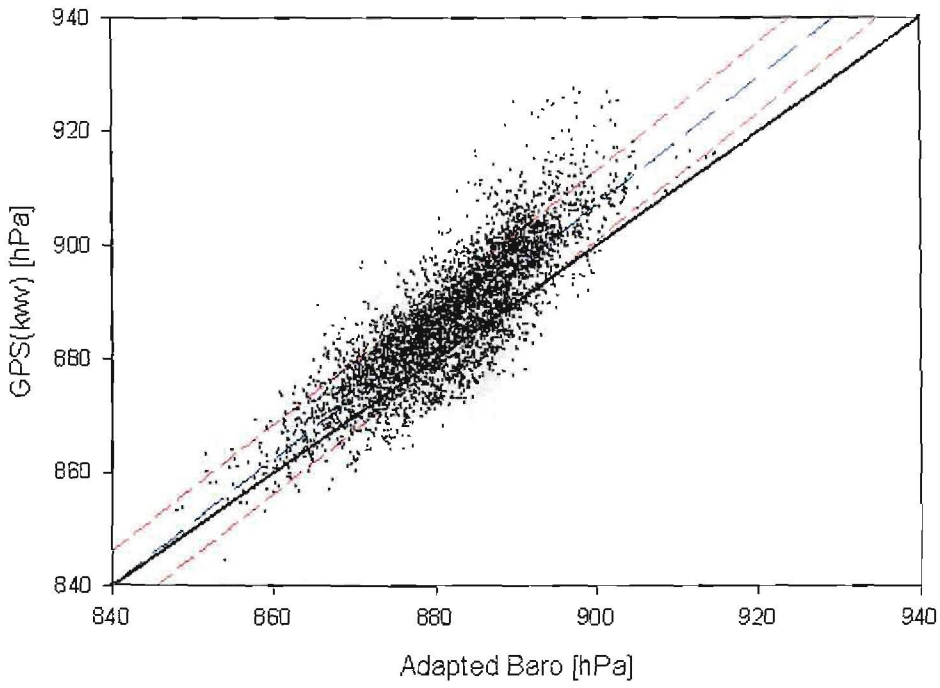

Figure 6.29: The linear relation between $P_{\text{GPS(kwv)}}$ and adjusted P_{baro}. The black line is for a line with slope m=1 through the origin, the blue line is the linear fit, and the red dashed lines represent the 66% prediction band.

Figure 6.32 it is shown how much this seasonal effect is present when these two quantities are subtracted from each other. The difference between GPS(KWV) and barometric pressure can be up to 40 hPa in the winter months. This is a very large difference and may cause a great deal of the standard deviation problem, found throughout this chapter. The periodicity for the pressure difference, ΔP, is given by $\Delta P = -4.78 + 15.29\text{x}|sin(\pi d + 0.13)|$, where d is for the date in years. As can be seen the absolute sin function only has a difference of maximum 15 hPa, that is 25 hPa less than the actual data. Therefore the periodicity can be predicted but the data can not be fully adjusted for this effect.

In Figure 6.33 the new $P_{\text{GPS(kwv)}}$ data are plotted against the P_{baro}. The black plot is for a line with slope equal to 1 through the origin. For this linear relation the equation of the line is adapted $P_{\text{GPS(kwv)}} = -3.59 + 1.00(P_{\text{baro}})$. The line has a 66% prediction band of ~4.54 hPa, and an R^2 value of 0.792. In Figure 6.4 the same regression has a 66% prediction band value of ~6.32 hPa, that is a difference of 1.78 hPa. The R^2 value in Figure 6.4 was 0.705, that is a difference of 0.087. These are big differences and show how much these seasonal effects in the data influence the correlation between the variables.

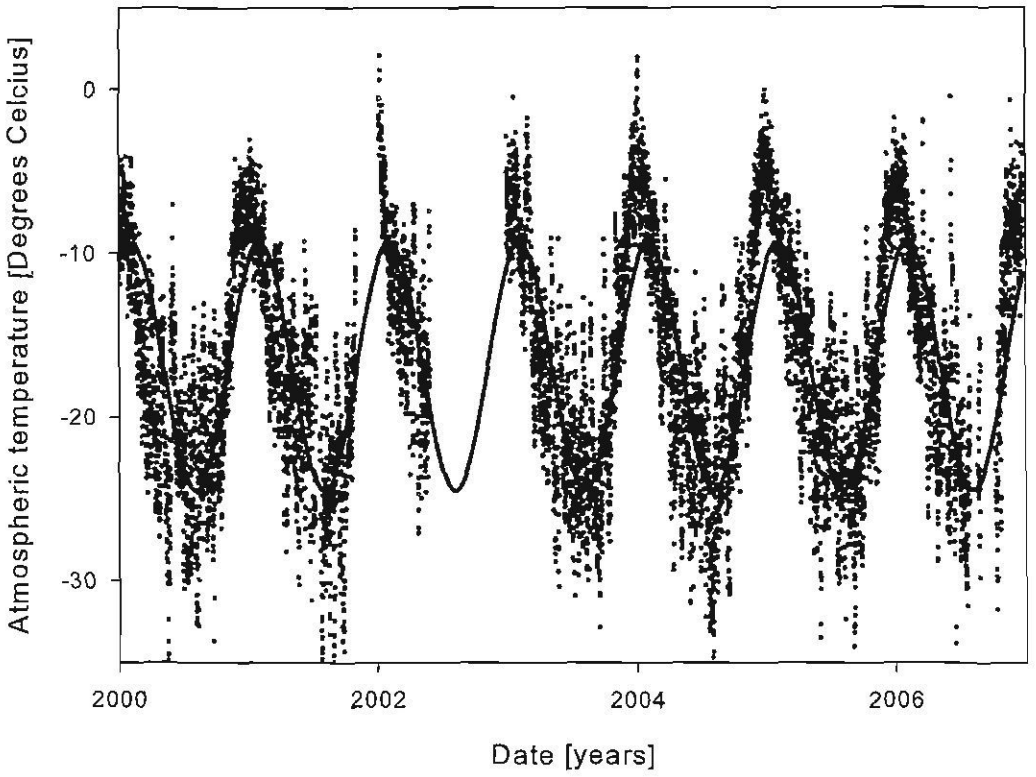

Figure 6.30: The time line for atmospheric temperature measurements at the SANAE IV base for period beginning 2000 till end 2006. The black line is the best fit sin function.

6.10 Summary

In this chapter it was shown how much different weather variables influence atmospheric pressure calculations. It was also shown how one is able to eliminate each of these variables from the data one by one, and how the accuracy of the data increases with each elimination. Furthermore, it became clear that although all these variables were eliminated the data never became that accurate. This is due to the problem of low pressure systems, as was briefly discussed in this chapter. The dependence of so many different variables on each other make the task of eliminating the wind speed very complicated. If all the standard deviations improvements are added up it comes to a total of 3.74 hPa. This is more than half the amount of the standard deviation in Figure 6.4. Therefore it is fair to say that much progress has been made regarding the accuracy of the data for the duration of this study.

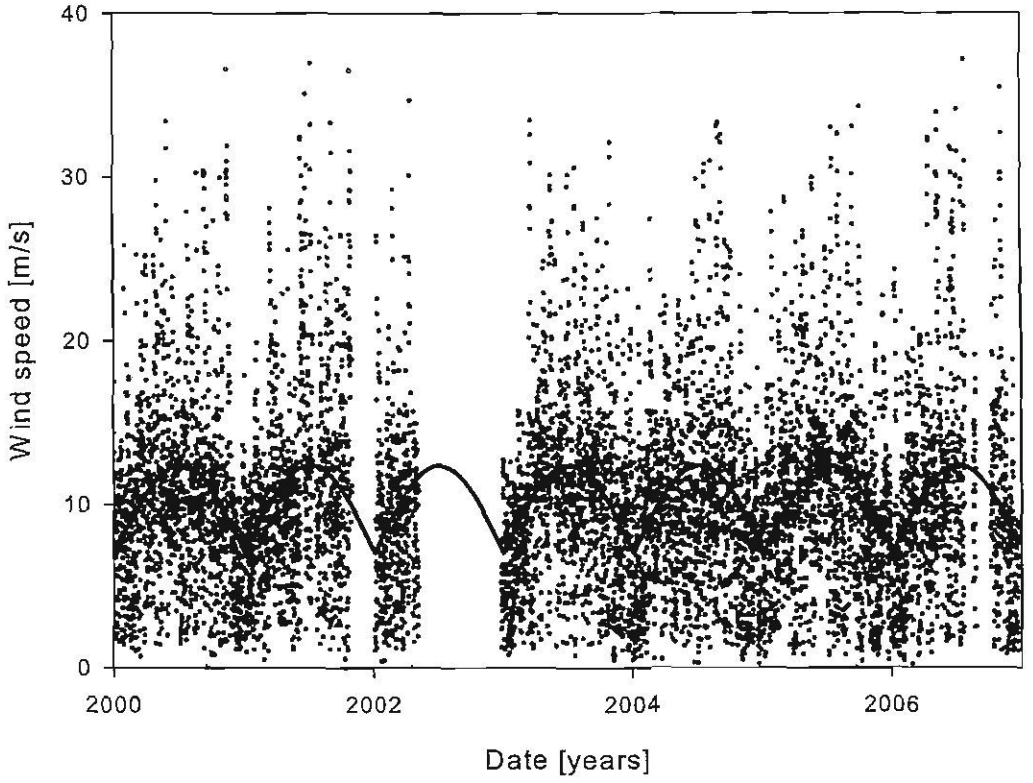

Figure 6.31: The time line for wind speed measurements at the SANAE IV base for period beginning 2000 till end 2006. The black line is the best fit absolute sin function.

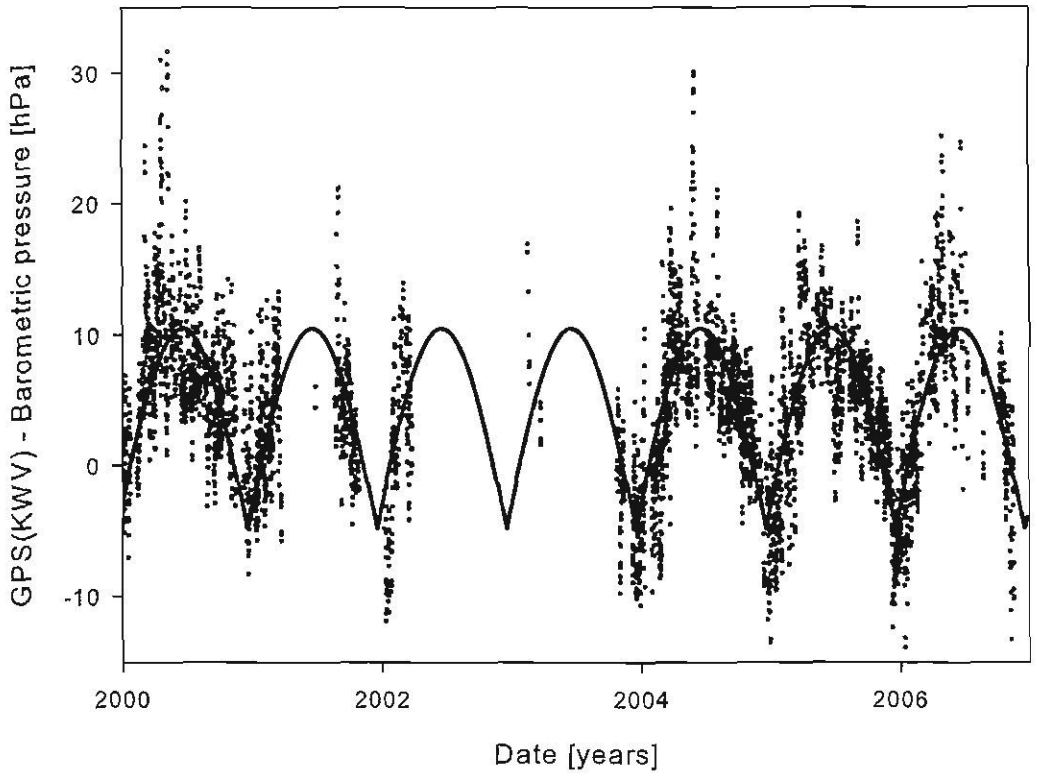

Figure 6.32: The time line for GPS(KWV)-baro pressure at the SANAE IV base for period beginning 2000 till end 2006. The black line is the best fit absolute sin function.

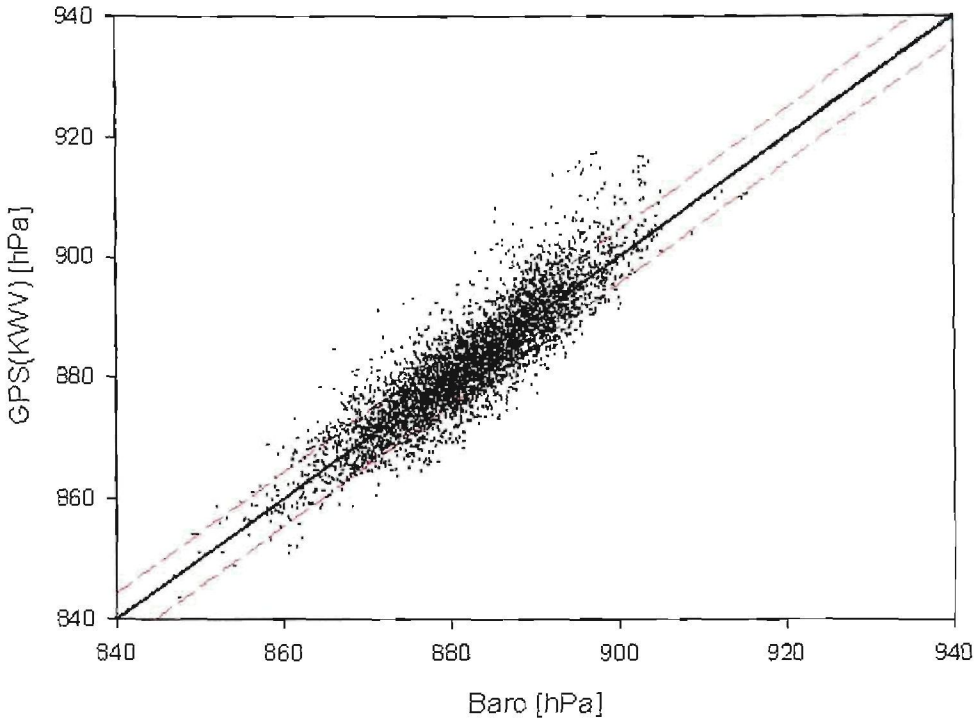

Figure 6.33: The linear relation between $P_{GPS(kwv)}$ and P_{baro}. The black line is for a line with slope m=1 through the origin, the blue line is the linear fit, and the red dashed lines represent the 66% prediction band.

Chapter 7

Summary and Conclusion

The aim of this study was to find an appropriate expression to eliminate the wind effect on pressure corrections for neutron monitor counting rates due to wind speed. The main idea was to use GPS technology to determine the atmospheric pressure. Using this specific technology one is able to eliminate the wind effect from the atmospheric pressure. Therefore one will be able to compare these two data sets and be able to determine the wind effect. A problem with calculating atmospheric pressure using GPS, is that it is so sensitive to atmospheric water vapour. Therefore a secondary study was to see how water vapour influences the propagation of an electromagnetic wave, specifically a GPS signal. Furthermore it was also shown how the fundamental physics fit with this technology.

The main results of this study are the following:

- In Chapter 3 it is shown how the wind speed influences the pressure measurements. It is shown how the Bernoulli effect may account for this wind speed problem. According to *Malan and Moraal* (2002) the Bernoulli effect may at most account for 81% of the effect, but most likely accounts for only 38% of this effect. Therefore in Chapter 3 it is confirmed that the Bernoulli effect does not give a satisfactory result.

- In Section 4.2 it is shown how GPS technology can be used to determine the atmospheric pressure at a certain position. The time delay for an electromagnetic wave to reach the surface of the earth from a GPS satellite at zenith for typical atmospheric conditions is $\sim$7.3 ns.

- In Section 5.2 the *Kuemmel* (1997) water vapour expression is derived from fundamental thermal physics. In Figure 5.2 the fundamental expression is compared to the KWV expression. It has been found that although using crude latent heat values to find the fundamental expression, they correlated well.

- In Section 5.4 the general dispersion expressions for electromagnetic waves are derived from fundamental electromagnetic theory. Furthermore these expressions are drawn in Figure 5.7 and 5.8, and it is shown how GPS signals are non-dispersive in the troposphere, but dispersive in the ionosphere.

- In Section 6.2 it is shown that the SANAE IV base has a mean wind speed of 10.3 m/s compared to Nelspruit's wind speed of 1.7 m/s and Sutherland's of 3.4 m/s. For the water vapour pressure, SANAE IV has a mean of 2.0 hPa, Nelspruit a mean of 14.2 hPa, and Sutherland a mean of 7.6 hPa. Thus in that section it is shown how well-suited SANAE IV is for experiments with this kind of properties.

- In Section 6.4 it is shown how different the PWV values are when compared to the KWV values. It is furthermore concluded that the PWV values should only be used as reference for other results, and not for finding any pressure results.

- Section 6.5 shows how the relative humidity data supplied by the SAWS does not agree with theory and need to be adjusted to be meaningful.

- Section 6.7.1 shows that this study is possible because wind speed and water vapour are not dependent on each other.

- In Section 6.3 it is shown that a standard deviation of 0.19 hPa is needed to be able to say that all effects have been eliminated from the data sets. Furthermore it is shown that the standard deviation between the GPS(KWV) derived pressure and the barometric pressure at the SANAE IV base is $\sim$6.32 hPa. Therefore the data are not accurate enough.

- When the new corrected relative humidity is used to find the GPS(KWV) derived pressure the new linear relationship has a standard deviation of $\sim$6.25 hPa. That is 0.07 hPa better than for the uncorrected relative humidity case. This difference is quite insignificant and is therefore meaningless.

- In Section 6.7.2 the water vapour, in this case KWV, is extracted from the GPS(KWV) derived pressure. It is then plotted against the barometric pressure, and a standard devi-

ation of ~4.69 hPa is found. This is 1.63 hPa smaller than the original relationship. This is quite a significant improvement.

- In Section 6.8 the wind speed is eliminated from the barometric pressure. The new linear relationship between GPS(KWV) derived pressure and barometric pressure has a standard deviation of ~6.06 hPa. Therefore the difference is 0.26 hPa which is a moderate difference.

- In Section 6.9 a seasonal periodicity was found in the data, it is shown that if the periodicity is eliminated the new linear relationship has a standard deviation of ~4.54 hPa. Therefore the difference is 1.78 hPa which is a large difference.

- If all these differences are added up a standard deviation of ~2.58 hPa can be found. This is more than 10 times higher than is needed for pressure correction of neutron monitor data, and therefore this study has been successful in showing that current PWV estimate and GPS accuracies are not sufficient to correct neutron monitor data under windy conditions.

Recommendations for future research are:

- To get better acquainted with weather systems and be able to analyse the dependence of weather variables. If one is able to do this one may be able to eliminate the low pressure system problem referred to in Chapter 6.

- To use other methods to determine the atmospheric water vapour. It is recommended that radiosondes or Water Vapour Radiometry (WVR) be used to do this.

  Finally, it is recommended that the Paroscientific barometer data still be used for the atmospheric corrections to neutron monitor data, because the wind effect on the pressure measurements is still small compared to the effect of water vapour on pressure estimates from GPS techniques.

Acknowledgements

"And I gave my heart to seek and search out by wisdom concerning all things that are done under heaven: this sore travail hath God given to the sons of man to be exercised therewith." Ecclesiastes 1:13

I would like to express my sincere gratitude to all colleagues, family, friends and institutions that made the completion of this dissertation possible. In particular, thank you to the following:

- My supervisor, Prof. Harm Moraal, for his patience in listening to what I had to say, and his guidance towards what needed to be done; his long hours poring over my work despite of him having a busy schedule. Thank you for bearing up with me although I sometimes have a tendency to be stubborn.
- Dr Attie Combrink, my co-supervisor, for always replying quickly to e-mail discussions; for helping me and guiding me wherever possible, and for encouraging me through all stages of my dissertation.
- My parents for their financial support throughout my studies; for encouraging me to be successful at what I do to do that which I enjoy and for giving me the chance to do what I wanted to do.
- Mrs Petro Sieberhagen and Mrs Elsabe Fraser for handling all my financial inquiries most efficiently.
- Mrs Hettie Sieberhagen for checking my grammar and spelling.
- I want to thank my friends, and the people I stayed with for always having the patience to listen when things where not always going well.
- Mr Mathew Holleran and Mrs Anne Mans for help with computer related problems.
- Mrs Lizelle le Roux and Mrs Lee-Ann van Wyk, secretaries at Physics, for their administrative help during my studies.

- The National Research Foundation and the Unit for Space Research of the NWU Potchefstroom Campus for financial support.
- My fianceè, Jeanie, for helping me to remember who I am, and why I am doing this; for always fighting with me when I stress about work; for her love and unconditional support in everything I do. I love you.
- Lastly, I am eternally grateful to our Heavenly Maker for His grace in giving me the opportunity to find Him throughout my life.

Izak.G. Morkel

Unit for Space Physics, North-West University, Potchefstroom Campus, 2520, South Africa

Bibliography

Bachelet, F., P. Balata, N. Iucci, and G. Dyring, Attenuation coefficient of the cosmic ray nucleonic component in the lower atmosphere, *Nuovo Cimento, 35*, 23, 1965.

Bachelet, F., E. Dyring, N. Iucci, and G. Villoresi, Time change of the attenuation coefficients for cosmic-ray neutron monitors, *Canadian Journal of Physics. Proceedings of the 10th International Conference on Cosmic Rays, Calgary, Alberto, June 19-30, 1967, Vol. 46., p.1041, 46*, 1041, 1968.

Bachelet, F., N. Iucci, G. Villoresi, and N. Zangrilli, The cosmic-ray spectral modulation above 2 GV. IV. The influence on the attenuation coefficient of the nucleonic component, *Nuovo Cimento B Serie, 11*, 1–12, 1972.

Balogh, A., R. G. Marsden, and E. J. Smith, *The heliosphere near solar minimum. The Ulysses perspective*, The heliosphere near solar minimum. The Ulysses perspective / André Balogh, Richard G. Marsden and Edward J. Smith (eds.). Springer-Praxis Books in Astrophysics and Astronomy. London: Springer. ISBN 1-85233-204-2, 2001, XXV + 411 pp., 2001.

Balthasar, H., and M. Schuessler, Preferred longitudes of sunspot groups and high-speed solar wind streams - Evidence for a 'solar memory', *Solar Physics, 87*, 23–36, 1983.

Bieber, J. W., and M. A. Pomerantz, Cosmic ray unidirectional latitude gradient: Evidence for north-south asymmetric solar modulation, *J. Geophys. Res., 96*, 11,569–11,585, 1991.

Bumba, V., and R. Howard, Solar Activity and Recurrences in Magnetic-Field Distribution, *Solar Physics, 7*, 28–38, doi:10.1007/BF00148402, 1969.

Cane, H. V., Coronal Mass Ejections and Forbush Decreases, *Space Science Reviews, 93*, 55–77, doi:10.1023/A:1026532125747, 2000.

Carmichael, H., and M. Bercovitch, Analysis of IQSY cosmic-ray survey measurements, *Canadian Journal of Physics, 47*, 2073–2093, 1969.

Chapman, S., and J. Bartels, Geomagnetism, *Oxford: Clarendon*, 1940.

Choudhuri, A. R., *The Physics of Fluids and Plasmas*, Cambridge University Press, 1998.

Combrink, A. Z. A., Detection of atmospheric water vapour using the global positioning system, Master's thesis, North-West University (Potchefstroom campus), 2003.

Combrink, A. Z. A., Sensing atmospheric water vapour using the global positioning system, Ph.D. thesis, University of Cape Town, 2006.

Debye, P., *Polar Molecules.*, Dover Publications Inc., 1929.

Decker, R. B., S. M. Krimigis, E. C. Roelof, M. E. Hill, T. P. Armstrong, G. Gloeckler, D. C. Hamilton, and L. J. Lanzerotti, Voyager 1 in the Foreshock, Termination Shock, and Heliosheath, *Science, 309*, 2020–2024, doi:10.1126/science.1117569, 2005.

Dorman, L. I., Cosmic Ray Meteorogical Effects, *Nauka*, 1972.

Dorman, L. I., J. F. Valdes-Galicia, and M. Rodriguez, Multistation comparitive study of the nucleonic barometric coefficient dependance with altitude, curoff rigidity and level of solar activity, *Proc. 25th International Cosmic Ray Conference (Durban), 2*, 457, 1997.

Ferreira, S. E. S., and K. Scherer, Modulation of Cosmic-Ray Electrons in the Outer Heliosphere, *Astrophys. J., 616*, 1215–1223, doi:10.1086/425034, 2004.

Fisk, L. A., Motion of the footpoints of heliospheric magnetic field lines at the Sun: Implications for recurrent energetic particle events at high heliographic latitudes, *J. Geophys. Res., 101*, 15,547–15,554, doi:10.1029/96JA01005, 1996.

Fujita, T., and K. Otani, Pressure oscillations due to high winds, *Report of Meteorogical Laboratory of Kyushu Institutes of Technology, 2*, 50, 1952.

Gleeson, G. M., L. J. Webb, Energy changes of cosmic rays in the interplanetary region, *Astrophys. Space Sci., 58*, 21, 1978.

Goldstein, B. E., M. Neugebauer, J. T. Gosling, S. J. Bame, J. L. Phillips, D. J. McComas, and A. Balogh, ULYSSES Observations of Solar Wind Plasma Parameters in the Ecliptic From 1.4 to 5.4 AU and Out of the Ecliptic, *Space Science Reviews, 72*, 113–116, doi: 10.1007/BF00768764, 1995.

Griffiths, D. J., *Introduction to electrodynamics (3^{rd} edition)*, Prentice Hall, 1999.

Harman, C. V., and C. J. Hatton, Contributions to the counting rate and the temperature dependence of neutron monitors, *Canadian Journal of Physics. Proceedings of the 10th International Conference on Cosmic Rays, Calgary, Alberto, June 19-30, 1967, Vol. 46., p.1052, 46*, 1052, 1968.

Humble, J. E., Private communication, 1998.

Iucci, N., Cosmic ray survey to Antarctica and coupling functions for neutron component near solar minimum (1996-1997), 2. Meteorological effects and correction of survey data, in *International Cosmic Ray Conference, International Cosmic Ray Conference*, vol. 7, p. 321, 1999.

Jokipii, J. R., and B. Thomas, Effects of drift on the transport of cosmic rays. IV - Modulation by a wavy interplanetary current sheet, *Astrophys. J., 243*, 1115–1122, doi: 10.1086/158675, 1981.

Jokipii, J. R., E. H. Levy, and W. B. Hubbard, Effects of particle drift on cosmic-ray transport. I - General properties, application to solar modulation, *Astrophys. J., 213*, 861–868, 1977.

Kallenrode, M., *Space physics: an introduction to plasmas and particles in the heliosphere and magnetospheres*, Springer, 2001.

Kalnay, E., et al., The NCEP/NCAR 40-Year Reanalysis Project, *Bulletin of the American Meteorological Society, vol. 77, Issue 3, pp.437-472, 77*, 437–472, 1996.

Kaplan, E. D., Understanding GPS: Principles and Applications, *Boston: Artech House*, p. 554, 1996.

Keenan, J. H., F. G. Keyesl, P. G. Hill, and J. G. Moore, *Steam Tables. (S.I. Units)*, Wiley, New York, 1978.

Kodama, M., Y. Ishida, and I. Shimizu, Development of a barometric sensor insensitive to high winds, *J. Meteo. Soc. Japan. Series II, 45*, 191, 1967.

Krüger, H., A calibration neutron monitor for long-term cosmic ray modulation studies, Ph.D. thesis, North-West University (Potchefstroom campus), 2006.

Krüger, T. P. J., The effect of a Fisk-Parker Hybrid Magnetic Field on Cosmic rays in the Heliosphere, Master's thesis, North-West University (Potchefstroom campus), 2005.

Kuemmel, B., Temperature, humidity and dew point, [Internet:] http://www.faqs.org/faqs/meteorology/temp-dewpoint/, 1997.

Leick, A., GPS Satellite Surveying, *New York: Wiley-Interscience.*, p. 352, 1990.

Lide, D. R., *CRC Handbook of Chemistry and Physics.*, Chemical Rubber Company, Boca Raton, 1994.

Lockwood, J. A., Forbush Decreases in the Cosmic Radiation, *Space Science Reviews, 12*, 658–715, doi:10.1007/BF00173346, 1971.

Lockwood, J. A., and A. R. Calawa, On the barometric pressure coefficient for cosmic ray neutrons, *J. Atmos. Terr. Phys., 11*, 23, 1957.

Malan, D., and H. Moraal, The effect of wind on pressure correction of the SANAE neutron monitor counting rate, *South African Journal of Science, 98*, 278–281, 2002.

Maletsoa, K. S., The effect of wind - SANAE N M data, Master's thesis, North-West University (Potchefstroom campus), 2000.

Marsden, R. G., The 3-D Heliosphere at Solar Maximum, *Publications of the Astronomical Society of the Pacific, 113*, 129–130, 2001.

Marsden, R. G., and R. G. Marsden (Eds.), *The High Latitude Heliosphere*, 1995.

McCracken, K. G., H. Moraal, and P. H. Stoker, A dual acceleration mechanism for the 20 January 2005 ground level enhancement , *J. Geophys, In proceeding*, 2008.

Medeiros, A. L., Radio propagation through the ionosphere layers, 2000.

Merry, C. L., *Introduction to the Global Positioning System (4th edition).*, University of Cape Town, 2006.

Meyer, P., R. Ramaty, and W. R. Webber, Cosmic rays - astronomy with energetic particles, *Physics Today, 27*, 23–30, 1974.

Nasa, Crossing of the Terminations shock by Voyager 2, [Internet:] http://voyager.jpl.nasa.gov/mission/fastfacts.html.

Parker, E. N., Dynamics of the Interplanetary Gas and Magnetic Fields, *Astrophys. J., 128*, 664, 1958.

Parker, E. N., Sudden Expansion of the Corona Following a Large Solar Flare and the Attendant Magnetic Field and Cosmic-Ray Effects, *Astrophys. J., 133*, 1014, 1961.

Parker, E. N., The passage of energetic charge particles through interplanetary space, *Planet. Space. Sci., 13*, 9, 1965.

Raubenheimer, B. C., Various aspects of the attenuation coefficient of a neutron monitor, Ph.D. thesis, Potchefstroom University for CHE, 1972.

Raubenheimer, B. C., and P. H. Stoker, Various aspects of the attenuation coefficient of a neutron monitor, *J. Geophys. Res., 79*, 5069–5076, 1974.

Schroeder, D. V., *An Introduction to Thermal Physics*, Heyden, R. J., 1999.

Shatashvili, K. L., and G. O. Rogava, The Cyclic Variations of the Barometric Coefficient of the Cosmic Ray Neutron Component Intensity, in *International Cosmic Ray Conference, International Cosmic Ray Conference*, vol. 4, p. 1176, 1995.

Shea, M. A., and D. F. Smart, Fifty Years of Cosmic Radiation Data, *Space Science Reviews, 93*, 229–262, doi:10.1023/A:1026500713452, 2000.

Shulman, L., Technical drawing date 27/09/1965, *Bartol Research Foundation*, 1997.

Simpson, J. A., Cosmic Radiation: Particle Astrophysics in the Heliosphere, in *Frontiers in Cosmic Physics, New York Academy Sciences Annals*, vol. 65, edited by R. B. Mendell and A. I. Mincer, pp. 95–+, 1992.

Simpson, J. A., The Cosmic Ray Nucleonic Component: The Invention and Scientific Uses of the Neutron Monitor (Keynote Lecture), *Space Science Reviews, 93*, 11–32, doi: 10.1023/A:1026567706183, 2000.

Smith, E. J., and R. G. Marsden, Ulysses Observations at Solar Maximum: Introduction, , *30*, 1–1, 2003.

Smith, E. J., et al., The Sun and Heliosphere at Solar Maximum, *Science, 302*, 1165–1169, doi:10.1126/science.1086295, 2003.

Steenkamp, R., Shock acceleration as source of the anomalous component of cosmic rays in the heliosphere, Ph.D. thesis, Potchefstroom University for CHE, 1995.

Stone, E. C., A. C. Cummings, F. B. McDonald, B. C. Heikkila, N. Lal, and W. R. Webber, Voyager 1 Explores the Termination Shock Region and the Heliosheath Beyond, *Science, 309*, 2017–2020, doi:10.1126/science.1117684, 2005.

Suda, H., and M. Kodama, Atmospheric pressure deficiency inside the hut inferred from cosmic rays at Syowa Base, *Antarctic Record. Japan, 20*, 53, 1963.

Svalgaard, L., and J. M. Wilcox, Long-term evolution of solar sector structure, *Solar Physics, 41*, 461–475, 1975.

Vomel, H., Saturation vapor pressure formulations, [Internet:] http://cires.colorado.edu/ voemel/vp.html, 2006.